

# **Extended use of Magnetic Resonance Sounding (MRS) datasets - QT inversion and resolution studies**

vorgelegt von  
Diplom Geophysiker  
**Mike Müller-Petke**  
Berlin

der Fakultät VI Planen Bauen Umwelt  
der Technischen Universität Berlin  
zur Erlangung des akademischen Grades

Doktor des Naturwissenschaften  
- Dr. rer. nat. -  
genehmigte Dissertation

Promotionsausschuss:

Vorsitzender: Prof. G. Franz  
Berichter: Prof. U. Yaramanci  
Berichter: Prof. A. Kemna  
Berichter: Dr. M. Hertrich

Tag der wissenschaftlichen Aussprache: 19. August 2009

Berlin 2009  
D 83



# Abstract

*Mike Müller-Petke, Berlin University of Technology, PhD thesis 2009*

## **Extended use of Magnetic Resonance Sounding (MRS) datasets - QT inversion and resolution studies**

The present thesis provides a comprehensive insight into the Magnetic Resonance Sounding (MRS) inverse problem and introduces the QT inversion scheme as native solution scheme of the inverse problem. At this, the thesis analyses the inverse problem in terms of resolution and stability both in theory, synthetic and field examples, mostly restricted to 1D depth sounding (MRS) but with an outlook on 2D tomography like investigations (MRT), and follows several tasks.

First and within the scope to develop an improved inversion scheme the currently available solution schemes are analysed. This analysis includes the initial value inversion using extrapolated initial values and the time step inversion using multiple inversions for several different record times. The resulting new approach, called QT inversion, incorporates directly the native data structure of two variables, namely the pulse moment  $q$  and the record time  $t$ , and provides improved resolution and stability.

Second, the model and data spaces of the initial value inversion scheme are investigated. In order to assess the model resolution as a function of the loop size, maximum pulse moment and noise level, the model space is studied. On the one hand, the results of this study help to determine field settings appropriate to the target of investigation. On the other hand, the estimated model can be evaluated concerning its reliability using measures of resolution derived from the model resolution matrix.

Besides model resolution the data space carries information on data dependencies. Consequently, analysing the data resolution matrix a sequence of optimal distributed pulse moments is derived. This optimal pulse moment distribution provides the maximum amount of information most efficiently. This analysis introduces the data resolution matrix rather than the model resolution matrix, as object of analysis into the field of experimental design.

In addition, the properties of the mono or multi-exponential fitting are studied, and possibilities to improve the estimated model using transformation that restrict the model and data space with upper and lower boundaries are shown. At this, the pseudo water content is introduced to permit data space transformations.

Finally, all subtasks are summarised, assessed and discussed at a field example.





# Zusammenfassung

*Mike Müller-Petke, Technische Universität Berlin, Doktorarbeit 2009*

## **Erweiterter Nutzen von Datensätzen der Magnetischen-Resonanz Sondierung (MRS) - QT Inversion und Studien zum Auflösungsvermögen**

Die vorgelegte Dissertationsschrift stellt einen möglichst umfassenden Einblick in die inverse Aufgabe der Magnetischen-Resonanz Sondierung (MRS) dar. Im Besonderen wird ein neues Inversionsschema, die QT Inversion als natürlicher der Datensatzstruktur entsprechender Lösungsansatz, vorgestellt. Das inverse Problem wird dieser Zielstellung folgend, hinsichtlich Auflösungsvermögen und Stabilität sowohl im theoretischen Rahmen als auch mittels synthetischer und praktischer Beispiele. Dabei folgt die Arbeit mehreren Aufgabenfeldern.

Zum Einen, werden die verfügbaren Lösungsansätze im Hinblick auf die Entwicklung eines verbesserten Schemas analysiert. Die Analyse beinhaltet dabei das Inversionsschema basierend auf extrapolierten Werte der gemessenen Zeitreihen zum Zeitpunkt null (Initial value inversion) und das Zeitschrittinversionsschema, d.h. die gemeinsame Interpretation von Inversionen zu definierten verschiedenen Zeitpunkten der Zeitreihen (Time step inversion). Der, auf dieser Analyse beruhende, verbesserte Ansatz wird als QT Inversion bezeichnet und benutzt erstmalig nativ die Abhängigkeit des Datensatzes von zwei Variablen, dem Pulsmoment  $q$  und der Aufzeichnungszeit  $t$ , direkt, um verbesserte Auflösungseigenschaften und Stabilität zu gewinnen.

Zum Anderen, werden der Model- und Datenraum des Initial value Inversionsschemas analysiert. Die Analyse des Modelraums führt dabei auf die Evaluierung des Inversionsresultates in Abhängigkeit von Spulengröße, maximalem Pulsmoment und Rauschlevel. Die gewonnenen Erkenntnisse helfen dabei, dem Objekt der Untersuchung entsprechende, angepasste Messanordnungen zu wählen und durch Berechnung von Auflösungsmaßen das durch die Inversion gewonnene Model hinsichtlich seiner Vertrauenswürdigkeit zu untersuchen. Die Analyse des Datenraums ermöglicht die Wahl einer optimalen Verteilung von Pulsmomenten, dergestalt dass unter dem Gesichtspunkt der Effektivität der maximale Informationsgehalt extrahiert werden kann. Diesem Feld des experimentellen Designs wird damit die Analyse der Datenauflösungsmatrix hinzugefügt.

Ergänzend werden die Eigenschaften der mono und multi-exponentiellen Datenanpassung untersucht, sowie die Möglichkeiten das Inversionsresultat mittels Transformationen, d.h. dem Einschränken des Model- und Datenraumes durch obere und untere Grenzen, zu verbessern, gezeigt. Dabei wird die Größe des scheinbaren Wassergehaltes eingeführt, um die Transformationen auch auf den Datenraum erweitern zu können.

Abschließend werden alle Teilaufgaben in einem Feldbeispiel zusammengefasst, beurteilt und diskutiert.



# Contents

<b>1</b>	<b>Introduction</b>	<b>1</b>
<b>2</b>	<b>Surface NMR Forward Problem</b>	<b>5</b>
2.1	NMR phenomenon . . . . .	5
2.2	Surface NMR signal . . . . .	8
<b>3</b>	<b>Surface NMR Inverse Problem - Overview</b>	<b>13</b>
<b>4</b>	<b>Surface NMR Dataset</b>	<b>21</b>
4.1	Inversion scheme independent dataset processing . . . . .	22
4.2	Dataset processing and error estimations for initial value inversion . . . . .	26
4.2.1	Dataset exponential fitting and extrapolation . . . . .	26
4.2.2	Dataset error estimations . . . . .	30
4.3	Dataset processing and error estimations for QT Inversion . . . . .	37
4.4	Estimating systematic error - Frequency variations while stacking . . . . .	39
4.4.1	Modelling frequency variations while stacking . . . . .	39
4.4.2	Effects of frequency variations on fitting results . . . . .	40
4.4.3	Detectability of frequency variations . . . . .	42
4.5	Conclusion and outlook . . . . .	44
<b>5</b>	<b>Initial Value Inversion</b>	<b>47</b>
5.1	Singular Value Decomposition (SVD) . . . . .	47
5.1.1	The inverse problem in terms of SVD . . . . .	47
5.1.2	Picard Plot and model space basis vectors . . . . .	50
5.1.3	The model resolution matrix in terms of SVD and measures of resolution . . . . .	51
5.1.4	The data resolution matrix in terms of SVD . . . . .	53
5.2	Results of the model resolution analysis . . . . .	54
5.2.1	Parameter dependencies of the interval of confidence . . . . .	54
5.2.2	Resolution width in dependency on loopsize . . . . .	56
5.2.3	Field case: Haldensleben . . . . .	56
5.3	Results of the data resolution analysis . . . . .	60
5.3.1	Calculation of optimal pulse moment distributions . . . . .	60
5.3.2	Evaluation of optimal pulse moment distributions . . . . .	61
5.3.3	Efficient number of pulse moments . . . . .	64
5.3.4	Efficiency in dependency on loopsize, noise and maximum pulse moment . . . . .	68
5.4	The transformed inverse problem . . . . .	69
5.4.1	Model space transformations . . . . .	69
5.4.2	Data space transformations . . . . .	70
5.4.3	Evaluating the use of transformations . . . . .	73
5.5	Outlook on 2D Resolution . . . . .	76

<b>6</b>	<b>QT Inversion</b>	<b>83</b>
6.1	Forward operator . . . . .	86
6.2	Inverse problem . . . . .	86
6.3	Synthetic comparison . . . . .	88
<b>7</b>	<b>Field cases</b>	<b>93</b>
7.1	Naunen . . . . .	93
7.1.1	Test site geology - laboratory measurements . . . . .	93
7.1.2	Results of the different inversion schemes . . . . .	97
7.1.3	Discussion and comparison to the laboratory data . . . . .	100
7.2	Shwaib . . . . .	104
7.2.1	Test site geology - borehole NMR . . . . .	104
7.2.2	Results . . . . .	104
<b>8</b>	<b>Conclusion and Outlook</b>	<b>111</b>
<b>9</b>	<b>Acknowledgements</b>	<b>113</b>

# 1 Introduction

The phenomenon of Nuclear Magnetic Resonance, independently discovered in 1940ies by two groups of researchers (Purcell, Torrey, Pound and Bloch, Hansen Packard), takes advantage of a quantum-mechanical property of matter, namely the Spin, and allows investigations of matter at the basis of signals originating from the nuclei. It has found a widespread of use in medical, chemical and (geo) physical sciences. Concerning geophysical investigations this is due to its direct access to hydrogen protons and thus direct detectability of water.

All NMR based techniques share a common procedure in which an alternating magnetic field (the excitation or secondary field) at Larmor frequency forces reorientation of the macroscopic magnetic moments from their thermal equilibrium orientated along with the static (or primary) field. After the excitation field is extinguished, the orientation of magnetisation relaxes back to this equilibrium. This relaxation process generates a weak magnetic field that is measured and analysed to determine the matters properties.

Surface Nuclear Magnetic Resonance (surface NMR) as the superordinated method and Magnetic Resonance Sounding (MRS) as its application for 1D water content depth sounding denotes the usage of NMR for geophysical exploration at field scale to detect ground water and to characterise aquifer properties like hydraulic conductivities from the surface.

The technique of surface NMR was introduced by Russian scientists in the 1980ies and first field results were published by (Semenov et al., 1988). In 1996 Iris Instruments introduced the first commercially available device and triggered the interests of research groups outside of Russia. Currently, profound research on the fundamentals of the technique is concentrated at a workgroup of Iris Instruments, the geological survey of France (BRGM), the University of Grenoble (France), ETH Zurich (Switzerland), a Russian group in Novosibirsk and at the Berlin University of Technology (Germany) in cooperation with the geological survey of Germany (BGR). Furthermore, there is increasing research from China as well as from Iran during the last years. Besides continuous publications of actual research results, international workshops that took place in 1999, 2003 and 2006 led to special issues on MRS published in 2002 (Journal of Applied Geophysics), 2005 (Near Surface Geophysics) and 2008 (Journal of Applied Geophysics).

The simplest configuration of MRS operates with a single loop at the Earth's surface. This loop acts both as transmitter (emitting the excitation field) and receiver (recording the relaxation signal). The depth sensitivity is based on changed excitation intensities, i.e., the pulse moment  $q$  that is the products of the loops current and pulse duration. Increasing or decreasing the pulse moment increases or decreases the depth of investigation, respectively. Hence, the surface NMR dataset are NMR signals in dependency of the pulse moment  $q$  and have to be inverted for their spatial distribution. The basic theory had been presented in some review articles (e.g. Yaramanci (2000); Legchenko and Valla (2002)) but neither obviously possible separate transmitter and receiver loops nor the subsurface resistivity are completely discussed. The most general formulation introducing the actual state of art surface NMR formulation was

## 1 Introduction

published by (Weichman et al., 1999, 2000). This formulation allowed modelling of complex surface NMR signals including separated transmitter and receiver loops and takes into account the vectorial nature of the NMR phenomenon as well as the subsurface resistivity distribution.

Consequently, the recent research now includes all model parameter that influence the methods physics. On the one hand, extended formulations triggered the development to overcome the restrictions on 1D applications using 2D and 3D forward modelling Eikam (2000); Warsa et al. (2002) and introducing separated loop configurations (Hertrich et al., 2005). In further development, inversion schemes have been adopted to 2D and according to geophysical notation the extension to 2 spatial dimensions is called Magnetic Resonance Tomography (MRT), as presented in Hertrich et al. (2007). On the other hand, detailed investigations on the resistivity influence on the MRS signal were carried out (Braun, 2007) and finally led to a inversion of the subsurface resistivity as presented by (Braun and Yaramanci, 2008). Furthermore, jointly with subsurface resistivity information measures of water quality are available.

Besides the development of the theoretical concepts the method has proved its usage as hydrogeophysical exploration technique (Vouillamoz et al., 2008) due to its outstanding properties compared to other geophysical methods, thanks to the direct sensitivity to hydrogen protons, i.e., quantitative measures of both subsurface water content and hydraulic conductivity. At this, beside the total (effective or extractable) water content distribution, the decay time is essential. Surface NMR measures  $T_2^*$ , i.e., the relaxation constant of the free induction decay (FID) in dependency of  $q$ . Legchenko and Valla (2002) presented a scheme to invert not only for the depth distribution of the subsurface water content but also the depth distribution of the decay time  $T_2^*$  using a mono-exponential approach. Commonly, laboratory NMR and borehole NMR use a decay time distribution to describe the NMR relaxation behaviour of a complete sample derived by multi-exponential fitting, i.e., describing the partial amount of water relative to some decay time (interval). Thus, a concept of Legchenko and Valla (2002) was extended to multi-exponential fitting by Mohnke and Yaramanci (2005) and introduced a decay time distribution in dependency on the spatial dimension as necessary for surface NMR. Mohnke and Yaramanci (2005) used the description decay time spectra while in this thesis partial water content (PWC) distribution is proposed as a more convenient descriptor. Ongoing from this PWC distribution the total water content as a function of depth is the sum over all decay times. In this notation, the logarithmic mean of the PWC distribution as a function depth, as a usually used measure for a mean decay time, is named decay time depth distribution. Hence, the inverted  $T_2^*$  decay times may provide additional information about aquifer properties due to their dependency on the pore space geometry but compared to laboratory and borehole measurements that provide  $T_1$  and  $T_2$  distributions these information are limited.

All of which above improved the surface NMR forward modelling or extended the limitations concerning inversion results, but extended insight in the inverse problem is only presented by Legchenko and Shushakov (1998). But these insights into the inverse problem are of importance to evaluate limitations of resolution and reliability as well as to improve inversion schemes and to extend its limitations. At this, the thesis will provide detailed knowledge on the surface NMR inverse problem. The results are mostly restricted to the 1D case but with a preliminary outlook to 2D resolution properties.

Chapter 2 gives a brief review on NMR basics deriving the most essential results of the spin theory on the basis of Bloch's set of equations. The fundamental equation of surface NMR is shown and discussed afterward.

Chapter 3 opens the field of the surface NMR inverse problem from a general point of view. It should allow the reader to understand the possible range of solution approaches that are discussed in later chapters. The fundamental differences according to the dataset, forward operator and model parameter of the different solution schemes will be shown. It provides the knowledge of how to construct the forward problem from the fundamental surface NMR equation and therefore the operator to be inverted as well as the needs for dataset preparation or processing, depending on the solution approach.

After this overview of approaches and prior to analysing properties, like resolution and stability of the inversion schemes (as it is done in chapter 5/6), the measured dataset is focused in-between these chapters.

The dataset has to be analysed before discussing inversion aspects due to the fact that measured dataset builds the basis of all forthcoming steps. At this, data is handled not only as input parameter for the inversion but defining the need (and strength) of regularisation due to noisy data. Consequently, a proper regularisation of the inverse problem has to be based on analysing the data error, e.g. discussing the mono-, bi-, or multi-exponential fitting. Hence, in this chapter it is shown how data error can be estimated and how this might vary depending on processing schemes and/or processing steps.

At the same level of importance, limitations that cannot be seen by a solitary look at inversion results (that might look nicely but do not fit geological expectations) like systematic data error have to be analysed. Thus, the outcome of this chapter is fundamental understanding of surface NMR dataset and a roadmap to follow in order to process and evaluate measured data prior to invert for the subsurface model.

The inversion scheme widely used is the initial value inversion, i.e., reducing the dataset to a sounding curve that has to be approximated by an appropriate water content model. Chapter 5 investigates the resolution of model parameters and maximum depth of investigation with respect to different parameters like loop size, resistivity and available pulse moments. Some tables and graph providing an overview of general relationships are given, hopefully help to plan field surveys. At a field case the use of such kind of pre-analysis is shown.

Furthermore, the efficiency of different sequences of pulse moments using a data space analysis is evaluated (experimental design). The necessary total number of pulse moments is derived and discussed under the scope of the quality of the inversion results. Finally, the influence and improvements of transformations on the inversion scheme is shown. Pseudo water content is introduced, enabling restrictions not only to the water content but also to the data and significantly improving the inversion results.

The spatial extension on 2D water content inversion arises from calculating the forward operator in 2 dimensions and to get a tomography like subsurface image. Multiple soundings at different loop locations and configurations are used. While MRS takes only a coincident loop layout into account, for 2D investigations separated loop layouts where additionally introduced. Therefore, the loop layout for a 2D subsurface image, i.e., overlapping stations and loop separation are parameters that obviously influence the inversion result. Currently, the spatial

## 1 Introduction

extension to 2D uses initial values as input data. Thus, the resolution properties of different layout strategies are assessed in section 5.5.

Chapter 6 introduces a completely new but somehow more native inversion scheme: the QT inversion. QT inversion uses the complete surface NMR dataset build by the pulse moment  $q$  and the record time  $t$  at once, i.e., calculates a model that satisfies all data in a single step. This is, in contrast to all previously presented inversion schemes that divide the solution path into two steps. Consequently, it promises improved resolution and stability. It is assessed with synthetic and real datasets and compared to the commonly used strategies.



## 2 Surface NMR Forward Problem

The forward problem of Surface Nuclear Magnetic Resonance is a coupled problem. It consists of the Nuclear Magnetic Resonance phenomenon, i.e. the usage of a quantum-mechanical property of matter, namely the Spin. Discovered in the 1940ies the NMR phenomenon has nowadays found a widespread of use in medical, chemical and (geo) physical sciences. While in petrophysical lab applications the theory of NMR can be applied straight forward the counterpart that leads to a geophysical surface related application is the electromagnetic field propagation of surface loops at a fixed frequency.

### 2.1 NMR phenomenon

The quantum mechanical property of matter called spin is one of the four basic physical properties of atoms. The three others are: mass, electric charge and microscopic magnetisation. Since matter is made of atoms there are macroscopic consequences, i.e., matter has a mass and depending on the internal structure an electric charge. These two are easily observable. Macroscopic magnetisation sometimes occurs but is due to the movement of electrons while nuclear magnetism is very weak. Finally, nuclear spin is even less tangible. One can imagine the nuclear spin as an atomic nucleus that is rotating like a tiny planet in space and thus has an angular momentum. But in fact, it is an intrinsic property of the nucleus without any rotation behind. Even though, there is no simple macroscopic consequence, like a macroscopic spin, a macroscopic magnetisation or net magnetisation at the base of microscopic nuclear spins can occur.

**Macroscopic magnetisation:** Lets distinguish between microscopic magnetisation, i.e., an isolated nuclear spin, and macroscopic magnetisation, i.e., net magnetisation  $\mathbf{M}_0$  of an ensemble of spins. Based on the microscopic magnetisation a macroscopic magnetisation exist if an external magnetic field  $\mathbf{B}_0$  is applied and described by Curie's law

$$\mathbf{M}_0 = \frac{\rho_0 \gamma^2 \hbar^2 \mathbf{B}_0}{4k_B T} \quad (2.1)$$

with  $\hbar = h * 2\pi$  the Planck constant,  $\rho_0$  the number of spins per volume,  $k_B$  the Boltzmann constant,  $T$  the temperature. Obviously, the magnitude of this macroscopic magnetisation is proportional to the amplitude of its source, the external field  $\mathbf{B}_0$  and has the same orientation. After [Levitt \(2002\)](#) this macroscopic magnetisation can be qualitatively understood. Without external magnetic field the isolated microscopic moment are randomly orientated in space and thus cancelling the magnetisation in a macroscopic view. If an external static field exists a magnetisation behaves like a gyroscope rotation at a cone around the orientation of the static field. Since the spatial location of the single spins is not constant and thus also the local static field properties show tiny fluctuation the rotation cone of each spin is not constant. In addition, the parallel orientation of the spin moment with the static field orientation is more

## 2 Surface NMR Forward Problem

stable than the antiparallel orientation. Both together results in a very slight amount of more spins orientated with the static field after some time, i.e., the relaxation time  $T_1$ , building the macroscopic magnetisation  $M_0$  orientated with the external static field.

**NMR experiment:** How can we take advantage of this macroscopic magnetisation? In the following the simplest NMR experiment as it is used for surface NMR is described.

First, a strong static external magnetic field  $\mathbf{B}_0$  is applied to a sample causing a macroscopic magnetisation  $\mathbf{M}_0$  at an amplitude as described by Curies law. According to surface NMR, the static field is the earth magnetic field and the sample is the subsurface.

Second, the macroscopic magnetisation is forced to tilt with respect to the earth's field direction using an alternating excitation field  $\mathbf{B}$  (the secondary or excitation field) that is perpendicular to  $\mathbf{B}_0$  (or at least with field components  $\mathbf{B}^\perp$  perpendicular to  $\mathbf{B}_0$ ) at the larmor frequency (Levitt, 2002)

$$\omega_l = -\gamma \cdot |B_0| \quad (2.2)$$

with  $\gamma$  as a specific value for nuclei ( $\gamma_{hydrogen} = 0.2675 \frac{Hz}{nT}$ ). The angle of excitation depends on the amplitude of  $\mathbf{B}^\perp$  and the duration  $\tau$  of this excitation field, usually called excitation pulse. There are different types of pulses according to different objectives. One of those are  $90^\circ$  pulses that flip the orientation of the magnetisation from the z-axis by  $90^\circ$  to e.g. exactly the y-axis. Since the earth field is not constant in time or the Larmor frequency might not be chosen properly, one should also account for off-resonance effects as described in Mansfield et al. (1979); Legchenko (2004) or Braun (2007). These off-resonance effect cause improper  $90^\circ$  flip angles, i.e., an orientation of the magnetisation after the pulse including z- and x-components. If this excitation field is extinguished, i.e., after pulse cutoff, the orientation of the macroscopic magnetisation will move back to its parallel orientation with the static field. The movement of the magnetisation can be described by the Bloch equations and is discussed in the following. Basically, this motion is a precession, emitting a electromagnetic field at Larmor frequency that is measured and analysed concerning the captured information.

**Bloch equations:** The basic equations that describe the behaviour of a magnetisation vector  $\mathbf{M}$  in dependency of the time  $t$  under the presence of a magnetic field  $\mathbf{B}_0$  and damping conditions (relaxation constants  $T_1$  and  $T_2$ ) are the Bloch equations

$$\frac{d\mathbf{M}}{dt} = \gamma[\mathbf{M}(t) \times \mathbf{B}_0] - \frac{M_x \mathbf{e}_x + M_y \mathbf{e}_y}{T_2} - \frac{M_z - M_0}{T_1} \mathbf{e}_z \quad (2.3)$$

According to the NMR experiment after excitation field cutoff,  $\mathbf{B}_0$  is the primary static field

$$\mathbf{B}_0 = [0, 0, B_0]^T \quad (2.4)$$

and the magnetisation vector at  $t = 0$  for perfect  $90^\circ$  pulses e.g.

$$\mathbf{M}(t = 0) = [0, M_0, 0]^T. \quad (2.5)$$

Off-resonance effect are taken into account via introducing the angles  $\phi, \theta$ , in the common notation of spherical coordinates, calculated in dependency on the off-frequency and defining the position of the magnetisation in space. Exemplary after Mansfield et al. (1979) (for more

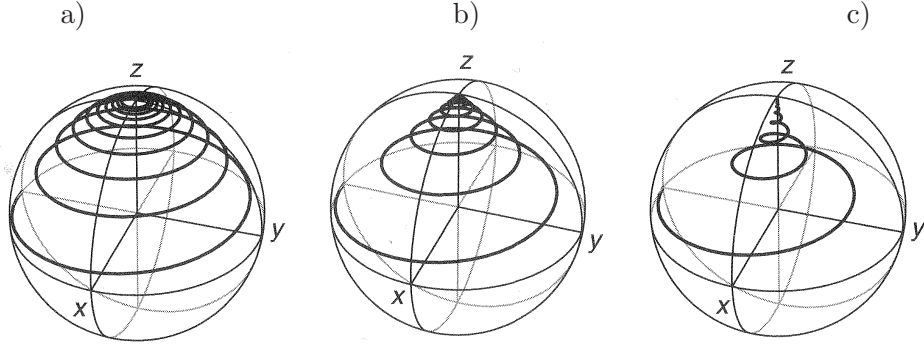


Figure 2.1: Trajectory of the relaxation process for different ratios  $\frac{T_1}{T_2}$ . a)  $2 \cdot T_1 = T_2$ , b)  $T_1 = T_2$ , c)  $T_1 = 2 \cdot T_2$ . After [Levitt \(2002\)](#)

detail concerning surface NMR see [Legchenko \(2004\)](#); [Braun \(2007\)](#))

$$\begin{aligned} M_x(t=0) &= M_0 \cdot \sin(\phi) \cos(\phi) (1 - \cos(\theta)) \\ M_y(t=0) &= M_0 \cdot \sin(\phi) \sin(\theta) \\ M_z(t=0) &= M_0 \cdot (\cos^2(\phi) + \sin^2(\phi) \cos(\theta)) \end{aligned}$$

Then equation 2.3 decouples concerning vertical and horizontal magnetisation, i.e. longitudinal ( $T_1$ ) and transverse ( $T_2$ ) relaxation to

$$\frac{dM_x}{dt} = \gamma \cdot M_y \cdot B_0 - \frac{M_x}{T_2} \quad (2.6)$$

$$\frac{dM_y}{dt} = -\gamma \cdot M_x \cdot B_0 - \frac{M_y}{T_2} \quad (2.7)$$

$$\frac{dM_z}{dt} = -\frac{M_z - M_0}{T_1}. \quad (2.8)$$

The solution to this set of equations is a damped harmonic oscillation

$$M_{x,y}(t) = M_{x,y}(0) \cdot \exp(-i\omega t) \cdot \exp(-t/T_2) \quad (2.9)$$

in the (x,y) plane (i.e. perpendicular to the static field) and (re)build of thermal equilibrium, i.e. net magnetisation

$$M_z(t) = M_z(0) \cdot \exp(-t/T_1) - M_0 \cdot \exp(-t/T_1) + M_0. \quad (2.10)$$

In total  $\mathbf{M}(t)$  describes the precession of the magnetisation around  $\mathbf{B}_0$  (Fig. 2.1), while the measurable signal is a decay at larmor frequency originating from the magnetisation component  $M_{x,y}(t)$  oscillating in the (x,y) plane at Larmor frequency.

## 2.2 Surface NMR signal

In contrast to laboratory NMR carrying the sample inside a measurement coil and using artificial primary magnetic field conditions, the object to be investigated of surface NMR is outside the coil and as primary field the earth field is used. From this “layout” additional tasks arise to get a proper set of equations describing the methods physics.

According to the earth field strength the Larmor frequency varies from 1 kHz up to 2.7 kHz. The excitation magnetic field  $\mathbf{B}_T$  is build up by large surface loops of sizes actually ranging from 10 m - 150 m. Thus, it is inhomogeneous and elliptically polarised due to the geometrical damping and subsurface resistivity. Following the description of [Weichman et al. \(2000\)](#), the emitted, in general elliptically polarised excitation field is projected on the earth’s field orientation in order to derive the component  $\mathbf{B}_T^\perp$  perpendicular to the earth’s field direction and then decomposed into two circular polarised fields (Fig. 2.2). This is necessary since only the field component that is co-rotating with the precession spin and perpendicular to  $\mathbf{B}_0$  deflects the spin from its orientation along with the earth field.

According to [Weichman et al. \(2000\)](#) (in more detail [Braun \(2002\)](#); [Hertrich et al. \(2005\)](#)) and with [Mohnke and Yaramanci \(2005\)](#) introducing multi-exponential NMR behaviour, the surface NMR signal in 3D composes to

$$d(q, t) = V(q, t) = \int G(\mathbf{r}, q) \int m(\mathbf{r}, T_2^*) \cdot e^{-t \cdot (T_2^*)^{-1}} dT_2^* d^3\mathbf{r} \quad (2.11)$$

$$\begin{aligned} G(\mathbf{r}, q) = & \sin\left(\gamma \frac{q}{I_0} |\mathbf{B}_T^+(\mathbf{r})|\right) \\ & \times \frac{2}{I_0} |\mathbf{B}_R^-(\mathbf{r})| \cdot e^{i[\zeta_T(\mathbf{r}) + \zeta_R(\mathbf{r})]} \\ & \times [\hat{\mathbf{b}}_R(\mathbf{r}) \cdot \hat{\mathbf{b}}_T(\mathbf{r}) + i \hat{\mathbf{b}}_0 \cdot \hat{\mathbf{b}}_R(\mathbf{r}) \times \hat{\mathbf{b}}_T(\mathbf{r})] \end{aligned} \quad (2.12)$$

with

$\mathbf{B}_T^+$	=	co-rotating part of the transmitter field
$\mathbf{B}_R^-$	=	counter-rotating part of the receiver field
$\mathbf{b}_0$	=	unit direction of earths magnetic field
$\hat{\mathbf{b}}_R(\mathbf{r})$	=	unit direction of virtual receiver field perpendicular to $\mathbf{b}_0$
$\hat{\mathbf{b}}_T(\mathbf{r})$	=	unit direction of the transmitter field perpendicular to $\mathbf{b}_0$
$d(q, t) = V(q, t)$	=	envelope of the voltage in the receiver loop [V]
$G(\mathbf{r}, q)$	=	kernel function, i.e. forward operator [ $V/m^3$ ]
$m(\mathbf{r}, T_2^*)$	=	partial water content distribution [ $m^3/m^3$ ]
$I_0$	=	transmitter loop current
$\tau$	=	pulse (excitation field) duration
$q = I_0 \cdot \tau$	=	pulse moment [As]
$r$	=	spatial location
$T_2^*$	=	apparent transverse decay time
$t$	=	time [s]
$\zeta_{T,R}(\mathbf{r})$	=	phase shift [rad]

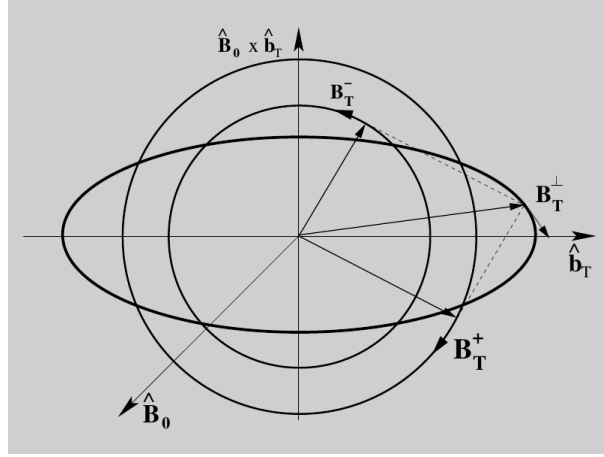


Figure 2.2: Decomposition of an elliptically polarised field  $\mathbf{B}_T^\perp$  into two opposite circularly polarised fields  $\mathbf{B}_T^+$  and  $\mathbf{B}_T^-$  (Braun, 2007). For description of all other symbols see equation 2.12

Equation 2.11 currently provides the most complete forward operator for spatial and time domain as well as for arbitrary loop positions, sizes and orientations. Commonly laboratory NMR and borehole NMR use a decay time distribution to describe the NMR relaxation behaviour of a complete sample, i.e., the partial amount of water associated with some decay time (interval). Concerning surface NMR a partial water content (PWC) distribution extends this decay time distribution by the spatial dimension as necessary for surface NMR. Ongoing from this PWC distribution the total water content as a function of depth is the sum over all decay times. This total water content is often referred to as  $\Theta$ , linking to a usual hydrogeophysical notation of water content. In addition, the logarithmic mean of the PWC distribution as a function depth, as a usually used measure for a mean decay time, is named decay time depth distribution. The spatial resolution of the subsurface PWC distribution is thereby realised by changing the parameter  $q$ , i.e. the spatial energy distribution due to the spatial distribution of the magnetic field. According to  $q = I_0 \cdot \tau$  the pulse moment is changed by changing the transmitter loop current  $I_0$ . These pulse moment changes leads to a change of the spatial distribution of excitation angles and therefore signal amplitudes. Consequently, changing  $q$  changes the spatial location of the subsurface volume creating the signal response. The kernel function  $G(\mathbf{r}, q)$  describes this “sensitive” volumes for any pulse moment  $q$ . The kernel is complex valued either due to the subsurface resistivity or separated transmitter and receiver loops. Depending on a subsurface assumption the kernel function can be integrated.

Figure 2.3 shows the kernel function for a horizontal layered earth, i.e. 1D conditions. In general, increasing the pulse moment increases the depth of the main sensitive volume. Figure 2.4 shows the kernel function in 2D, i.e. only integrating for one horizontal direction. Besides the kernel function for a coincident configuration (that is usually used for 1D exploration) a separated loop configuration (as introduced by Hertrich et al. (2005)) is shown. These two configurations significantly differ in their spatial sensitivity distribution and show different resolution properties as it will be discussed in section 5.5.

In equation 2.11 a hidden parameter is the subsurface resistivity that enters the equation via calculating the magnetic fields. Extensive research on the influence of the resistivity on the surface NMR kernel function as well as the development of an inversion schemes for the resistivity

## 2 Surface NMR Forward Problem

has been carried out by [Braun \(2007\)](#) and [Braun and Yaramanci \(2008\)](#).

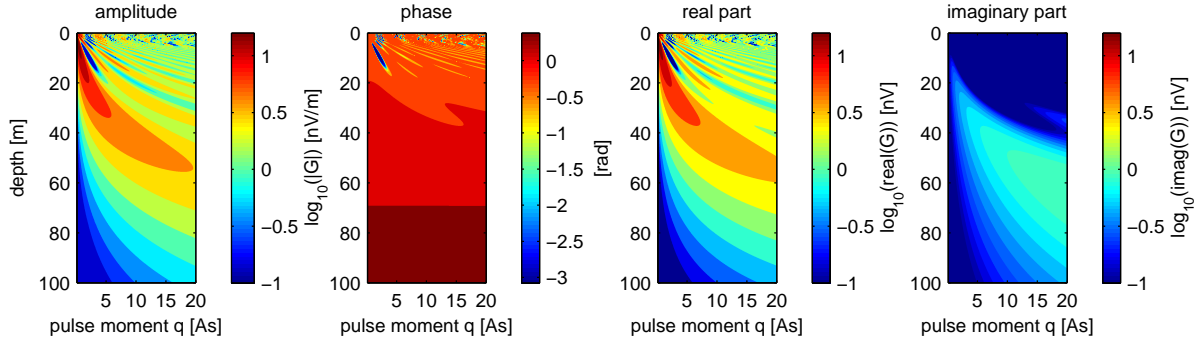


Figure 2.3: Kernel representation in 1D (horizontal integration over  $x, y$ ). Modelling parameter are: circular loop of 48 m diameter, 1 turn, 100  $\Omega m$  halfspace resistivity, earth's magnetic field with 48000 nT at  $60^\circ$  inclination. The kernel function is complex-valued due to the conductivity.

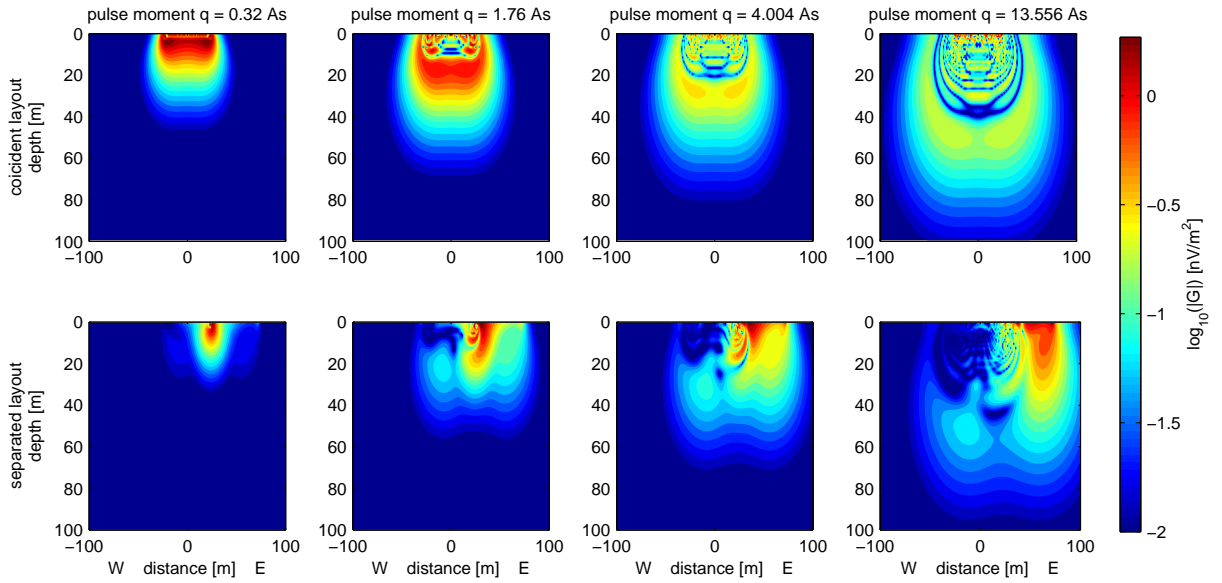


Figure 2.4: Kernel representation in 2D. Top: Coincident loop configuration equivalent to figure 2.3. Bottom: Separated loop configuration with transmitter center position is 0 m and receiver position at 48 m, i.e. the transmitter and receiver circular loop are separated by one diameter (edge to edge configuration)

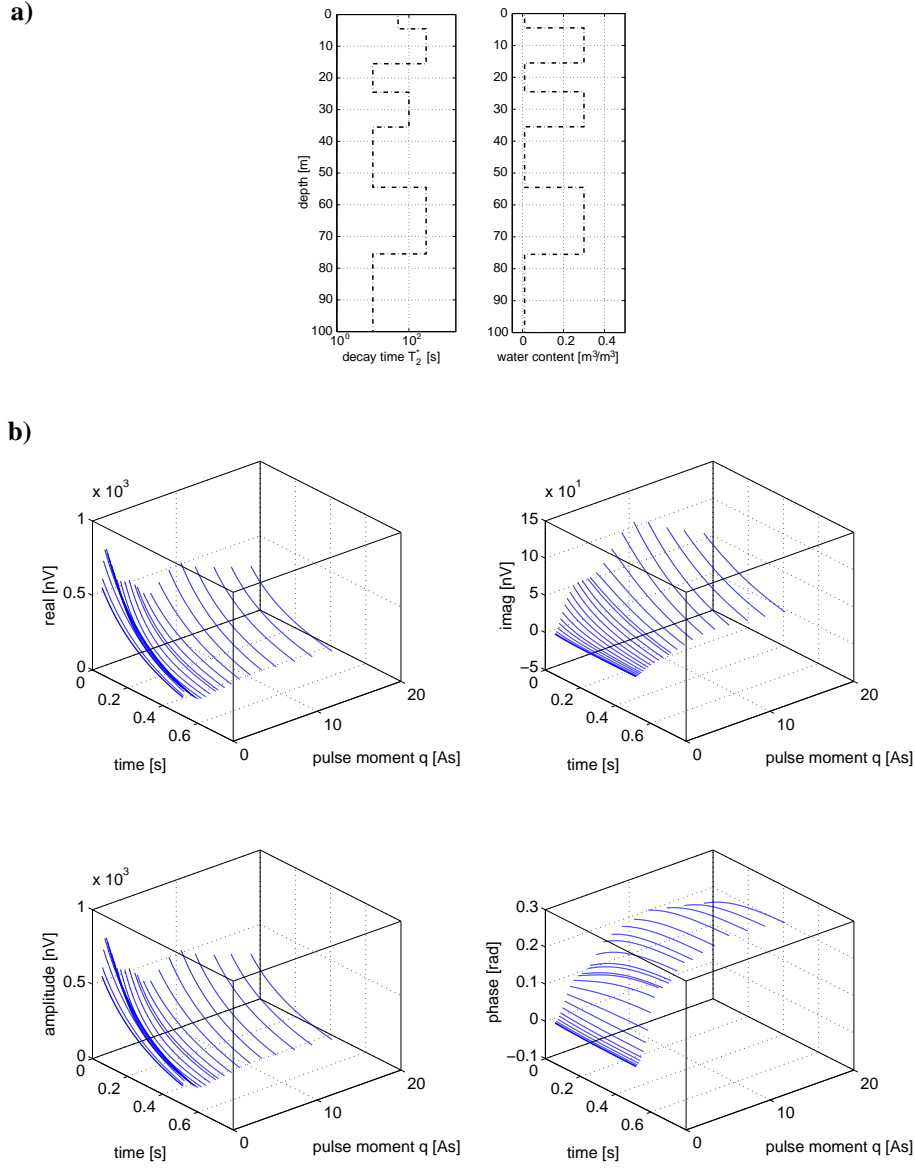


Figure 2.5: Surface NMR dataset is a measured voltage in dependency of the pulse moment  $q$  [As] and the record time  $t$  [s]. The synthetic dataset (subfigure b) is calculated using the kernel as in figure 2.3 and the subsurface model in subfigure a). The dataset might be complex for a complex kernel. Thus, it is presented in real part, imaginary part, amplitudes and phases.

Finally, the surface NMR dataset is derived by a multiplication of the subsurface PWC distribution, i.e., the water content distribution in space and decay time domain, with the kernel function and integration over the complete space and decay times, resulting in a two dimensional surface of voltages in dependency of pulse moments  $q$  and record time  $t$ . Figure 2.5 exemplary shows the surface NMR dataset for a coincident loop measurement at 1D layered earth conditions.





### 3 Surface NMR Inverse Problem - Overview

At the end of this thesis in chapter 6 the most advanced but somehow most natural inversion approach of surface NMR datasets is presented and evaluated. Thus, at chapter 6 a detailed motivation leading to this approach is given. Nevertheless, general properties like depth of investigation, resolution, field configuration, processing flows and uncertainty estimations are applied to the initial value inversion approach, too. Hence, a short derivation of possible solution strategies to the basic surface NMR equation is given beforehand and should allow the reader to follow the chapters in the given order. According to the usual matrix notation capital case bold symbols present matrices, lower case bold symbols present vectors. Commonly in geophysics the forward problem reads

$$\mathbf{d} = \mathbf{G}\mathbf{m} \quad (3.1)$$

with  $\mathbf{d}$  the data,  $\mathbf{G}$  the forward operator and  $\mathbf{m}$  the subsurface model. Since data is measured, the subsurface model is derived by multiplying the inverse operator  $\mathbf{G}^{-1}$  with the data and the inverse problem reads

$$\mathbf{m} = \mathbf{G}^{-1}\mathbf{d}. \quad (3.2)$$

In most cases the inverse problem is not that easy to pose, since it might be over determined (more data than model parameter) or underdetermined (less data than model parameter) or even of mixed condition and of great importance measured data is never exact. Therefore, an exact inverse  $\mathbf{G}^{-1}$  might not exist and we write the generalised inverse problem

$$\mathbf{m} = \mathbf{G}^{-g}\mathbf{d}. \quad (3.3)$$

with  $\mathbf{G}^{-g}$  the generalised inverse operator. Consequently, chapter 4 discussed the data, strategies of error estimation and limitation of surface NMR data in dependency of the different solution approaches (as presented next) to the surface NMR inverse problem, while in chapter 5.1.1 one solution to the problem of calculating the generalised inverse operator is discussed.

In the following three approaches that rearrange equation 2.11 to identify the data, forward operator and model are shown. Basically the approaches differ in handling the measured surface NMR dataset. As an simplification equation 2.11 is preintegrated over  $x$  and  $y$  to handle the 1D case and reads

$$d(q, t) = V(q, t) = \int G(z, q) \int m(z, T_2^*) \cdot e^{-t \cdot (T_2^*)^{-1}} dT_2^* dz. \quad (3.4)$$

**Initial value inversion:** Let's start with the integral

$$\int m(z, T_2^*) \cdot e^{-t \cdot (T_2^*)^{-1}} dT_2^* \quad (3.5)$$

as part of equation 3.4 and assume mono-exponential NMR behaviour. The partial water content (PWC) distribution then reduces to water content depth distribution  $m(z)$  at decay time depth distribution  $T_2^*(z)$

$$m(z, T_2^*) \rightarrow m(z), T_2^*(z) \quad (3.6)$$

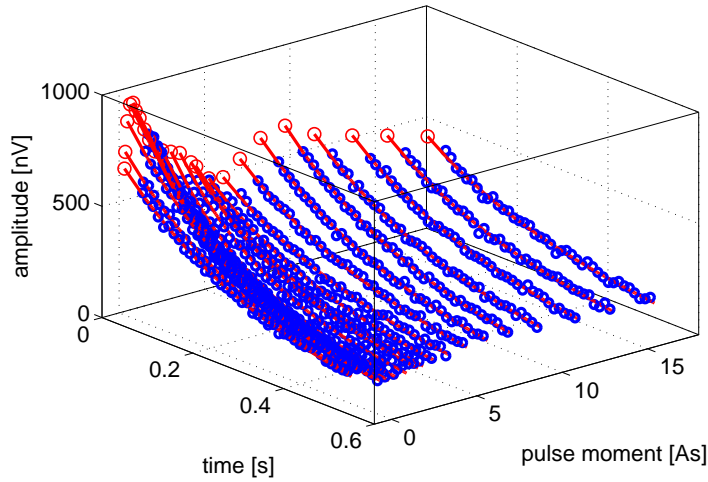


Figure 3.1: Surface NMR dataset  $d(q, t)$  with mono-exponential fit to each NMR signal  $d(q_i, t)$  (the index  $i$  indicates a certain pulse moment) for the initial value inversion. Each datum  $d(q_i, t_n)$  (the index  $n$  indicates a certain time) is represented as blue circle with mono-exponential fit to NMR signal  $d(q_i, t)$  as read line. The red circle show the extrapolation to  $t = 0$  and build as  $\mathbf{E}_0$  the sounding curve that is used for subsurface water content inversion.

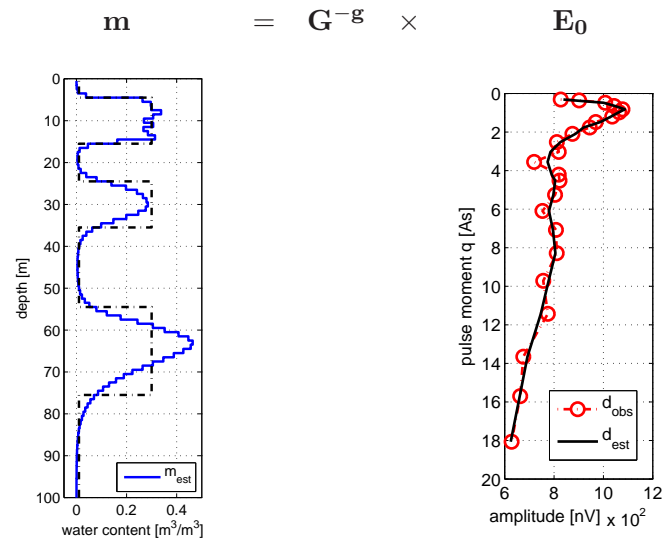


Figure 3.2: Principle of inversion for total water content distribution  $\mathbf{m}$  (black: synthetic model, blue: inversion result) using  $\mathbf{E}_0$  the initial values (red: extrapolated values as of figure 3.1, black: forward response of the estimated model) and the generalised inverse  $\mathbf{G}^{-\mathbf{g}}$  (as derived in chapter 5.1.1).

and the integral over all decay times becomes unnecessary. Thus, equation 3.4 reads

$$d(q, t) = \int G(z, q) m(z) e^{-t/T_2^*(z)} dz \quad (3.7)$$

and at  $t = 0$ , i.e. after pulse cutoff

$$d(q, t = 0) = \int G(z, q) m(z) dz = E_0(q). \quad (3.8)$$

Using a discretisation of depth  $z$  and the pulse moment  $q$ , equation 3.8 can be written as a system of linear Equations

$$\mathbf{E}_0 = \mathbf{Gm} \quad (3.9)$$

and solved for  $\mathbf{m}$ . Since  $\mathbf{E}_0$  the initial amplitudes at  $t = 0$  act as input data (called sounding curve) for the inversion, one can refer to this scheme as initial value inversion. Due to an instruments dead time, i.e., a registration of the NMR signal starting at  $t > 0$  (currently this dead time is about 40 ms) these initial values are unknown and have to be estimated in a first step.

Commonly a mono-exponential fit to  $d(q_i, t)$ , i.e., NMR signal for a certain pulse moment  $q_i$ , and extrapolation to the time  $t = 0$  as shown in figure 3.1 is used. These extrapolated initial values building the sounding curve are then used for water content inversion (Fig. 3.2). This is the common used approach to invert for water content. Chapter 5 will provide extensively insights in this type of solution and chapter 4 provides detailed knowledge of dataset preparation, fitting and error analysis.

Obviously, decay times can be derived only in dependency of the pulse moment but not as a function of depth. Mohnke and Yaramanci (2002) has presented a slightly extended scheme using the initial values and mono-exponential fitting also inverting for decay time depth distribution. This approach was neglected, since the time step inversion approach, as presented in the next paragraph, is a more enhanced strategy.

Generally spoken, the initial value inversion reduces the dataset by mono-exponential fitting to a sounding curve (solves for the NMR parameter - figure 3.1) and then inverts the sounding curve  $E_0(q)$  for the subsurface water content distribution  $m(z)$  (solves for the correct depth distribution of the NMR parameter). But mono-exponential datafit and extrapolation is not always a correct simplification, as we see next.

**Time step inversion:** Equation 3.7 shows that  $d(q_i, t)$  is of mono-exponential behaviour only if  $T_2^*(z)$  is constant for the sensitive volume shown by  $G(z, q)$ . Since the kernel function is a smoothing function the assumption is only valid for homogeneous halfspaces.

Therefore, even for mono-exponential behaviour within a subvolume the MRS recorded signal is multi-exponential due to the second part of the forward problem: the electromagnetic field propagation. Consequently, the separation has to be vice versa as presented by Legchenko and Valla (2002) and Mohnke and Yaramanci (2005). Lets start again with equation 3.5, integrate

$$\int m(z, T_2^*) \cdot e^{-t \cdot (T_2^*)^{-1}} dT_2^* = m(z, t) \quad (3.10)$$

and with equation 2.11 for a certain time  $t_n$

$$d(q, t = t_n) = \int G(z, q) m(z, t_n) dz = E_{t_n}(q) \quad (3.11)$$

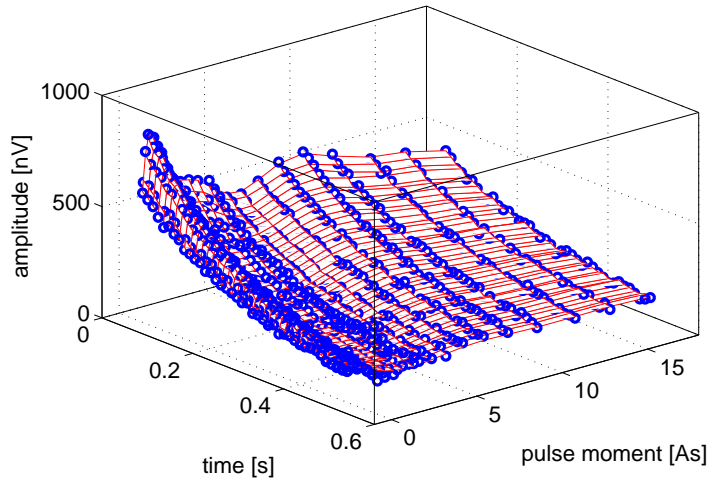


Figure 3.3: Same dataset as in figure 3.1. At every time step  $t_n$  a sounding curve  $E_{t_n}(q) = d(q, t_n)$  (the measured dataset without any exp. fitting) is inverted for water content  $m(z, t_n)$ . Thus, red lines now represent the forward response of this water content inversion of each sounding curve, separately.

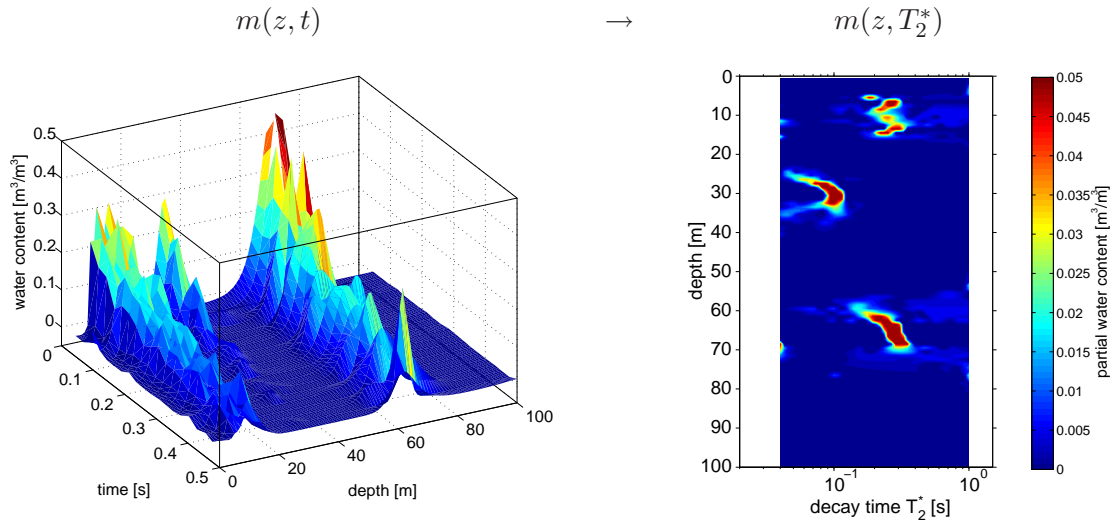


Figure 3.4: The single water content inversion  $m(z, t_n)$  builds together  $m(z, t)$ , i.e., a water content domain.  $m(z, t)$  can be fitted by a mono-exponential (to derive the total water content and the decay time) or multi-exponential approach to derive the PWC distribution  $m(z, T_2^*)$ .

Thus, the dataset  $d(q, t)$  is separated into  $E_{t_n}(q) = d(q, t_n)$  sounding curves. with  $t_n$  : a certain time sample at the NMR signal. After discretising the depth  $z$  and the pulse moment  $q$ , a system of linear equation for every time step  $t_n$  exists

$$\mathbf{E}_{t_n} = \mathbf{G}\mathbf{m}_{t_n}. \quad (3.12)$$

Consequently,  $n$  inverse problems have to be solved (as much as time steps of the NMR signal) for water content in dependency of the record time as shown in figure 3.3. After all inversion at every time step the solution for the water content builds a new structure  $m(z, t)$ . Therefore, one can call this step a transformation of the dataset into the water content domain.

The second step now either estimates  $m(z), T_2^*(z)$  (water content and decay time depth distribution) using a mono-exponential fit to  $m(z, t)$  (Legchenko and Valla (2002)) or  $m(z, T_2^*)$  (PWC distribution) using multi-exponential fit (Mohnke and Yaramanci (2005)). In any case it provides an exact solution scheme to equation 2.11.

In Mohnke and Yaramanci (2008) the approach is discussed and both synthetic and field datasets are presented. In chapter 6 this scheme is used to compare time step inversion results to the initial value and QT inversion. Generally spoken, the time step inversion solves first for the correct depth distribution and therefore resolves apparent multi-exponential signals and then solves for the NMR parameter. Thus, it provides both water content and decay time.

**QT inversion:** Both two step schemes have a drawback. To get an exact solution the first scheme has to use multi-exponential fitting of not necessarily multi-exponential NMR signals that might cause instability as discussed in section 4.2.1. The second scheme has to solve numerous linear equation systems. Both solve equations independently that share information, i.e., the subsurface parameter distribution. Since both steps (exponential fitting and water content estimation) are ill-posed, an appropriate regularisation for the final parameter distribution is fairly difficult.

To avoid these problems equation 2.11 can be rewritten to

$$d(q, t) = \int G(z, T_2^*, q, t) m(z, T_2^*) dT_2^* dz. \quad (3.13)$$

Hence, the standard kernel function is extended by the NMR decay signal to solve the complete problem. Discretising equation 3.13 spatially and for  $T_2^*$  leads to standard linear equation system of one spatial and one time dimension

$$\mathbf{d} = \mathbf{G}\mathbf{m}. \quad (3.14)$$

Thus, a fit to the complete dataset  $d(q, t)$  is calculated at one step (Fig. 3.5). The new scheme is tested with synthetic (Chapter 6) and field examples (Chapter 7) and compared to the initial value inversion and time step inversion, respectively. Figure 3.6 summarises the different approaches as an overview.

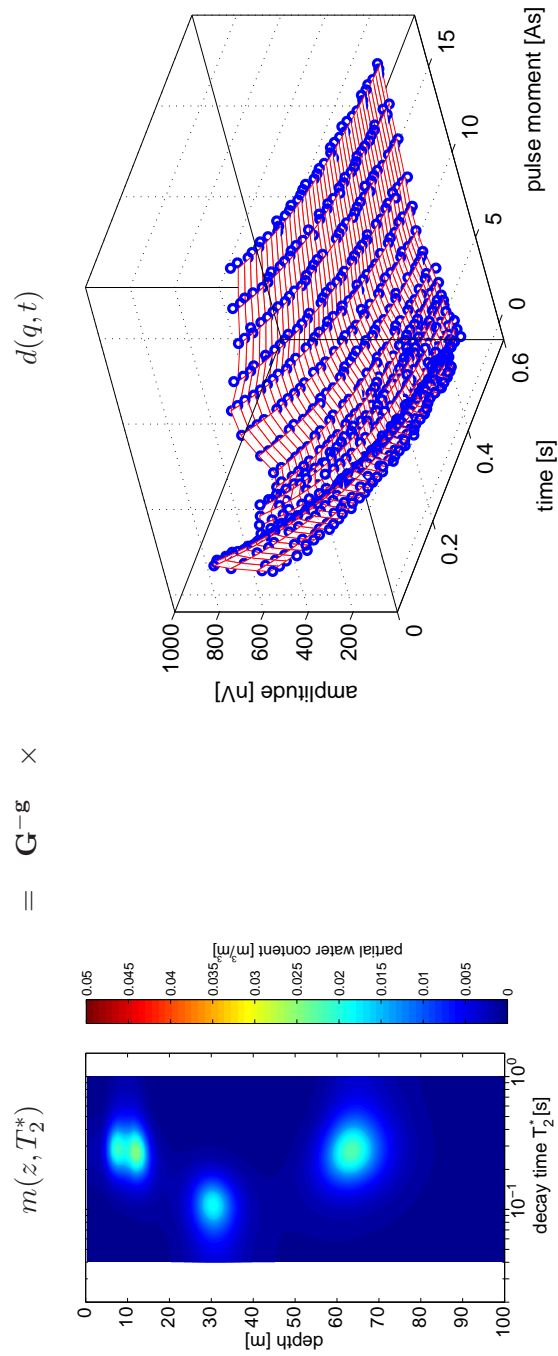


Figure 3.5: Same dataset (blue circles) as in figure 3.1. The red mesh represents the forward response of the estimated subsurface PWC distribution  $m(z, T_2^*)$  after QT inversion and satisfies the complete dataset, i.e., all data  $d(q_i, t_n)$  are taken into account jointly.

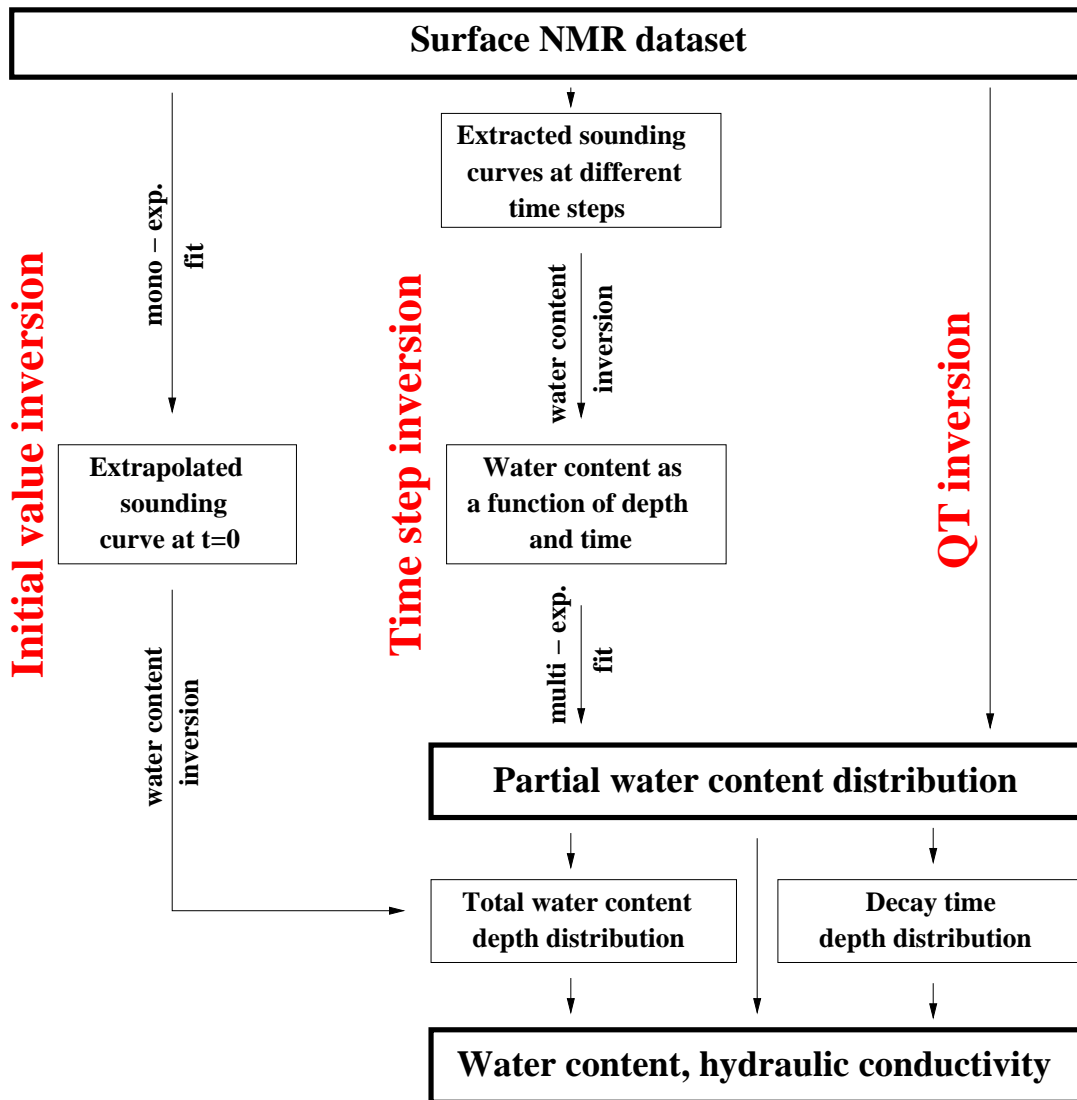


Figure 3.6: Overview on the different solution approaches.





## 4 Surface NMR Dataset

After an overview of solution approaches to the inverse problem identifying the different kinds of data as input parameter for the different inversion schemes (e.g. exponential fitting to provide initial values) and prior to analysing inversion schemes dependent resolution and stability properties (Chapter 5/6) the measured surface NMR dataset is focused in-between these chapters. Data is analysed before discussing inversion aspects due to the fact that measured data builds the base of all forthcoming steps. At this, data is handled not only as input parameter for the inversion but defining the need (and strength) of regularisation due to noisy data. Consequently, a proper regularisation of the inverse problem has to base on a detailed data error analysis. First, this chapter shows how data error is estimated and how this might vary depending on processing schemes (e.g. mono-, bi- or multi-exponential fitting) and/or processing steps. Second, uncertainties arising from systematic data error are analysed. Here systematic errors are defined as errors that do not directly influence the inversion quality in terms of a proper solution to the inverse problem, i.e., the estimated data fits very nicely the measured data, but may not fit geological expectations or lead to geological misinterpretation. Due to the different needs of data processing for different inversion schemes the sections are structured to discuss scheme independent influences, i.e., firstly common processing steps and secondly forthcoming steps for initial value inversion and QT inversion. Consequently, the given structure of sections is a roadmap for processing a dataset for inversion and evaluating the dataset concerning its reliability as well as providing fundamental understanding of surface NMR datasets.

## 4.1 Inversion scheme independent dataset processing

The surface NMR dataset following equation 2.11 is of 2 dimensions:

1. The pulse moment  $q$  that defines the spatial location of the sensitive volume
2. The time  $t$  carrying the surface NMR signal (free induction decay - FID) arising from the sensitive volume

In general, for 2D or 3D exploration (MRT) the loop position is varied and the spatial sensitivity distribution, i.e., kernel function, is a function of the loops spatial location and the pulse moment  $q$ , as well as the loop geometry, subsurface resistivity and earth field conditions. Without loss of generality, basic dataset processing steps can be shown at the 1D dataset, i.e. independent of the loop location and only as a function of  $q$ . Such a MRS dataset is exemplarily shown in figure 4.1 for 24 pulse moments and a record time of 0.5 s.

The amplitude of the surface NMR signal is mostly smaller than the mean level of Gaussian distributed noise. Consequently, the measurement for a specific fixed pulse moment is repeated and stacked to enhance the signal quality. This approach is well known and enhances the signal to noise ratio by the square root of the stacking number.

Due to the 2 dimensions of the MRS dataset 2 measurement schemes exist. On the one hand, the same pulse moment is repeated until a necessary stack number is reached and then one switches to the next higher pulse moment. On the other hand, all pulse moments are recorded successively until the maximum pulse moment is reached and then restart with the smallest pulse moment for stacking. Both schemes are currently applied in different devices. But at least

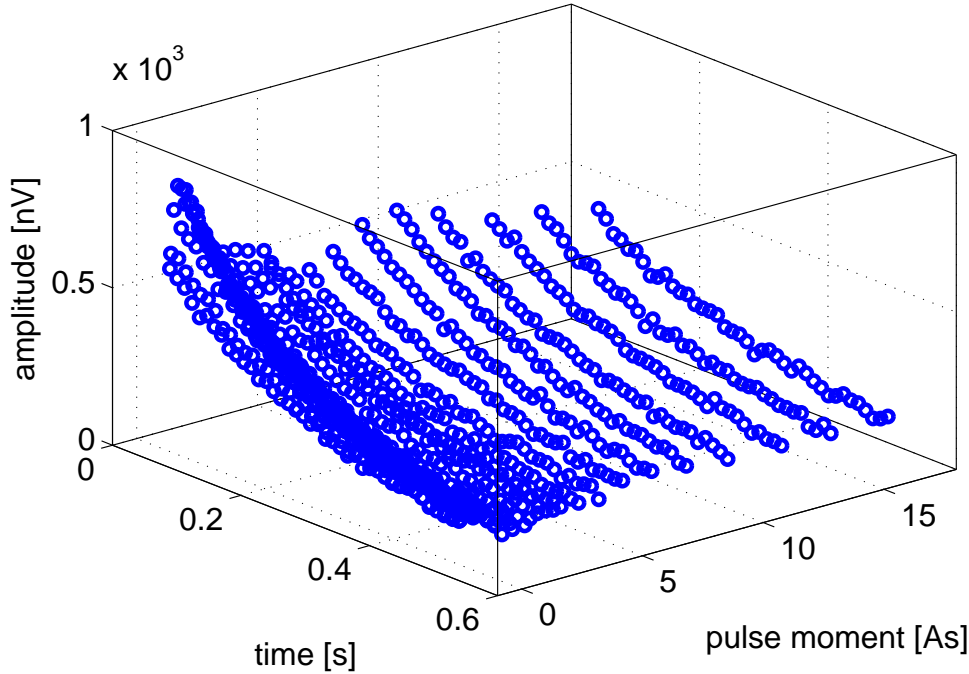


Figure 4.1: MRS dataset of a single sounding. Surface NMR signals are recorded for 0.5 s and for 24 pulse moments representing different sensitive volumes.

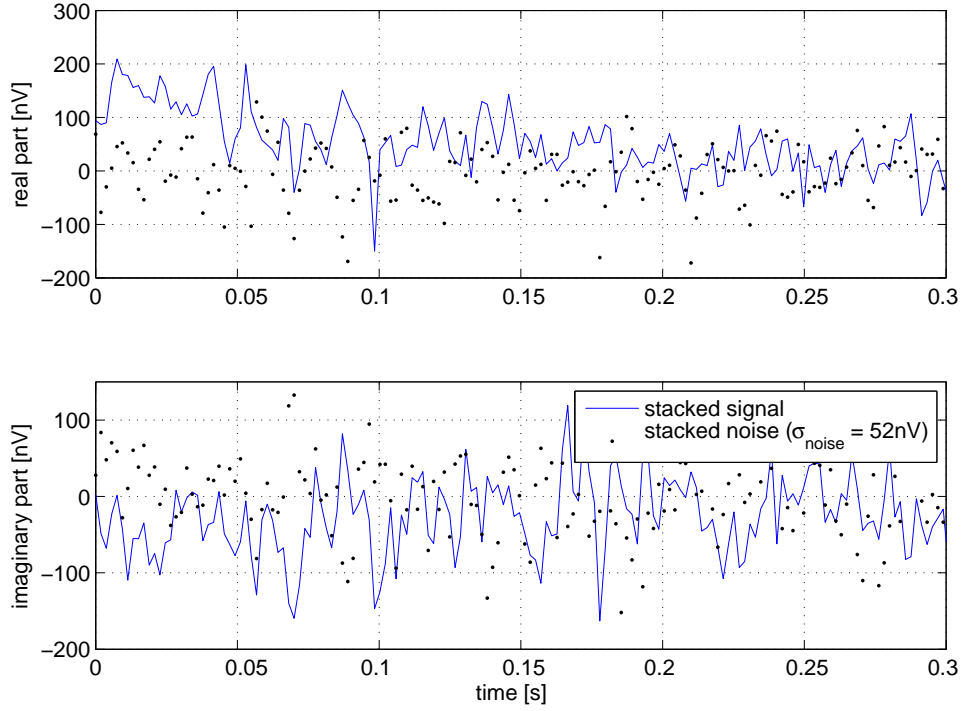


Figure 4.2: Stacked surface NMR signal (recorded in Ahrenshop, Germany) based on 164 single stacks without despiking. The stacked noise also consists of 164 stacks. Even at the stacked surface NMR signal spike events (e.g. at 0.095 s) are visible.

both schemes have to stack the single records of each pulse moments.

Unfortunately, besides Gaussian distributed noise, spike events often occur due to electromagnetic events like natural short time variation, pulsations or lightnings but also artificial events caused by trains or mobile communication. These events do not destroy a single stack but if the occurrence repeats during many single stacks the stacked signal can be totally corrupted.

A often used scheme is to filter these events using some low-pass filter. Concerning surface NMR signals this approach is difficult due to the surface NMR signals spectrum and has to be done adaptively for any dataset. Anyhow, systematic errors might be introduced according to [Strehl \(2006\)](#). Another approach evaluated by [Strehl \(2006\)](#) are wavelet based spike eliminations that promise very good results but need further development and evaluation.

Here, a very easy and robust scheme is presented. It is based on deleting spike affected parts of a single stack rather than to filter (or delete) the complete single stack. Figure 4.2 shows a signal, recorded near Ahrenshop (Germany), containing 164 stacks without deleting spike events, i.e., all 164 single stacks for this pulse moment are stacked to one signal.

Figure 4.3a shows all 164 single stacks. Spike events are easily visible and corrupt the stacked surface NMR signal (Fig. 4.2, e.g. at 0.095 s). But clearly not a complete single stack is affected by increased noise condition. Consequently, one would delete valuable information, if the whole single stack is deleted.

Lets extract e.g. from each single stack the complex value at 0.2 s after pulse cutoff. One gets a dataset of 164 data points (Fig. 4.3b) virtually repeating a measurement of exactly the same time sample of the surface NMR signal. Spike events are still clearly visible. Next, a statistical analysis can be applied. Therefore, the standard deviation for these 164 measurements is cal-

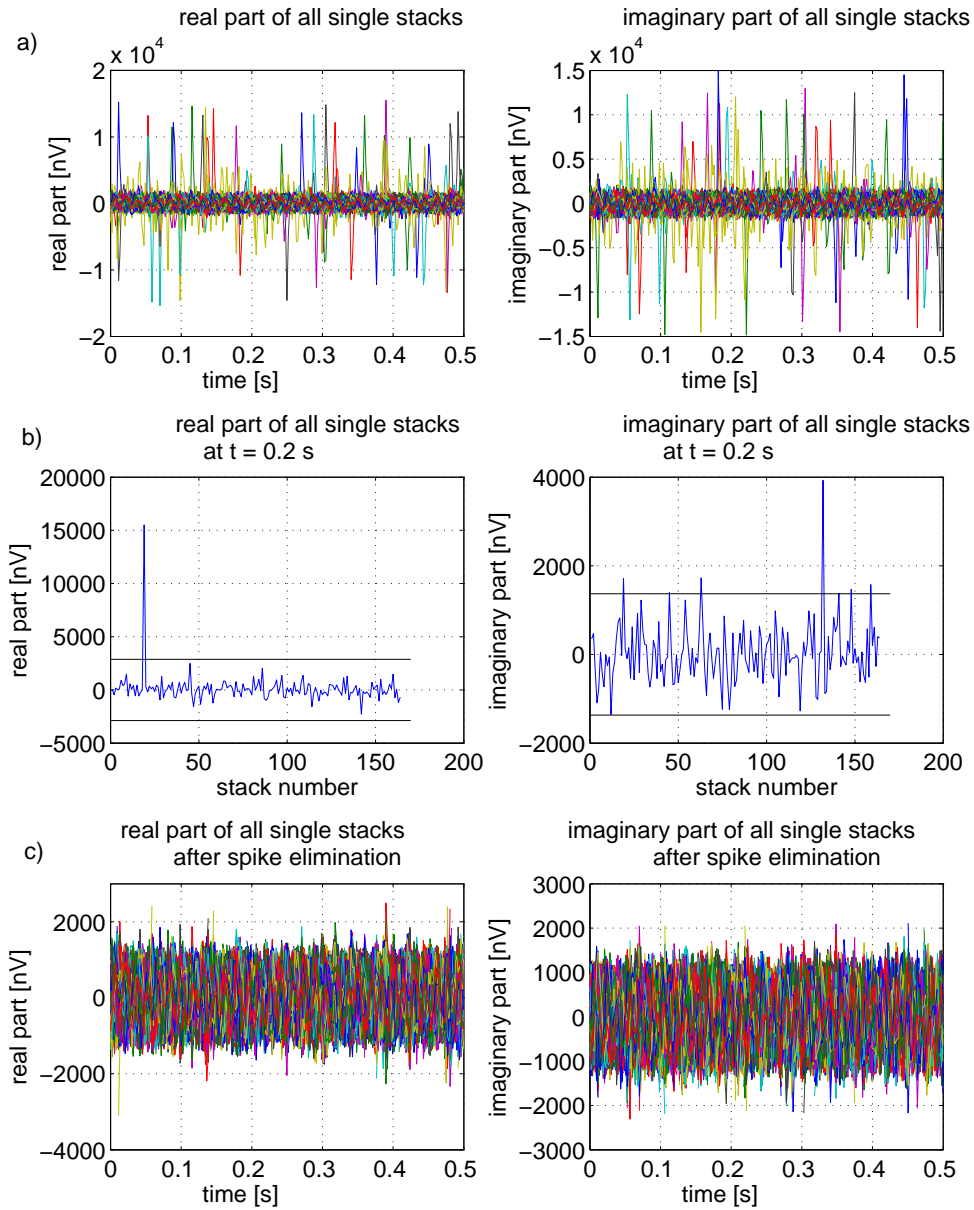


Figure 4.3: a) 164 single stacks in real and imaginary part. b) Extracted real and imaginary part of these 164 single stacks at a fixed time (0.2 s), i.e., a dataset of 164 repeated measurements. The black lines are twice the standard deviation, calculated from this dataset. Spikes can be easily identified and only single measurements of these 164 stacks at each time sample are deleted instead of the whole single stack. c) Remaining 164 single stacks after spike elimination.

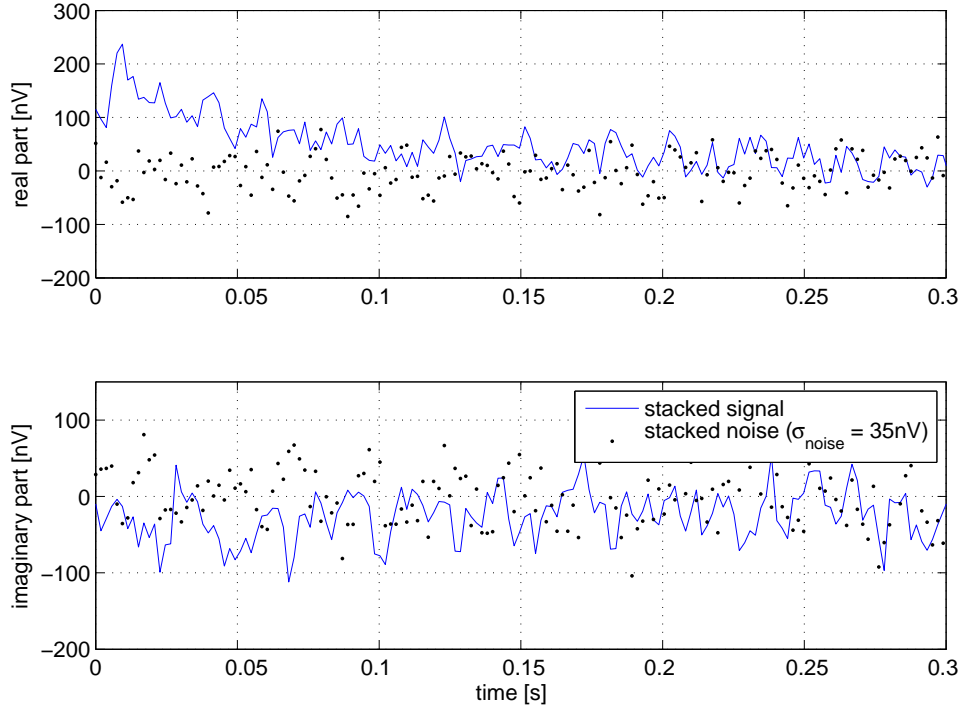


Figure 4.4: Stacked surface NMR signal (recorded in Ahrenshop, Germany) based on 164 single stacks with despiking.

culated. The black lines then indicate an interval of twice the standard deviation, i.e., within 95% confidence interval. Obviously, spike events do not fit into this interval and thus, can be detected and deleted. This approach is successively repeated for all available time samples.

Consequently, not a complete single stack is deleted, if a spike occurs during the record. Only the spike of the single stack is deleted and the remaining time samples are still used for stacking. Figure 4.3c shows the remaining part of all single stacks that are then used to calculate the stacked surface NMR signal as presented in figure 4.4.

In order to calculate the improvement on the signal to noise ratio, exemplarily this schemes is applied to the noise record as well. The noise record also consists of 164 stacks, each recorded directly before the signal. Deleting the spike events before stacking clearly improves the signal by a factor of 2 (Fig. 4.4).

## 4.2 Dataset processing and error estimations for initial value inversion

### 4.2.1 Dataset exponential fitting and extrapolation

The essential processing step using the initial value inversion is to calculate the NMR complex value at an appropriate time  $t$  that corresponds to the maximum amplitude, i.e.,  $90^\circ$  excitation angle. While most extrapolation approaches (see [Legchenko and Shushakov \(1998\)](#), [Mohnke and Yaramanci \(2002\)](#)) refer to the time after excitation pulse cutoff as initial value, [Weichman et al. \(2000\)](#) proposes an extrapolation within half the pulse length but neither proved or evaluated this proposal. In 2009 ([Walbrecker et al., 2009](#)) has proven this concept. Due to the late proof, here the time after excitation pulse is used. But since it has no essential influence on the approach of extrapolation and error estimation the results are transferable.

Depending on the general concept of petro-physics, application range or data feasibility, different extrapolation schemes are available. In laboratory and borehole applications a multi-exponential approximation of the NMR signal is common sense, while in MRS applications both mono-exponential (as standard approach) and multi-exponential approximation ([Mohnke and Yaramanci \(2005\)](#)) schemes exist. [Mohnke and Yaramanci \(2005\)](#) had shown that for multi layered subsurface structures with different relaxation regimes the surface NMR signal is necessarily multi-exponential.

Besides this, a surface NMR signal is complex due to frequency offsets and phase effects. Thus, the complex surface NMR signal is usually fitted according to [Legchenko and Valla \(1998\)](#), i.e., using real and imaginary part of the signal instead of amplitudes. Taking only the amplitudes into account, i.e., neglecting phase and frequency offsets leads to a biased solution. In the complex case four parameter: initial amplitude  $x_1$ , decay time  $x_2$ , phase  $x_3$  and frequency offset  $x_4$ , are necessary to completely describe a complex mono-exponential signal  $V(t)$

$$\Re(V(t)) = x_1 e^{-tx_2^{-1}} \cos(2\pi x_4 t + x_3) = V_R(t) \quad (4.1)$$

$$\Im(V(t)) = x_1 e^{-tx_2^{-1}} \sin(2\pi x_4 t + x_3) = V_I(t) \quad (4.2)$$

In order to determine these four parameters, at least two complex measurements (at different times  $t_1$  and  $t_2$ ), i.e., four datapoints  $\{V_R(t_1), V_I(t_1), V_R(t_2), V_I(t_2)\}$  are necessary. Lets write equation 4.1 and 4.2 using these four datapoints:

$$V_R(t_1) = x_1 e^{-t_1 x_2^{-1}} \cos(2\pi x_4 t_1 + x_3) \quad (4.3)$$

$$V_I(t_1) = x_1 e^{-t_1 x_2^{-1}} \sin(2\pi x_4 t_1 + x_3) \quad (4.4)$$

$$V_R(t_2) = x_1 e^{-t_2 x_2^{-1}} \cos(2\pi x_4 t_2 + x_3) \quad (4.5)$$

$$V_I(t_2) = x_1 e^{-t_2 x_2^{-1}} \sin(2\pi x_4 t_2 + x_3) \quad (4.6)$$

and rearrange in order to solve for  $\{x_1, x_2, x_3, x_4\}$ .

First, eliminate  $x_1$  in equation 4.3 and 4.5 using 4.4 and 4.6, respectively.

$$\frac{V_I(t_1)}{V_R(t_1)} = \tan(2\pi x_4 t_1 + x_3) \quad (4.7)$$

$$\frac{V_I(t_2)}{V_R(t_2)} = \tan(2\pi x_4 t_2 + x_3) \quad (4.8)$$

This yields the phase  $x_3$  and frequency offset  $x_4$ .

Second, using the known  $x_3$  and  $x_4$  equation 4.3 and 4.5 leads to

$$\frac{V_R(t_1)}{\cos(2\pi x_4 t_1 + x_3)} = x_1 e^{-t_1 x_2^{-1}} \quad (4.9)$$

$$\frac{V_R(t_2)}{\cos(2\pi x_4 t_2 + x_3)} = x_1 e^{-t_2 x_2^{-1}} \quad (4.10)$$

and yields the amplitude  $x_1$  and the decay time  $x_2$ . Obviously, the parameter determinations decouples into calculating the phase and frequency first and second the amplitude and decay times. This has some consequences if data uncertainties are taken into account. After equation 4.7 and 4.8 any misestimation of the phase is compensated by a frequency offset misestimation according to the data uncertainty. That is, phase and frequency offset are correlated. On the other hand, after equation 4.9 and 4.10 amplitude and decay time estimation are correlated.

Furthermore, due to the correlation of phase/frequency offset and the decoupling of the parameter determination, the amplitude/decay time estimation is independent and uncorrelated with the phase/frequency offset estimation.

In the following three fitting approaches are compared and evaluated for its use and feasibility for estimating MRS initial amplitude and decay time (or decay time distribution). According to the correlation analyses the synthetic modelling was carried out neglecting phase and frequency offsets, i.e., phase and frequency offset is set to zero and only the real part of signal is used. Remark, for real field data the complex fitting is necessary to avoid biased solutions.

The approaches to compare are:

1. Mono-exponential
2. Bi-exponential
3. Multi-exponential

Be aware, the focus of this evaluation is on fitting results in dependency on the signal to noise ratio and discussed independent of a petro-physical model.

A signal with two exponentials is generated and contaminated with two noise levels related to laboratory and moderate field signal quality. Here, noise level defines the standard deviation of a Gaussian distribution.

Furthermore, all synthetic signal are at a sampling frequency of 500 Hz that is equivalent to the surface NMR field signals.

Figure 4.5 shows the modelling parameters, the noise contaminated signal and the different fitting results. Both, the multi- and bi-exponential approach can explain the data adequately while the mono-exponential fit is just able to resolve a mean of the two decay times and therefore underestimates the total amplitude. Figure 4.6 presents the results with increased noise conditions that are equivalent to moderate surface NMR field conditions. For this case all approaches show deviations for the total amplitude within the same range. Concerning multi- and bi-exponential fitting the amplitude is overestimated due to wrong decay time estimations, i.e., the fitting process is very noise sensitive. The mono-exponential fit underestimates the total amplitude but the estimated decay time still presents a mean of the two exponentials.

Second, a mono-exponential signal with the total amplitude (1000 nV) and mean decay time (0.3 s) of the previous experiment at field scale noise level (100 nV). Table 4.1 lists the fitting results including the standard deviation derived from 100 independent runs of signal creation and fitting. Obviously, the mono-exponential approach represents the synthetic model with

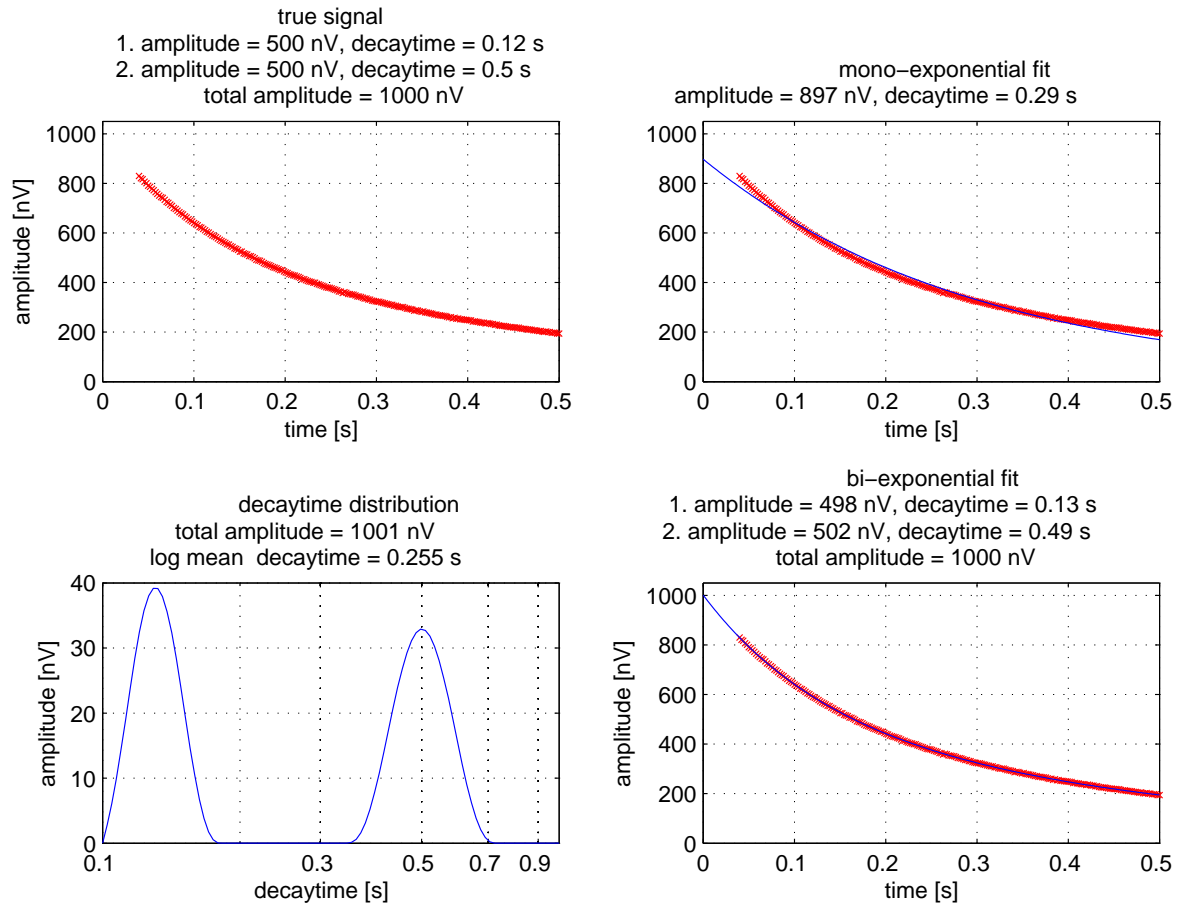


Figure 4.5: Comparison of exponential fitting approaches at laboratory noise level (1nV). Synthetic signal consists of two exponentials at the same initial amplitude of 500 nV but different decay time (0.12 s and 0.5 s). Upper right corner: mono-exponential fit and signal, Lower right corner: bi-exponential fit and signal, Lower left corner: decay time distribution of the multi-exponential fit.



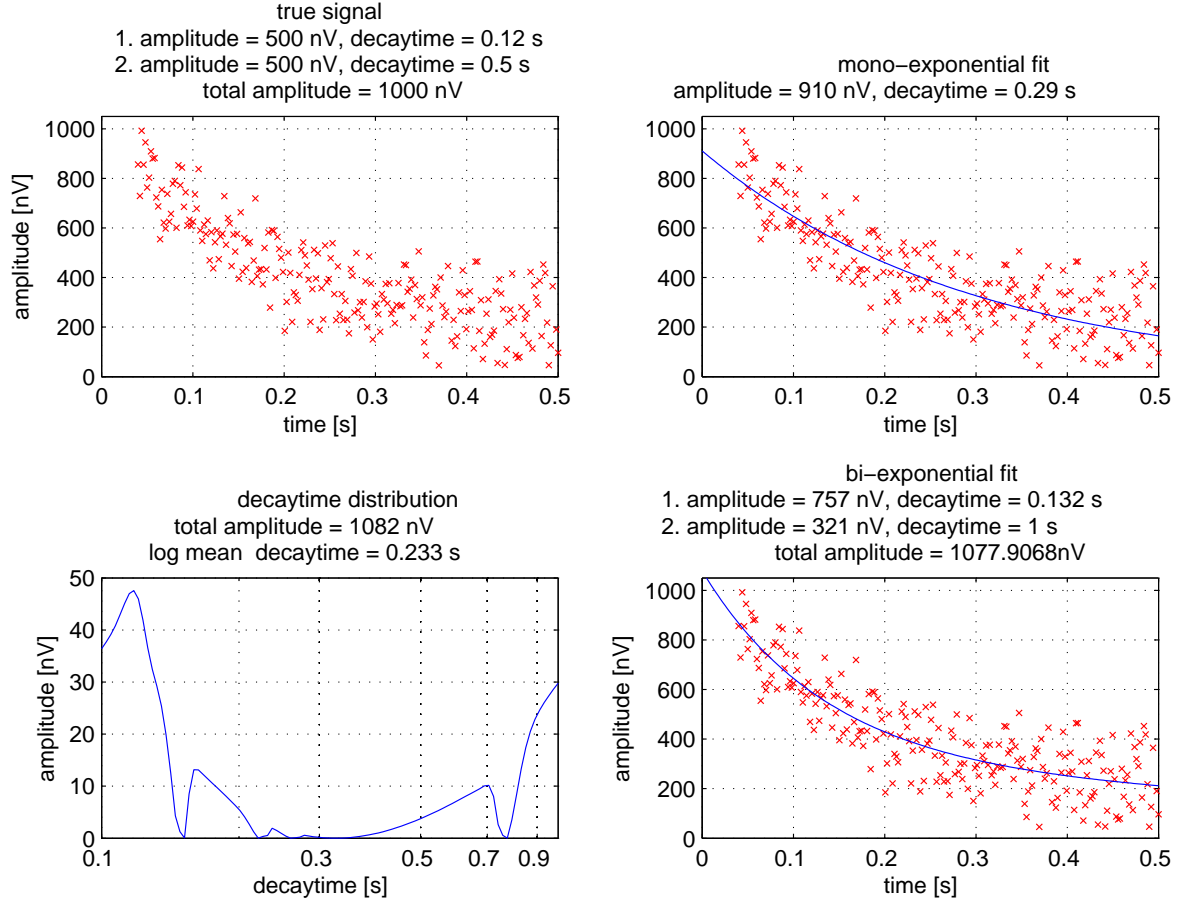


Figure 4.6: Comparison of exponential fitting approaches at moderate field noise level (100 nV). Synthetic signal consists of two exponentials at the same initial amplitude of 500 nV but different decay time (0.12 s and 0.5 s). Upper right corner: mono-exponential fit and signal, Lower right corner: bi-exponential fit and signal, Lower left corner: decay time distribution of the multi-exponential fit.

	mean initial amplitude $\pm$ std	mean decay time $\pm$ std
mono-exponential fit	1001 nV $\pm$ 26 nV	0.29 s $\pm$ 0.01 s
bi-exponential fit	1018 nV $\pm$ 38 nV	0.36 s $\pm$ 0.14 s
multi-exponential fit	1030 nV $\pm$ 33 nV	0.29 s $\pm$ 0.015 s

Table 4.1: Comparison of exponential fitting approaches at moderate field noise level (100 nV). Synthetic signal consists of a single exponential at 1000 nV initial amplitude and 0.3 s decay time). The standard deviations of the fitting parameters are calculated from 100 independent runs.

less deviation due to the limited free model parameters compared to multi- and bi-exponential approach.

In conclusion, multi-exponential fitting routines using several exponential decay functions are able to represent complicated models at favourable noise condition in laboratory application but have to be carefully chosen for MRS field measurements due to unfavourable noise conditions. In fact, no inversion scheme for MRS datasets uses a multi-exponential fit at surface NMR signal domain. In general, these results cannot be passed directly to a signal fitting in water content domain as used in the time step or QT inversion since cross signal correlations and inversion stability changes the signal to noise ratio at that domain.

#### 4.2.2 Dataset error estimations

**Calculating the error estimation:** As shown in subsection 4.2.1 the mono-exponential fit is to be preferred to approximate the initial value. Hence, the following subsection presents error estimation based on this approach. Later this results will be used for the initial value inversion as input parameter. Remark, now and for all following discussions the complex fitting for all four parameter (including phase and frequency offset) is applied.

Concerning NMR signals one has to distinguish between: error estimations for each datum of the measured time series (as being discussed in subsection 4.3) and for the extrapolated initial values as discussed in the following.

In order to estimate the error of the extrapolated initial value one has to take two steps into account. First, the covariance of the fitting result is discussed. Let  $\sigma_k$  be the standard deviation of a certain measurement  $k$  in the time series and  $\sigma$  it's mean. Then for  $n$  model parameter  $m$  the covariance matrix related to the fit is defined as

$$\mathbf{C}^m = \sigma^2 (G^T G)^{-1}. \quad (4.11)$$

with  $G$  the forward operator and  $\mathbf{C}^m$  the  $n$  by  $n$  element covariance matrix.

Second, the amplitude extrapolation is considered as an error propagation with dependent model parameters, i.e.  $\mathbf{C}_{ij}^m$  with  $i \neq j$  is not zero. If  $m_{extr} = f(m)$  is the extrapolated value and following Taylor (1982), the model standard deviation for two model parameter (amplitude and decay time) reads

$$\sigma^{m_{extr}} = \sqrt{\left(\frac{\partial f}{\partial m_1}\right)^2 \mathbf{C}_{11}^m + \left(\frac{\partial f}{\partial m_2}\right)^2 \mathbf{C}_{22}^m + 2 \left(\frac{\partial f}{\partial m_1}\right) \left(\frac{\partial f}{\partial m_2}\right) \mathbf{C}_{12}^m}. \quad (4.12)$$

Corresponding to subsection 5.1.1 the regularisation parameter can be chosen according to the discrepancy principle that calculates a proper regularisation parameter depending directly on

## 4.2 Dataset processing and error estimations for initial value inversion

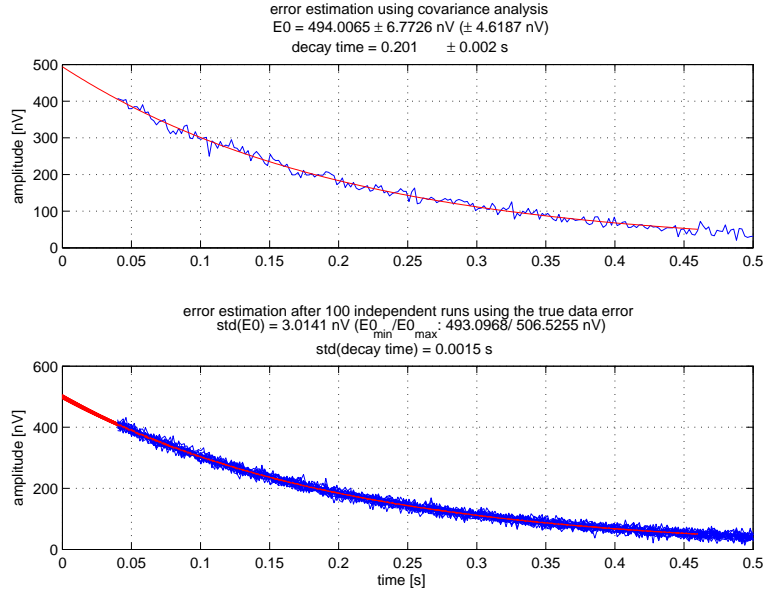


Figure 4.7: Comparison of different error estimations. True signal: Initial amplitude 500 nV, decay time 0.2 s. Top: Error estimation based on the covariance calculation for a single signal with Gaussian distributed noise at standard deviation of 10 nV. The fitted initial value and its standard deviation is given using the Gaussian error propagation as well as (in brackets) the standard deviations before extrapolation. Bottom: Standard deviation (and max/min values) calculated from 100 independently noise contaminated signals.

the error estimation of the measured data. An accurate calculation of the data error based on equation 4.12 will lead to optimal regularisation only if all error estimation are perfectly known and follow the Gaussian distribution, that is rarely given. Otherwise, an over- or under-regularised solution is finally calculated. Thus, it is useful to derive an error estimation that ensures an upper limit independent if parameter covariances exist or not. This solution then is, by definition, not under-regularised. The Gaussian error propagation is used to ensure such an upper limit and derived from equation 4.12 by applying the Schwarz inequality

$$|\mathbf{C}_{12}^m| \leq \sqrt{\mathbf{C}_{11}^m} \sqrt{\mathbf{C}_{22}^m} \quad (4.13)$$

leading to

$$\sigma^{m_{extr}} = \sum_{i=1}^n \left| \frac{\partial f}{\partial m_i} \right| \cdot \sqrt{\mathbf{C}_{ii}^m}. \quad (4.14)$$

**Verification of the calculated error:** In order to prove the calculated error estimations the covariance analysis is compared to a statistical analysis using independent runs. It turns out (Fig. 4.7 and 4.8) that the estimated standard deviations based on the Gaussian error propagation are, as expected, mostly larger compared to the statistically calculated standard deviations based on 100 independently contaminated and fitted signals. But, according to figure 4.7 and 4.8 the estimated error including Gaussian error propagation explains the maximum deviation of the 100 statistical runs too, and therefore avoids an under-regularised solution. On the other

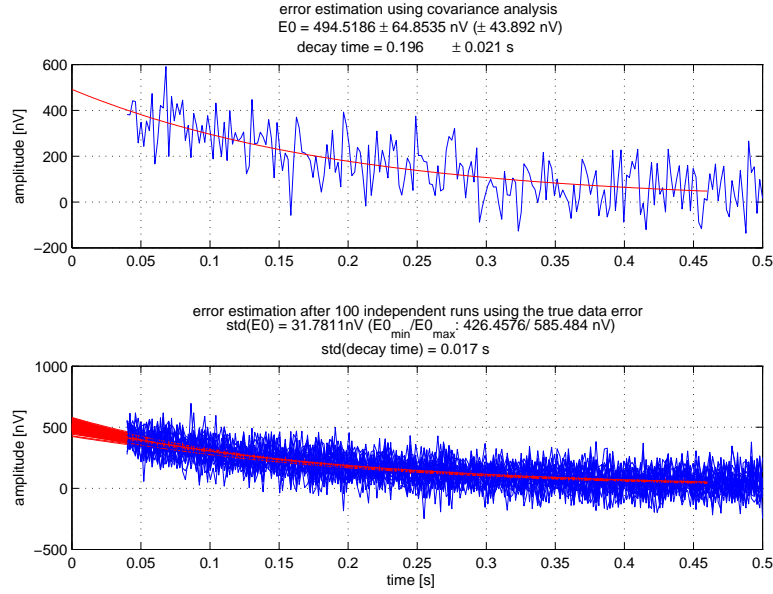


Figure 4.8: Top: Same as figure 4.7 but Gaussian distributed noise at standard deviation of 100nV.

hand, neglecting the error propagation completely may underestimate (Fig. 4.7) the error. Consequently, these two estimations define the upper and lower limits of a valid error estimation to be used for inversion. In order to avoid over-interpreted results (or under-regularised models) the error estimation taking the Gaussian error propagation into account will be used by default. In chapter 7 inversion results according to this interval will be presented and discussed. Estimating a reliable data error is essential for calculating reliable inversion results as well as resolution properties. To evaluate these error estimates besides the successful synthetic modelling, field data test are essential. In order to prove the use of the error estimation with field data, three criteria are tested.

1. Repeated measurements should be within the estimated error interval
2. Inversion results regularized using the estimated error should represent the subsurface at a well known test site
3. Fitting error of an automatically regularised inversion scheme should be in the same range as the estimated error.

First, a field experiment was carried out based on 3 repeated measurements. The results are shown in figure 4.9. It turns out that both the amplitudes and decay times can be repeated within the calculated range based on the covariance analysis while the phases appear not to be repeatable. As a restriction concerning the measured phases it should be stated that no phase correction as published in Legchenko (2004) or Braun (2007) was applied. All authors documented an antisymmetric correlation of the frequency offset to the measured phase. This is obviously not the general case here. Besides the proposed phase correction that is based on the frequency offset causing a different spin dynamic also filter properties of the resonance circuit may cause large phase misinterpretation. Consequently, in order to interpret the MRS phase by default further evaluation is necessary and only amplitudes are used in the following.

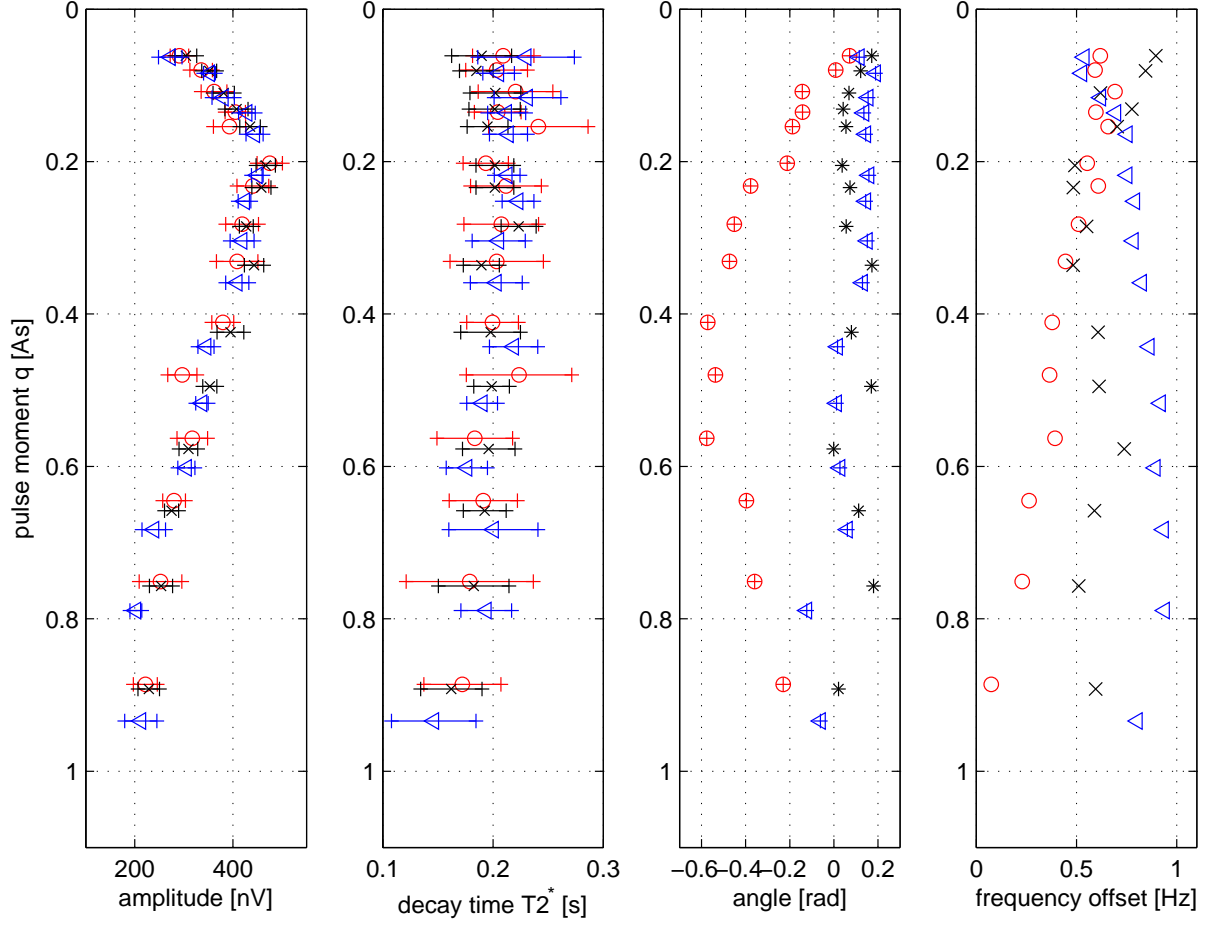


Figure 4.9: Repeatability of MRS data and reliability of error estimations. Red/ Blue and Black marks 3 measurements and its covariance based error estimations at the same location with exactly the same layout measured within 1 1/2 days.

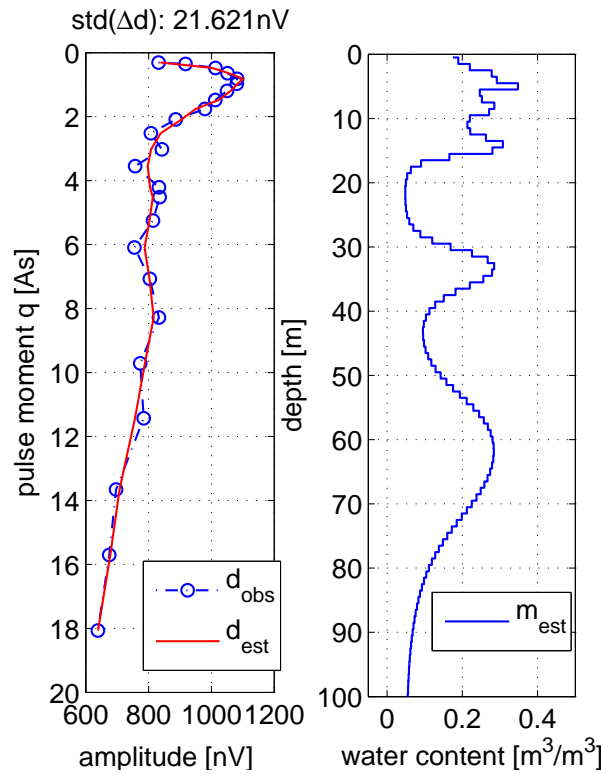


Figure 4.10: Field measurements at the test site Nauen. Settings:  $d = 100$  m loop diameter, larmor frequency at 2089 Hz, earth field inclination at  $64^\circ$ . The inversion results are discussed in section 7 in detail.

This results can be confirmed by the results presented in [Braun et al. \(2003\)](#). The authors carried out a series of repeated measurements at different test sites but changed the pulse duration since one of the aims of that research was to show this dependency. Beside this they showed similar results concerning phase behaviour and, in the context of repeatability, reliable decay times. Remark, repeatability in this context includes an unchanged loop position. There are datasets measured at locations with comparable hydrological parameters but showing different (repeatable) decay times.

Second, a measurement at a well known test site Naunen ([Yaramanci et al. \(2002\)](#)) was carried out. The applied inversion scheme will be presented in chapter 5 using both data space and model space transformation and generalised cross validation (gcv) to choose an automatic regularisation ([Aster et al. \(2005\)](#)). The presented water content in figure 4.10 represents the expectations very well (the complete field case including borehole measurements for verification is discussed in section 7) and fits the data within an error of about 22 nV standard deviation. The calculated standard deviation of the mono-exponential data fit is about 28 nV using error propagation and 17 nV without.

Consequently, both test criteria, the comparability of automatically chosen regularisation and covariance based as well as reliable inversion results based on covariance estimated errors are satisfied.

**Effects of signal sampling rate and low pass filter:** Using the Numis Instrumentation (Iris Instruments [Iris Instruments \(2000\)](#)) the signal sampling frequency is at about 500 Hz. The standard processing and measurement scheme already includes a low pass filter at about 100 Hz ([Legchenko and Valla \(2002\)](#)). If these filtered signals (in contrast to the raw data as used above) are taken into account a significantly underestimated data error is observed. This effect can be explained as follows.

In order to establish a well determined system of equations to solve the mono-exponential fitting problem (for amplitude and decay time) at least two equations, i.e. two measurements, are necessary. Any additional measurements turn the problem into a over determined, i.e. improve the fitting as long as the error is Gaussian distributed. In fact, this is similar to repeating a measurement and calculating the mean

$$\bar{x} = \frac{1}{N} \sum_{i=1}^N x_i. \quad (4.15)$$

Consequently, the more independent measurements are available, the more exact the estimated model parameter become, since the standard deviation of this mean increases according to [Taylor \(1982\)](#)

$$\sigma_{\bar{x}} = \frac{\sigma_x}{\sqrt{N}} \quad (4.16)$$

with square root of the amount of measurements. But this is only valid as long as the measurements are independent experiments.

In fact, applying a 100 Hz low pass filter to the raw signal of 500 Hz without re-sampling the signal does creates dependent measurements. After e.g. [Buttkus \(2000\)](#) filtering at the frequency domain, i.e., multiplication of the signal and the filter function in the frequency domain, is equivalent to the convolution of the signal and the filter function in the time domain. If the low pass filter at the frequency domain is a perfect step function with the corner frequency  $f_g$ ,

$$H(f) = \begin{cases} 1 & \text{for } -f_g \leq f \leq f_g \\ 0 & \text{else} \end{cases} \quad (4.17)$$

then in the time domain it is a sinc function

$$h(t) = 2f_g \frac{\sin(2\pi f_g t)}{2\pi f_g t} \quad (4.18)$$

One can reduce the side lobes using more sophisticated windows. Anyhow, the convolution of the signal with filter in the time domain is an averaging process while the length of averaging depends on the cutoff frequency of the low pass. The lower the corner frequency of this low pass becomes the more averaging takes place and the more dependent data exists. At least one can understand this also using the sampling theorem. There is no larger frequency, i.e., independent information, than half the sampling rate. Consequently, a 100 Hz low pass filtered signal at a sampling frequency of 500 Hz does contain dependent information. Consequently, a low pass filtered signal should be re-sampled. Finally, if now a low pass filtered signal without re-sampling is used to calculate a confidence interval, these intervals must be underestimated and therefore the fitting error is underestimates if the sampling frequency is not adjusted.

On the other hand, according to equation 4.16 assume a signal without any filter (or at least a very wideband detection system) with an increased sampling (e.g. higher sampling rate of the AD converter). With restriction to Gaussian noise, the fitting results can be improved as shown

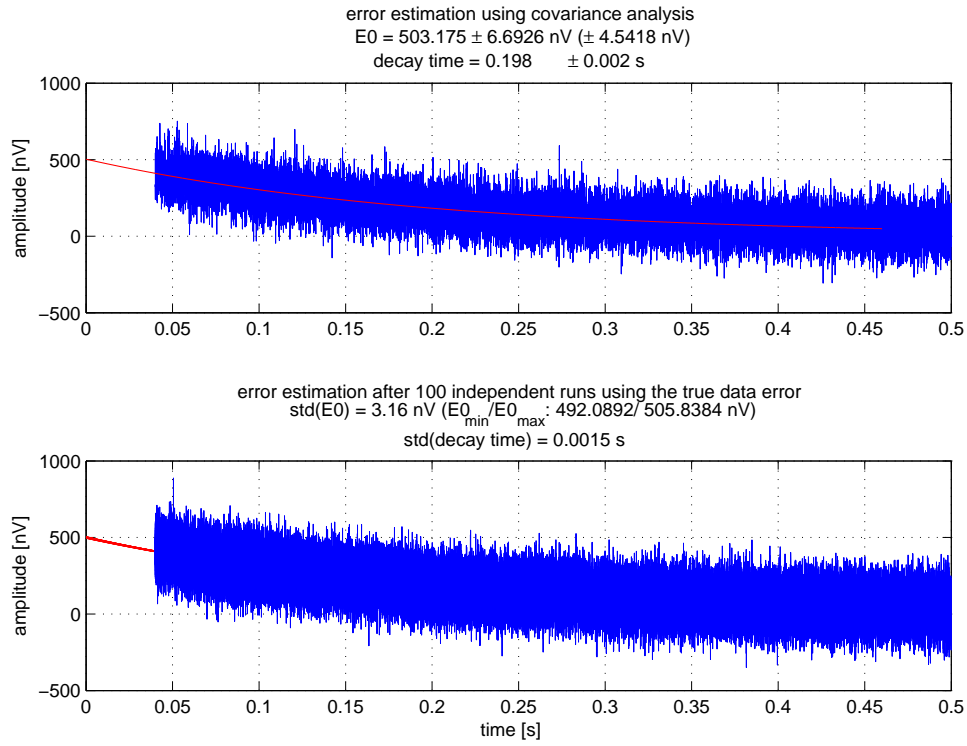


Figure 4.11: Same modelling settings as in figure 4.8 but sampling frequency is increased by a factor of 100 (50 kHz instead of 500 Hz).

in figure 4.11. Of course increasing the sampling frequency might introduce noise sources from higher frequency bands and a low pass filter has to be applied afterwards and reducing the effect of higher sampling.



### 4.3 Dataset processing and error estimations for QT Inversion

**Dataset phase elimination:** The main difference between the QT inversion and the initial value inversion is the use of the complete dataset and not only the initial values. Since a surface NMR dataset is in general complex valued, due to frequency offsets and signal phases, also the initial value is complex valued. It has been shown in subsection 4.2.2 that phase information cannot be used by default. Therefore, only the amplitudes are mostly used. But remark, for fitting the signals the complex time series has to be used (Legchenko and Valla (1998)). Using the amplitudes already for fitting the time series causes systematic error since the exponential function does not decay to zero but to the level of noise. Figure 4.12a/b illustrates the differences in fitting the complex signal in contrast to the amplitudes.

Whereas for the initial value inversion the complex time series is used to derive amplitude and phase initial value and afterwards only amplitudes are used, the QT inversion uses the time series completely for inversion, i.e. the forward response of the QT inversion is the complex time series, i.e. including phases. Thus, the inversion tries to satisfy both amplitude and phase. Consequently, if signal phases are corrupted or unexplainable the inversion becomes instable and leads to wrong solutions. On the other hand, using the amplitude dataset leads to a biased solution.

To avoid both we need an amplitude dataset that decays to zero. The idea is simple. A complex value consists of amplitude and phase or real and imaginary part. If the phase of a complex value is zero then the amplitude equals the real part. So if we delete the phase from a complex signal we can use the real part as amplitudes. If we do not take noise into account the former processing does not show any advantage or disadvantage. But if we take noise into account the new amplitude signal (i.e. the real part) can be negative and decay to zero. Thus, a transformation sets the phase as well as the frequency offset to zero, i.e. the complex signal is reduced to a real valued. Fitting this new signal leads to the correct initial amplitude and decay time. Therefore, this approach ensures the statistical noise properties, especially the mean of zero, to avoid a biased solution.

The transformation is rather simple. According to the Euler formula every complex value  $c$  can be expressed by its amplitude  $|c|$  and phase  $\phi_c$  via  $|c|e^{i\phi_c}$ . Therefore, the single complex signal  $V(t)$  with  $|V(t)|$  its amplitude and  $\phi_{V(t)}$  its phase at the time  $t$ , is initially processed by the standard mono-exponential fitting to derive:  $x_1$  : the initial amplitude,  $x_2$  : decay time,  $x_3$  : phase and  $x_4$  : frequency. At the next step the full dataset is reconstructed according to

$$d(t) = |V(t)|e^{i(\phi_{V(t)} - x_3 - 2\pi \cdot x_4 \cdot t)}. \quad (4.19)$$

while the term “ $\phi_{V(t)} - x_3$ ” subtracts the fitted phase  $x_3$  from the actual signal phase  $\phi_{V(t)}$  and only the random (noise) phase remains. The frequency offset is subtracted via “ $2\pi \cdot x_4 \cdot t$ ” from the signal.

Figure 4.12 illustrates the different fitting strategies. The synthetic signal is calculated with a initial amplitude of  $E_0 = 200$  [nV], decay time  $T_2^* = 0.2$  [s], phase  $\phi = 0.5$  [rad] and frequency offset  $df = 1.5$  [Hz]. First, fitting the complex signal, this synthetic model can be estimated properly. Second, using only the amplitudes of the signal the initial amplitude becomes underestimated and the decay time overestimated. Finally, using the corrected amplitude both amplitude and decay time are again estimated correctly.

The transformation to corrected amplitudes need to fit the complex data first and uses the fitted phase to derive these corrected amplitudes. Consequently, what happens if the fitted phases and frequency offsets are not perfect or wrong? After subsection 4.2.1 there is no correlation between

the amplitudes and decay time on the one hand and phase and frequency offset on the other. That is, even if the phase is incorrectly fitted the amplitudes are not affected as long as the signal shows mono-exponential behaviour, Gaussian distributed noise and/or time constant additional (e.g. instrumental) phases. If the signal shows multi-exponential behaviour the phases cannot be explained completely and some uncorrected artefact remain. To my experience and actual signal to noise ratios the differences between the phase of a multi-exponential signal and a mono-exponential signal is unobservable.

**Dataset error estimations:** Estimating  $\sigma_i$  is not too difficult in contrast to the initial value processing. Here a noise signal, that is recorded before the signal record and stacked in the same manner as the surface NMR signal, can be used to calculate the standard deviation.

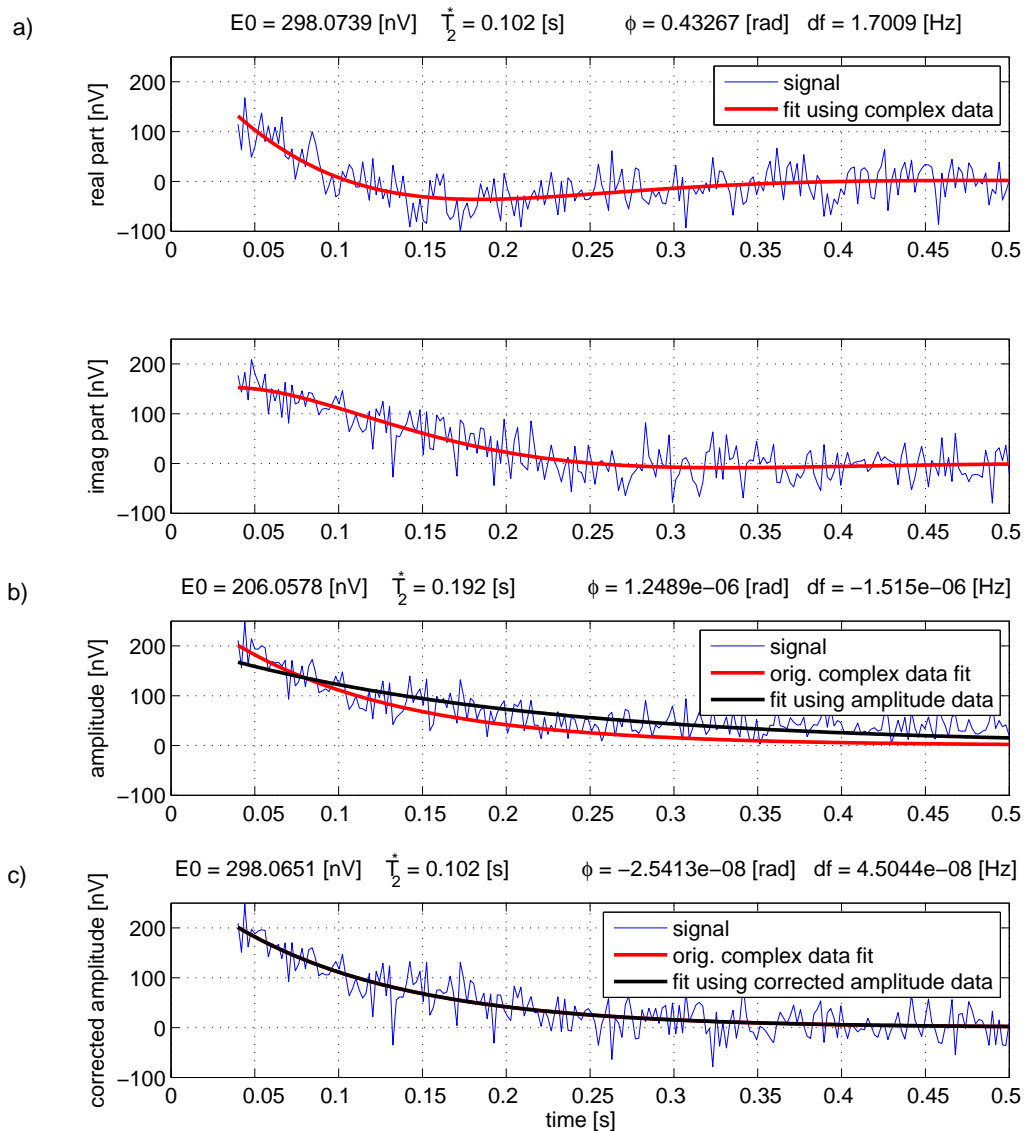


Figure 4.12: Comparison of mono-exponential fits using the complex signal (a), the amplitudes (b) and a corrected, i.e. phase and frequency reduced signal (c).

## 4.4 Estimating systematic error - Frequency variations while stacking

### 4.4.1 Modelling frequency variations while stacking

In general, error estimation is incomplete since (petro) physical theory is not complete and finished. Furthermore, only measurable quantities can be taken into account and possible systematic errors might be hidden.

One of these possible systematic errors can be caused by stacking slightly different signals in respect to the resonance frequency. This stacking of signals can be due to repeated measurements (traditional stacking to enhance the signal quality) but also caused by integrating over some spatial subsurface volume (due to the averaging character of the kernel function). As sources of earth field variation might occur

- daily (sun) and subdaily (moon) variation as linear trends in time and in the range of some 10 nT ([Militzer and Weber \(1985\)](#))
- variations in the range of seconds with amplitudes of 0.01 up to 10 nT due to pulsation/oscillation as random distributed variation in time ([Militzer and Weber \(1985\)](#))
- susceptibility variation within the formation as random distribution in space
- external ferromagnetic sources (dikes, cars) as linear trends in space.

In the following, the range of influence is estimated by synthetic modelling. The impact of the frequency variation on the synthetic model includes:

- actual frequency itself
- additional phase according to [Legchenko \(2004\)](#)

$$\phi = \tan^{-1}(\Delta\omega \cdot \omega_{eff} \cdot \frac{1 - \cos(\omega_{eff}\tau)}{\sin(\omega_{eff}\tau)})$$

$$\omega = \gamma B_T^+$$

$$\Delta\omega : \text{frequency offset}$$

$$\omega_{eff} = \sqrt{\omega^2 + \Delta\omega^2}$$

$$\tau : \text{pulse length}$$
- filter properties of the resonance circuit according to [Strehl \(2006\)](#). The values given below do change slightly according to the field setting but stay constant for this synthetic modelling
 
$$Z(\omega) = \left( \frac{1}{R_C} + i\omega C + \frac{1}{R_L + i\omega L} \right)^{-1}$$

$$R_C : \text{Resistance of the capacitor} = 1e6$$

$$R_L : \text{Resistance of the loop} = .5\Omega$$

$$C : \text{Capacity} = \frac{1}{(2\pi f_r)^2 L}$$

$$f_r : \text{resonance frequency}$$

$$L : \text{inductance of the loop} = 1mH$$

Varying these properties single signals are calculated and stacked to the final signal. Since we expect systematic errors by the frequency variation, the signal is additionally contaminated with Gaussian distributed noise.

#### 4.4.2 Effects of frequency variations on fitting results

Figure 4.13 compares a stacked signal of 100 stacks all of 100 nV noise without frequency variations (all stacks have zero frequency offset) and a contaminated signal of 100 stacks all of 100 nV noise and each a different frequency offset according to a Gaussian distribution of 0.5 Hz standard deviation (the equivalent magnetic field variation is 12 nT). That is, for every single stack a different frequency offset based on the Gaussian distribution of 0.5 Hz standard deviation is randomly chosen and the signal calculated. Finally, all stacks are summed up to the stacked signal and fitted. Obviously, a frequency variation can reduce the decay time of

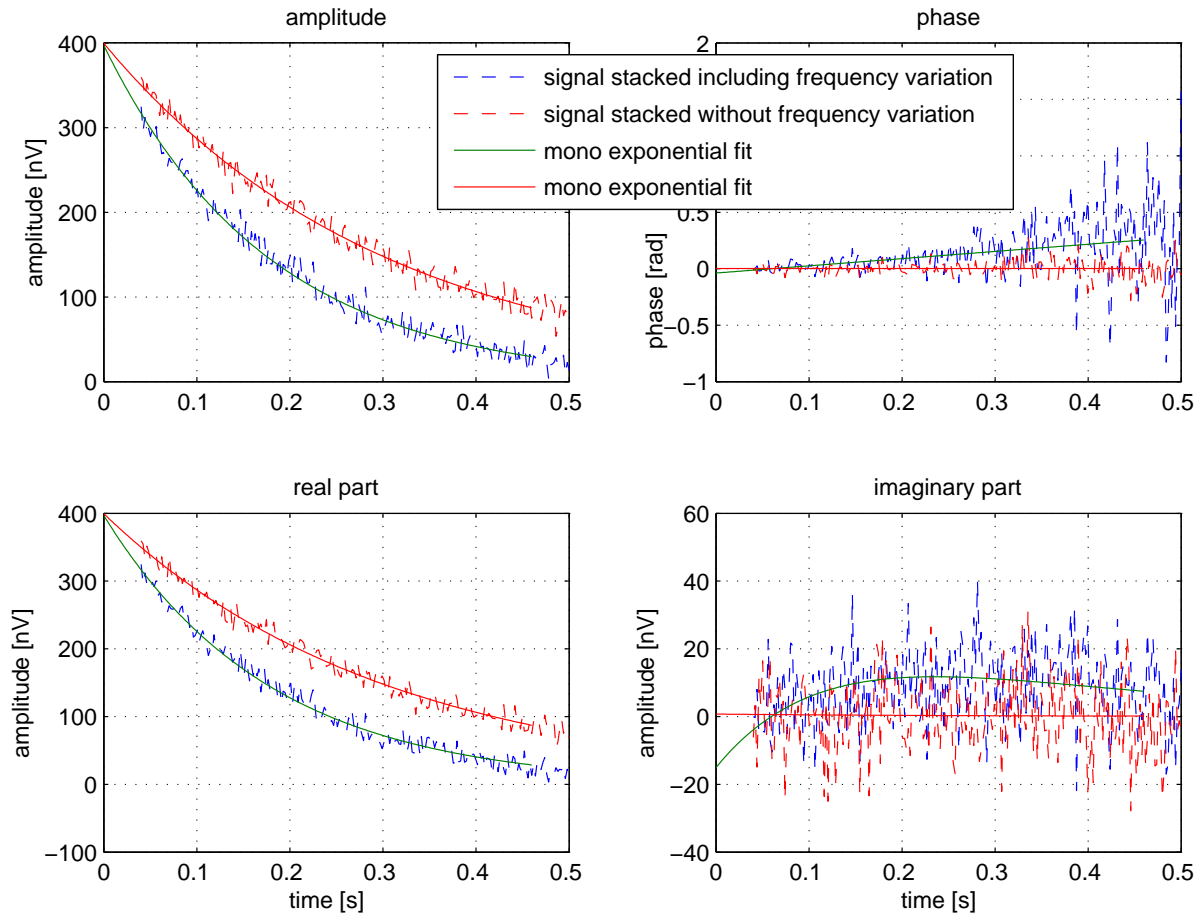


Figure 4.13: Comparison of a stacked signal consisting of 100 stacks all of 100 nV noise without frequency variations (all stacks have zero frequency offset) and its mono-exponential fit to a contaminated signal of 100 stacks all of 100 nV noise and each a different frequency offset according to a Gaussian distribution of 0.5 Hz standard deviation.

the stacked signal significantly from 0.3 s decay time of the true signal down to about 0.2 s for the contaminated signal. In contrast, the amplitude and phase remain less affected.

In order to estimate the range of deviation a set of modelling was conducted and presented in figure 4.14. Three parameters are systematically changed and its influence on the fitting result is observed. The noise level has changed from noise free up to 100 nV for each stack. The standard deviation for the randomly chosen frequency offset is varied from no frequency variation up to 1 Hz and shown at the right column. Furthermore, a linear trend for the frequency offset is

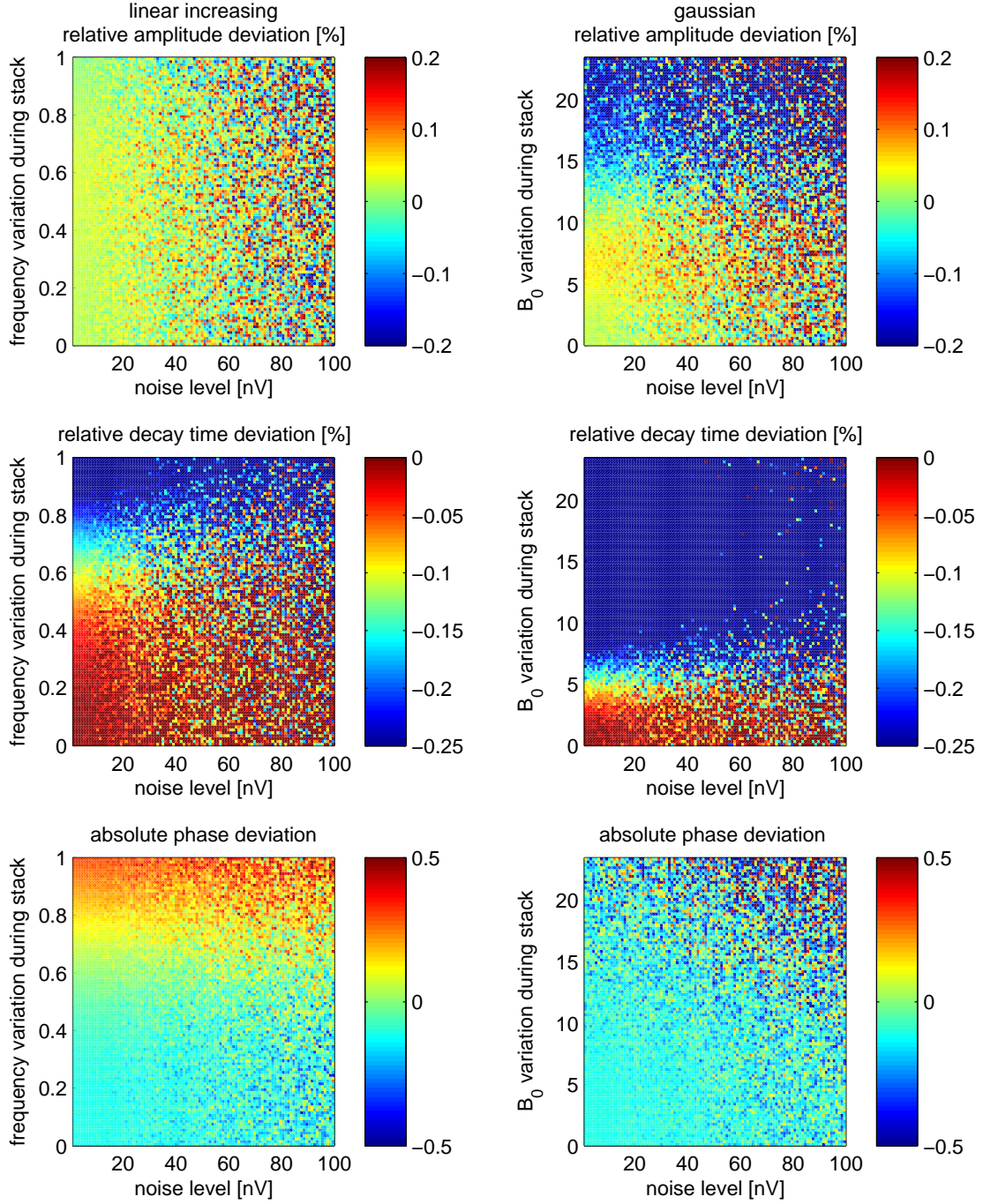


Figure 4.14: Overview on the range of systematic deviations for fitting parameters as functions of the range and type of frequency variations. Linear increasing (left column) is defined from zero to the value given with the y-axis. Gaussian distributed frequency variation (right column) is defined by Gaussian distributed random values of frequency variation with a standard deviation given with the y-axis. For the sake of clarity, the y-axes of the left and right column are equal but given in frequency variation (left) and magnetic field variation (right), respectively.



taken into account and shown at the left column. The linear trend is defined by the first stack with no frequency offset and linear increasing up to a maximum offset for the last stack. This maximum offset was changed from zero up to 1 Hz. For every modelling the number of stacks is fixed at 100. Finally, the calculated stacked signal are fitted and the deviation to the original fitting results are plotted in figure 4.14 against the noise level, Gaussian distributed frequency offset and linear increasing frequency offset, respectively.

As expected for zero frequency variations and noise free condition the fitting results equal the original values. With increasing noise conditions and zero frequency variations, single variations become larger but do not show a systematic trend. On the other hand, with increasing frequency variation systematic effects occur. These effects can be summarised to

1. linear trends need more than 0.5 Hz variation (12 nT) for significant systematic changes in decay time and phase while the amplitude is quite unaffected by linear variations. With increasing noise level all parameters show increasing Gaussian distributed errors as expected.
2. random variation of less than 0.25 Hz variation (6 nT) already causes a decreased decay time of 10%, the signal amplitude is less affected until 0.5 Hz, the signal phase in contrast stays unchanged from systematic errors, here the random frequency variation act as random error.

### 4.4.3 Detectability of frequency variations

Variations of the earth field amplitude in time can be observed easily with standard magnetometer within a certain time interval of integration, e.g. some milliseconds. This is suitable for long time observation, i.e., diurnal variation, but cannot resolve very short spike like events. An appropriate scheme to detect contaminated signals without a magnetometer using only the dataset itself is based on a sub-dataset analysis.

A dataset is separated into several sub-datasets that include a sub-amount of the original stacks. For example, the original dataset contains 100 stacks and the sub-dataset contains 50 stacks. In order to apply a statistical analysis e.g. 20 sub-datasets each of 50 stacks are selected. Each of this sub-dataset has to be different.

These sub-datasets are processed and fitted in the usual scheme for initial amplitude, decay time, phase and frequency offset. Since several sub-datasets exist the fitting results can be used for statistical analysis. That is, the 20 different fitting results have a mean and a standard deviation for amplitude, phase, decay time and frequency offset, respectively.

Figure 4.15 shows that these statistical properties, i.e., the standard deviation of the fitting parameters, is smaller for an uncontaminated dataset compared to a dataset affected by frequency variations. Consequently, a field dataset has to be separated into several sub-datasets and compared to a synthetic dataset at equivalent noise contamination. The level of noise contamination can be derived from the field noise record. If the calculated statistical properties of the field dataset and the synthetic dataset are equal, then the field dataset does not contain frequency variations while stacking. Otherwise if the statistical properties, e.g. the standard deviation of the amplitude fit, are higher for the field dataset, frequency variation can be expected.

Even if actually no dataset shows detectable deviation, the effect should not be neglected. A latest development in instrumentation also includes changes of the measurement scheme. Here, all pulse moments are measured one after one, and then the sequence of pulse moments is repeated. This concept increases significantly the time for a single stack and is therefore more sensitive to frequency variation. In contrast, variation of the earth field amplitude in space

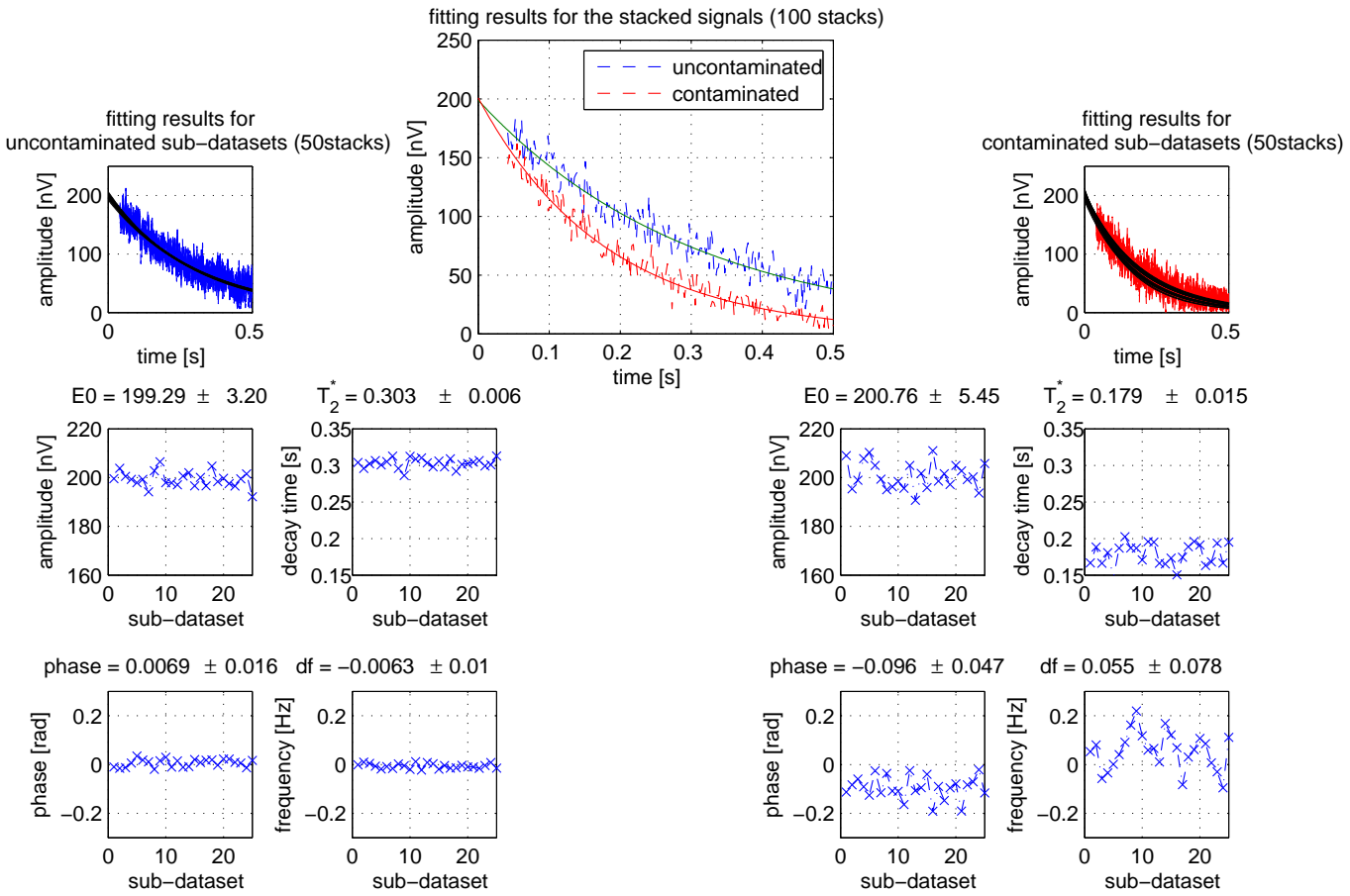


Figure 4.15: Comparison of a contaminated, i.e., a dataset including frequency variations, and a uncontaminated dataset on the base of sub-datasets. Sub-datasets containing 50 stacks are randomly selected from the original 100 stacks. There are no equal sub-datasets. Then each sub-dataset is independently fitted by a mono-exponential. The results of each dataset in respect to initial amplitude, decay time, phase and frequency offset is shown separately. Contaminated sub-datasets show increased standard deviation concerning the fitting result.

is rather difficult to observe from the surface and cannot be detected by the former presented scheme since any time stack is already affected. Two types should be distinct. Effects caused by bodies of larger susceptibility compared to its environment or paramagnetic material as iron. These anomalies can be detected from the surface again by standard magnetometers, i.e. this effects can approximated using figure 4.14. Susceptibility variations at smaller scales, i.e., pore wall, are undetectable from surface measurements but act as random variations. They might be observable using susceptibility logs in boreholes but further research in order to estimate a contamination using only the surface NMR dataset is necessary.

## 4.5 Conclusion and outlook

In this chapter several approaches, both for processing and inversion schemes, have been presented and evaluated concerning its use for the inversion scheme and for estimating the dataset reliability. This evaluation based on both field repeatability, statistical tests and on presenting hidden influences like frequency variations.

To sum the processing steps and main properties

Flow	Comments & Conclusions
Surface NMR dataset $d(q, t)$	Measured voltage in dependency of pulse moment $q$ and time $t$ . Usually repeated in order to stack.
Despiking	Based on the stacking, calculation of statistical properties at every $d(q_i, t_n)$ and delete those $d(q_i, t_n)$ of a single stack that do not fit some statistical expectations, i.e. twice the standard deviation (see 4.1)
Stacking	Check for frequency variations while stacking (see 4.4). Frequency variation of more than 0.5 Hz during stacking, corrupts the estimated decay time.
Exponential Fitting	Preferred mono-exponential fitting due to surface NMR dataset quality (see 4.2.1) based on the complex signal envelope after synchronous detection. Uncertainty calculation has to take Gaussian error propagation (see 4.2.2) and signal sampling vs. filter bandwidth into account. Increasing signal sampling increases the accuracy of parameter estimation Field examples shows (local) repeatable initial amplitudes and decay times
Phase Elimination	Necessary for QT Inversion to avoid biased results (see 4.3)



Since there are even more aspects to be discussed, that are not part of this work but have great influence on the reliability and uncertainty of surface NMR parameters, some open work shall be listed here:

- Relation of parameter estimation in low field compared to high field NMR. [Strehl and Yaramanci \(2008\)](#) compares decay time estimates derived at different primary field situation in order to compare laboratory and field measurements that appear to have different sensitivity.
- Influence of not neglectable short pulses ([Braun et al. \(2003\)](#)) and off resonance excitation on the general spin dynamic ([Walbrecker et al. \(2009\)](#)) is currently under investigation at the research group at the ETH Zurich.

Most of the work focuses on the decay times, that show repeatability in field measurements but the deviation of hydrological parameters cannot be applied by default. Remark, repeatability in this context includes an unchanged loop position. There are data sets measured at locations with comparable hydrological parameters but showing different (repeatable) decay times. Thus, petrophysical research showing sources of influence on the decay time is needed but underway ([Keating and Knight \(2007\)](#), [Bryar and Knight \(2002\)](#)) as well as somehow hidden influences like frequency variation (in time and space) should be of further interest.

In addition, the measured phase contains useful information for both improvements on water content inversion and resistivity inversion but also cannot be applied by default. Here, ongoing research on reliability and repeatability is needed to take advantage of these measured quantities.



## 5 Initial Value Inversion

### 5.1 Singular Value Decomposition (SVD)

A suitable tool to get both an appropriate solution to equation 3.8 and insights into the inverse problem is the well known Singular Value Decomposition (SVD). First, the solution in terms of SVD, including regularisation, is given and general properties are discussed. Second, the resolution in terms of model space and data space is derived.

#### 5.1.1 The inverse problem in terms of SVD

After pre-integration of  $x$  and  $y$  and discretisation of  $z$  the MRS forward problem reads like a standard linear inverse problem (bold capital letter present matrices, bold lower case letters vectors)

$$\mathbf{d}^{\text{obs}} = \mathbf{d} + \mathbf{e} = \mathbf{G}\mathbf{m} + \mathbf{e}. \quad (5.1)$$

with  $\mathbf{d}^{\text{obs}}$  the  $m$ -element noise contaminated complex data vector  $\mathbf{d}$ , i.e., the initial amplitudes of the measured decay curve,  $\mathbf{m}$  the  $n$ -element subsurface water content distribution and  $\mathbf{e}$  some error.  $\mathbf{G}$  is the  $m$  by  $n$  complex MRS kernel function.

Since the subsurface water content  $\mathbf{m}$  is real, the  $m$ -complex values of  $\mathbf{d}^{\text{obs}}$  and  $m$  by  $n$  complex values of  $\mathbf{G}$  can be separated into real and imaginary parts and give  $2 * m$ -independent data.

$$\begin{aligned} \mathbb{R}(\mathbf{d}^{\text{obs}}) &= \mathbb{R}(\mathbf{G}\mathbf{m}) = \mathbb{R}(\mathbf{G})\mathbf{m} \\ \mathbb{I}(\mathbf{d}^{\text{obs}}) &= \mathbb{I}(\mathbf{G}\mathbf{m}) = \mathbb{I}(\mathbf{G})\mathbf{m} \end{aligned} \quad (5.2)$$

In many real cases only the amplitude data contains reliable information. Hence, we have to reformulate the forward problem to use amplitude data

$$\Delta|\mathbf{d}^{\text{obs}}| = \Delta|\mathbf{G}\mathbf{m}| = \mathbf{J}\Delta\mathbf{m} \quad (5.3)$$

while one element of the Jacobian matrix  $\mathbf{J}$  then reads (see subsection 5.4.2 for detailed derivation)

$$\begin{aligned} J(n, m) = & \frac{\mathbb{R}(G(n, m)) \cdot \mathbb{R}(d(m))}{|d(m)|} + \\ & \frac{\mathbb{I}(G(n, m)) \cdot \mathbb{I}(d(m))}{|d(m)|}. \end{aligned} \quad (5.4)$$

Unfortunately, the use of amplitudes turns the problem into nonlinear since the Jacobian matrix as seen in equation 5.3 depends on a certain model. Therefore, the inversion has to be iterative. figure 5.1 shows the dependency of the Jacobian matrix on the used subsurface model to illustrate the non-linearity. First, we calculated a reference Jacobian  $\mathbf{J}_R$  using  $0.05 \text{ m}^3/\text{m}^3$  water content for homogeneous halfspace. Then we build a 3 layer case keeping the background  $0.05 \text{ m}^3/\text{m}^3$  water content but introducing one layer with varied water content, layer thicknesses and/or

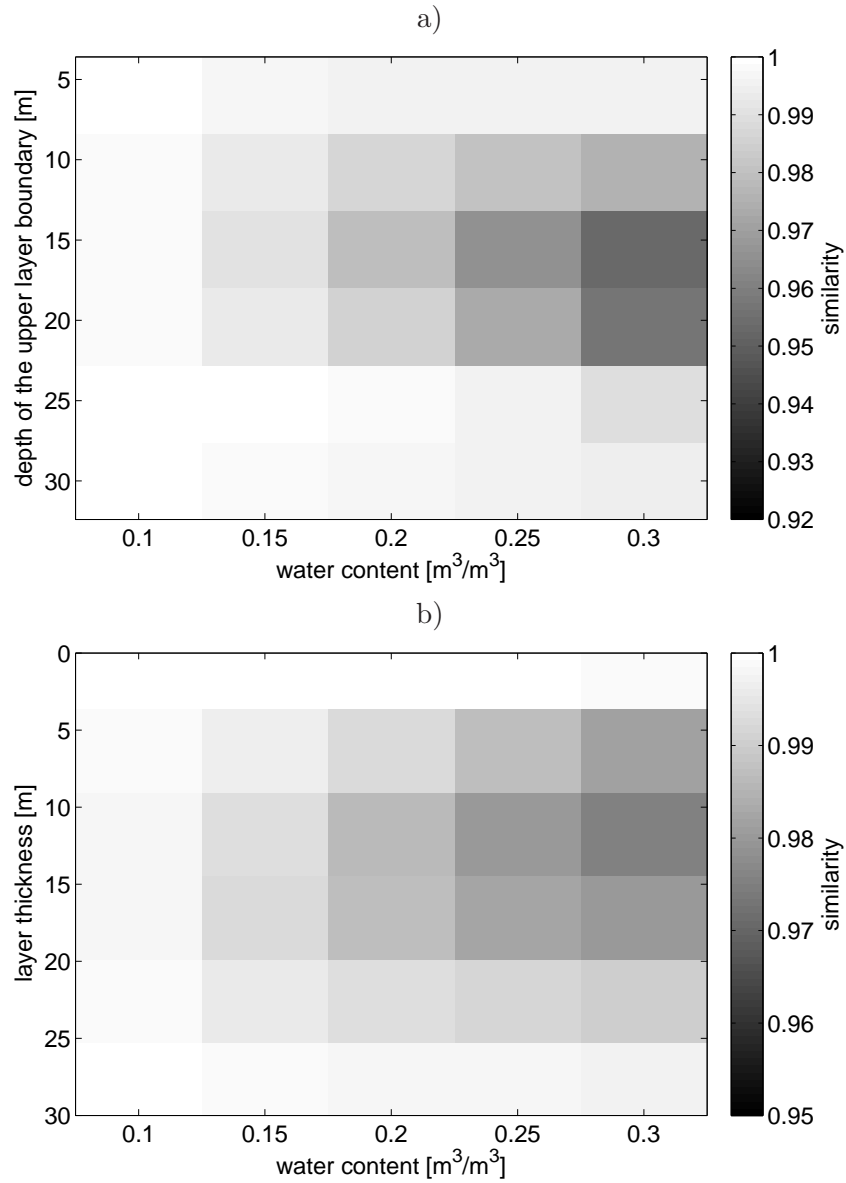


Figure 5.1: Dependency of the Jacobian matrix  $\mathbf{J}$  from the subsurface water content model. Similarity calculated between a reference model of  $0.05 [m^3/m^3]$  background water content and a 3 layer case keeping the background  $0.05 [m^3/m^3]$  water content but introducing one layer with varied water content and a) variation of layer thickness (centered around 15m depth), b) variation of the upper layer boundary depth and 10m constant layer thickness.

layer position to calculate the Jacobian  $\mathbf{J}$  to be compared with the reference. As a measure of similarity between these two Jacobians we use

$$S = \frac{\|\mathbf{J} \times \mathbf{J}_R^T\|}{\|\mathbf{J}\| \cdot \|\mathbf{J}_R\|} \quad (5.5)$$

with  $S \in [0, 1]$  while  $S = 1$  for  $\mathbf{J} = \mathbf{J}_R$ . It shows that for a wide range of parameter variations the similarity of the Jacobians is large, i.e. the dependency of the Jacobian from the actual model is small. Consequently, as a good estimation we can still use linear inversion theory, even if using the amplitudes.

Whether amplitudes or complex data is used and via a Singular Value Decomposition (SVD) the inverse problem (Eq. 5.1) is decomposed into (Menke (1984), Aster et al. (2005)),

$$\mathbf{d}^{\text{obs}} = \mathbf{G}\mathbf{m} + \mathbf{e} = \mathbf{U}_p \mathbf{S}_p \mathbf{V}_p^T \mathbf{m} + \mathbf{e}. \quad (5.6)$$

with  $\mathbf{S}_p$  is a  $p$  by  $p$  diagonal matrix with the ( $p = \min(2 * m, n)$ ) nonzero singular values  $s_i$  in decreasing order.  $\mathbf{U}$  and  $\mathbf{V}$  are orthogonal matrices with unit basis vectors forming the data space  $\mathbb{R}^{2*m}$  and the model space  $\mathbb{R}^n$ , respectively.  $\mathbf{U}_p$  and  $\mathbf{V}_p$  then denote matrices formed by the first  $p$  columns of  $\mathbf{U}$  and  $\mathbf{V}$ .

Calculating the generalized inverse  $\mathbf{G}^\dagger$  yields

$$\mathbf{G}^\dagger \mathbf{d}^{\text{obs}} = \mathbf{G}^\dagger \mathbf{G}\mathbf{m} + \mathbf{G}^\dagger \mathbf{e} = \mathbf{m}^{\text{est}} = \mathbf{V}_p \mathbf{S}_p^{-1} \mathbf{U}_p^T \mathbf{d}^{\text{obs}}. \quad (5.7)$$

Finally, introducing a regularisation the solution to the linear inverse problem reads

$$\mathbf{m}^{\text{est}} = \mathbf{V} \mathbf{F} \mathbf{S}^\dagger \mathbf{U}^T \mathbf{d}^{\text{obs}}, \quad (5.8)$$

with  $\mathbf{S}^\dagger$  the generalized inverse of  $\mathbf{S}$  and  $\mathbf{F}$  the regularisation realised using a diagonal matrix (Hansen (1994)) either as truncation with  $r$  the truncation level

$$f_i = \begin{cases} 1 & \text{if } i \leq r \\ 0 & \text{else} \end{cases} \quad (5.9)$$

or Tikhonov regularisation of first kind with  $\lambda$  the regularisation parameter

$$f_i = \frac{s_i^2}{s_i^2 + \lambda^2}. \quad (5.10)$$

Higher orders of Tikhonov regularisation can be realised using a generalized SVD (GSVD, see Aster et al. (2005)). Besides defining the kind of regularisation a proper choice of the regularisation parameter is essential. There are various methods available. In this thesis the generalised cross validation (gcv) and the discrepancy principle are used. The gcv is used as an automatic regularisation (for details see Aster et al. (2005)) and can be used without any knowledge of data error. In contrast, the discrepancy principle needs an error estimation (also see page 53). Then, the regularisation parameter is chosen to satisfy

$$\frac{\|(\mathbf{d}^{\text{est}} - \mathbf{d}^{\text{obs}})\|_2}{\sqrt{(m-1)}} \leq \delta \quad (5.11)$$

with  $\delta$  the error estimation and  $m$  the number of data.

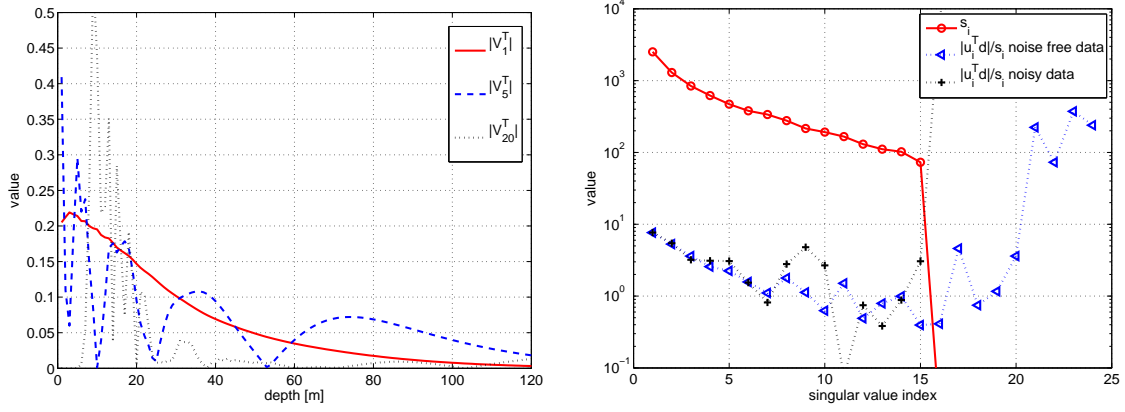


Figure 5.2: a) Unit basis vectors  $\mathbf{v}_i^T$  of the model space and b) Picard plot for kernel function of circular loop with 100 m diameter, 100  $\Omega\text{m}$  halfspace resistivity and 48000 nT magnetic field at  $60^\circ$  inclination

### 5.1.2 Picard Plot and model space basis vectors

Analysing equation 5.7 gives insight into the effects of regularisation and basic understanding of how the estimated model is reconstructed. Starting with figure 5.2 a) the columns  $\mathbf{v}_i^T$  of the model space  $\mathbf{V}$  are shown. The first column  $\mathbf{v}_1^T$  is a smooth distribution. Increasing the index, high frequency variations are introduced. Consequently, a smooth solution can be forced if the amount of model space columns are limited to a certain level  $r$ , i.e., taking for example only the first 10 columns for reconstruction and neglecting all others. This approach is known as truncation and is realised by an appropriate matrix  $\mathbf{F}$ . Actually, the number of columns in practice is already limited, due to the rank of  $\mathbf{G}$ . That is, the maximum reconstruction sharpness is already defined by the calculation of  $\mathbf{G}$ , i.e., the subsurface discretisation and number of measurements.

The truncation level  $r$  is then determined using the Picard Plot (Fig. 5.2b) in order to check the Picard conditions (Fedi et al. (2005)). For the sake of clarity, the Picard Plot is only used to illustrate general properties and not used for inversion in later chapters. The Picard condition states that the range of coefficients  $|\mathbf{u}_i^T \mathbf{d}|$  that decay on average faster than the distribution of  $s_i$  are not controlled by the noise and can be used to calculate a stable inverse  $\mathbf{G}^\dagger$ . Let's set

$$\mathbf{a} = \mathbf{S}^\dagger |\mathbf{U}^T \mathbf{d}^{\text{obs}}| \quad (5.12)$$

or using index notation

$$a(i) = |\mathbf{u}_i^T \mathbf{d}|/s_i \quad (5.13)$$

in equation 5.8 and interpret  $\mathbf{a}$  as weighting coefficients to  $\mathbf{V}$ . Obviously,  $\mathbf{a}$  must not increase with increasing index. Otherwise high frequency variation are uncontrolled and the model overfits the data. Thus, plotting  $|\mathbf{u}_i^T \mathbf{d}|/s_i$ , the usable range of indices is given for on average not increasing values of  $|\mathbf{u}_i^T \mathbf{d}|/s_i$ . The truncation level  $r$  then is the last singular value to be included. Figure 5.2b) shows that the truncation level  $r$  increases from approx.  $r = 12$  for noisy data (300 nV Gaussian distributed noise) to  $r = 18$  for noise free data. The truncation level generally increases with decreasing noise level. Consequently, datasets with unknown noise can be compared in terms of their truncation levels to check the data quality.

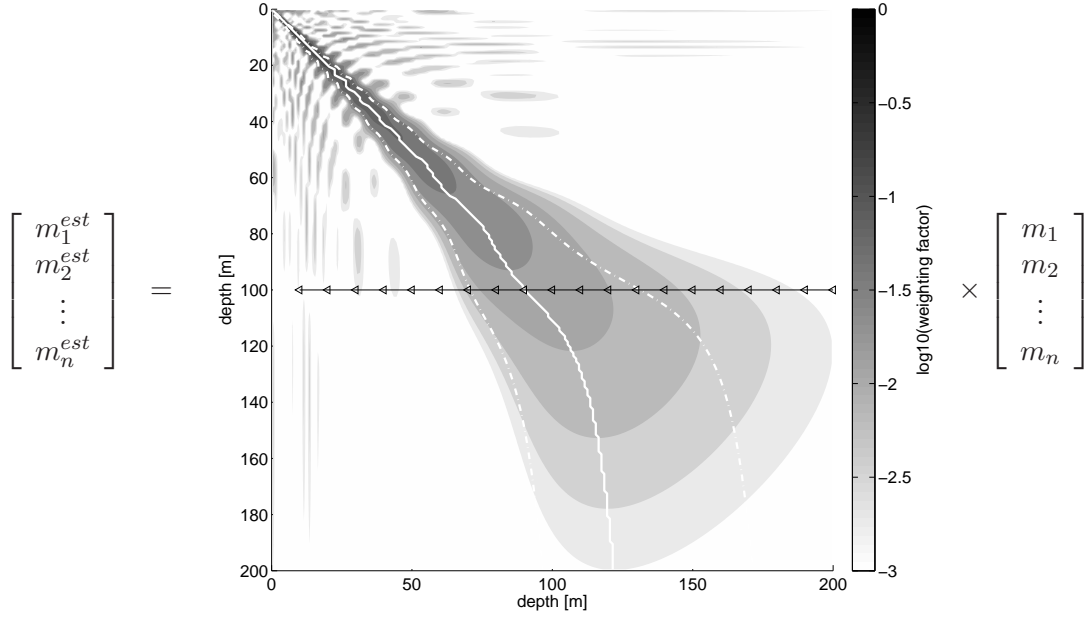


Figure 5.3: Visualisation of the model resolution matrix  $\mathbf{R}_m$  as weighting operator between true subsurface water content and estimated water content. The white dashed lines indicates the full width at the half maximum of a row  $\mathbf{R}_m$ . The white solid line indicates the depth position of this maximum. The black line with triangles shows the depth until the deviation between the position of the maximum and the diagonal is less than 10 %. This depth defines the confidence depth of the MRS water content image.

### 5.1.3 The model resolution matrix in terms of SVD and measures of resolution

After equation 5.7 both the forward and inverse operator define the relationship between the estimated model and the true subsurface.

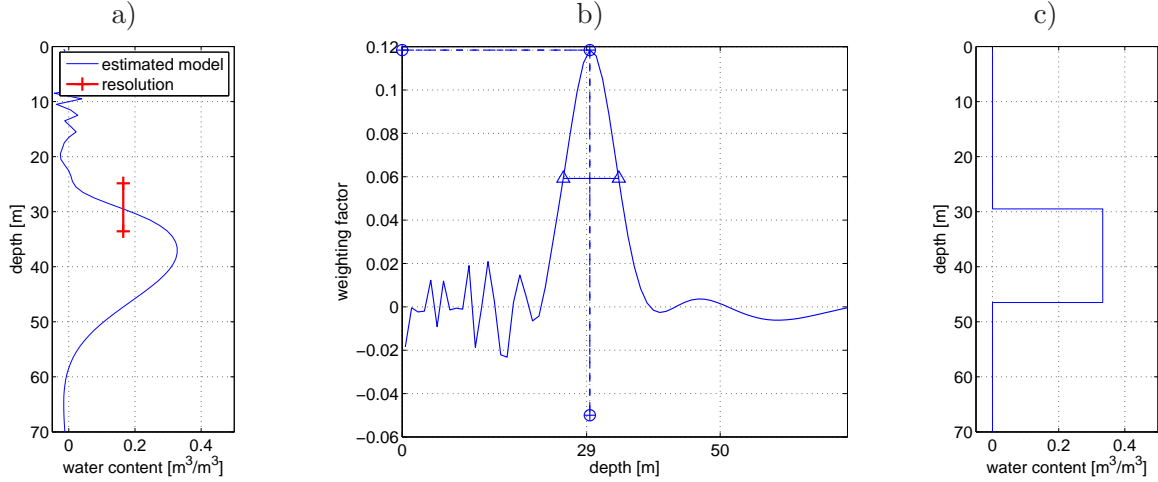
$$\mathbf{m}^{\text{est}} = \mathbf{G}^\dagger \mathbf{G} \mathbf{m} + \mathbf{G}^\dagger \mathbf{e} = \mathbf{R}_m \mathbf{m} + \mathbf{G}^\dagger \mathbf{e}, \quad (5.14)$$

The product  $\mathbf{R}_m = \mathbf{G}^\dagger \mathbf{G}$  is called the model resolution matrix. Since the data error  $\mathbf{e}$  does not vanish for real data, a regularisation has to be applied and  $\mathbf{R}_m$  is not an identity matrix. In terms of SVD the resolution matrix can be calculated after

$$\mathbf{R}_m = \mathbf{V} \mathbf{F} \mathbf{V}^T. \quad (5.15)$$

Figure 5.3 shows the resolution matrix calculated for  $d = 100$  m loop diameter,  $100 \Omega\text{m}$  homogeneous subsurface resistivity, 24 logarithmically spaced pulse moments  $q$  in the interval  $[0.2 \text{ } 18]$  As and  $\lambda = 100$  (see Eq. 5.10). Exemplarily  $m_2^{\text{est}}$  in figure 5.3 is the water content derived from the inversion result at 29 m depth. It is the weighted sum of the true subsurface water content  $\mathbf{m}$  with  $\mathbf{r}_m^i$  the  $i$ 'th row of the resolution matrix  $\mathbf{R}_m$  corresponding to 29 m depth as weighting operator. If  $\mathbf{r}_m^i$  is a "delta like" operator then  $m_2^{\text{est}} = m_2$ . The broader the peak of  $\mathbf{r}_m^i$  becomes, the more  $m_i$  are included into  $m_2^{\text{est}}$ , i.e. the resolution decreases.

Using this relationship some valuable measures can be defined to analyse the inverse problem and evaluate the estimated model.



$$m^{est}(29m) = \sum_{i=1}^{z_{max}} R_m(i, 29m) * m_i^{true}$$

Figure 5.4: Resolution width. The full width at half the maximum of a row of the resolution matrix (b) estimates the averaging depth range of the true model (c) for the estimated model (a) at a certain depth (29 m). The red bar in (a) indicates the full width at half the maximum, i.e., the resolution width.

**Interval of confidence:** The position of the maximum of the row  $\mathbf{r}_m^i$  indicates the focus of this weighting. Thus, misinterpretation occurs if the position of this maximum is not centered at the main diagonal of  $\mathbf{R}_m$  (Friedel (2003)), and the estimated model shows wrong water content according to the position of the maximum. It is observed that from some depth on the deviation between the main diagonal and the position of the rows maximum continuously increase, at least due to the limited penetration depth. Therefore, we define the interval of confidence for deviations between the position of the maximum and the main diagonal of less than 10 %. Additionally, we define the lower boundary of the confidence interval as confidence depth.

**Resolution width:** In order to get a suitable measure for the resolution at a certain depth, the full width at the half maximum of a row  $\mathbf{r}_m^i$  of the model resolution matrix is introduced (Fig. 5.4). This resolution width describes the size of the depth interval constructing the estimated water content as a weighted sum of the true subsurface water content. This replaces the radius of resolution proposed by Friedel (2003) taking only the diagonal values of the resolution matrix into account as a more precise measure of resolution.

**Detection depth:** In Legchenko and Shushakov (1998) the detection depth is equal to the depth where the signal amplitude of a 1 m thick layer with 1 m³/m³ water content can be measured above a noise level of 25 nV (according to the instrumental resolution). Hence, the detection depth defines the deepest water layer that may influence the estimated water content, but a reliable interpretation of signals arising from this depth is possible only with a-priori information (e.g. known boundaries). A comparison of the interval of confidence and detection depth can be found in Müller-Petke and Yaramanci (2008).



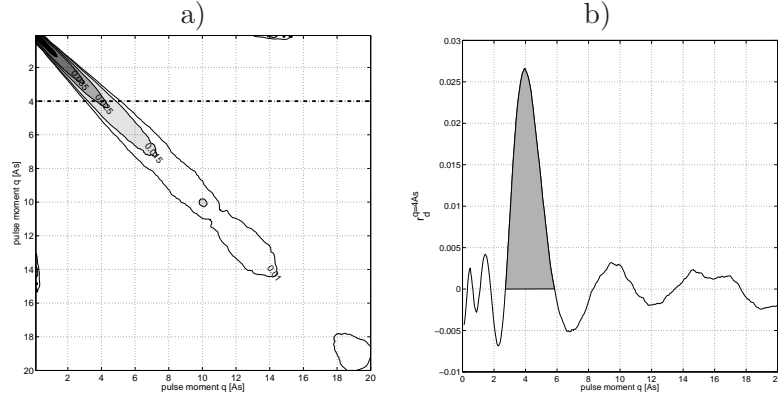


Figure 5.5: a) Data resolution matrix  $\mathbf{R}_d$  based on the Jacobian as in figure 5.2 and calculated with a truncation level of 10. b) Single row of  $\mathbf{R}_d$  for a pulse moment of 4 As. For a completely independent pulse moment this would be a delta distribution. The gray filled area shows dependent pulse moments according to the selected pulse moment of 4 As.

#### 5.1.4 The data resolution matrix in terms of SVD

Similar to equation 5.14 a matrix carrying the transformation of observed and estimated data is derived

$$\begin{aligned} \mathbf{m}^{\text{est}} &= \mathbf{G}^\dagger \mathbf{d}^{\text{obs}} = \mathbf{G}^\dagger \mathbf{d} + \mathbf{G}^\dagger \mathbf{e} \\ \mathbf{d}^{\text{est}} = \mathbf{G} \mathbf{m}^{\text{est}} &= \mathbf{G} \mathbf{G}^\dagger \mathbf{d}^{\text{obs}} = \mathbf{G} \mathbf{G}^\dagger \mathbf{d} + \mathbf{G} \mathbf{G}^\dagger \mathbf{e} \\ \mathbf{d}^{\text{est}} &= \mathbf{R}_d \mathbf{d}^{\text{obs}} = \mathbf{R}_d \mathbf{d} + \mathbf{R}_d \mathbf{e} \end{aligned} \quad (5.16)$$

and in terms of SVD

$$\mathbf{R}_d = \mathbf{U} \mathbf{F} \mathbf{U}^T. \quad (5.17)$$

According to the model resolution the data resolution describes the relationship between observed and estimated data and can be interpreted similar to the model resolution as weighting operator. Obviously, if the data error  $\mathbf{e}$  is not zero but  $\mathbf{R}_d$  an identity matrix the estimated model fits the data error and contains noise features. On the other hand if  $\mathbf{R}_d$  is not an identity matrix not only dependent measurements might occur but also data error is weighted. Therefore the data space trade-off can be defined as data weighting vs. independent measurements. Figure 5.5 shows exemplarily a data resolution matrix and one row at 4 As pulse moment. The estimated datum  $d_i^{\text{est}}$  at 4 As is build by a multiplication of  $\mathbf{R}_d^{q=4As}$  and the observed dataset  $\mathbf{d}^{\text{obs}}$ . The filled peak marks the main influence interval of pulse moments and therefore the dependencies of this pulse moments to all other.

If statistical properties of the data error are known (e.g. standard deviation), a regularisation can be carefully chosen in a way that the deviation of observed data and estimated data represents the data error (Discrepancy Principle, see equation 5.11). Thus, a model is over-regularized if independent measurements are weighted during the inversion. Furthermore, a model is improved if additional dependent measurements are introduced due to its weighting.

Consequently, analysing  $\mathbf{R}_d$  provides insights into measurement dependencies and is used for optimisation strategies in section 5.3. Remark, according to the data space trade-off the primary target of optimisation is not to create a dataset resulting in an identity matrix but to create equally dependent data.

## 5.2 Results of the model resolution analysis

Reliable information or measures to interpret and enhance inversion results are essential for any field applications. These measures can be captured by analysing the inverse problem concerning image reconstruction via analysing its resolution properties as recently successfully applied to several geophysical problems (Friedel (2003), Guenther (2004), Miller and Routh (2007)).

In respect to MRS, two influences can be distinguished: First, the ill-posedness of the inverse problem, i.e., large volumes of proton excitation cause large volumes of averaging. Second, inexact data, i.e., large covariances due to large relative data errors at small signal amplitudes that occur at small pulse moments, i.e., small volumes of proton excitation. The first effect causes poor resolution for large depths but good resolution for small depths while the second effect reduces the resolution for small depths due to the small volumes of proton excitation. Both effects are coupled and must be controlled by a regularisation that depends on the level of data error, i.e., noise conditions. Thus, the resolution matrix is calculated according to equation 5.15 while the elements of the regularisation matrix  $F$  are according to the Tikhonov approach (Eq. 5.10) and chosen in a way to satisfy the discrepancy principle, i.e., the deviation of estimated and observed data represents the data error. Since this approach incorporates an appropriate regularisation as a function of noise conditions and measurement configuration, it leads to resolution parameters and a confidence depth that show the general dependencies of the MRS method in respect to the loop diameter, pulse moment distribution, subsurface resistivity and noise conditions.

Finally, these results are used in analysing a MRS survey and determine optimum survey parameters as well as evaluate its interpretation.

Mark, noise condition always refer to the data error of a single measurements at a single stack while the data error of the sounding curve is derived as described in subsection 4.2.2.

### 5.2.1 Interval of confidence in dependency on loopsize, noise and maximum pulse moment

**Overview:** According to former definition, first the lower boundary of the interval of confidence, i.e., the confidence depth is calculated for a set of kernel functions in order to give an overview on the depth range for surface NMR applications. Table 5.1 lists the confidence depth for loop diameter from 20 m - 300 m and halfspace resistivities from 1  $\Omega\text{m}$  - 1000  $\Omega\text{m}$ . Due to the nature of ill-posed problems dealing with inexact data the level of data error influences the confidence depth as it will be shown later (Fig. 5.6). Therefore, the same level of noise according to the face of the loop based on 50 nV for the  $d = 100$  m loop was used. This is true, if the noise is homogeneous. In fact, mostly the noise is not homogeneous but in order to compare general properties this assumption appears to be useful. Furthermore, the minimum pulse moment is set to 0.01 As and maximum pulse moment to 18 As distributed over 24 pulse moments in total. The results (Tab. 5.1) are comparable to those published in Müller-Petke et al. (2006) using the real part of the kernel function without adding any noise. The increasing influence of electromagnetic attenuation is obvious (also shown in Braun and Yaramanci (2008)) for increased loop diameter. Furthermore, a general depth limitation of the technique down to 100 m can be derived due to geological relevant resistivities .

**Noise influence:** As a prominent and often used configuration the  $d = 100$  m diameter (88 m side length for a equivalent square) placed on a homogeneous halfspace of 100  $\Omega\text{m}$  is chosen to investigate the noise influence on the confidence interval. First (Fig. 5.6 a), the Picard

resistivity [ $\Omega m$ ]		1	3	10	30	100	300	1000
loop diameter [m]	noise level [nV]							
20	2	20	20	20	20	20	20	20
60	18	20	40	55	60	60	60	60
100	50	20	50	70	80	80	80	80
200	200	20	50	70	100	110	120	120
300	450	20	50	70	110	130	130	130

Table 5.1: Confidence depth for different loop diameter and halfspace resistivities. The noise level is based on a 100 m circular loop at 50 nV noise and adopted according the loops face for all other loop sizes in order to ensure comparable results.

plot is used to illustrate the noise influences on the inversion. With increasing data error less singular values, i.e., less model space eigenvectors that improve both near surface resolution and confidence depth (Fig. 5.6 a) are included (in the sense of a truncation SVD approach). For the chosen example at 300 nV  $|u_i^T d|/s_i$  increases (globally) until approximately 10, i.e., in equation 5.9  $r=10$  while for 10 nV  $r=15$  can be used. Figure 5.6b shows the development of the confidence depth with increasing noise conditions. As expected the confidence depth decreases with increasing noise level. On the other hand it increases to a certain plateau with decreasing noise. The top of this plateau is defined by the maximum and total amount of pulse moments available.

**Maximum pulse moment:** Consequently, the influence of the maximum pulse moment is assessed taking the same configuration at 50 nV but variable maximum pulse moment. First, the Picard plot is used to illustrate the influences on the inversion (Fig. 5.7a). In contrast to figure 5.6a, the singular value distribution is not constant, i.e., new information is added to the inverse problem with increasing maximum pulse moment. Hence, the truncation level increases. Figure 5.7b shows the development of the confidence depth with increasing maximum pulse

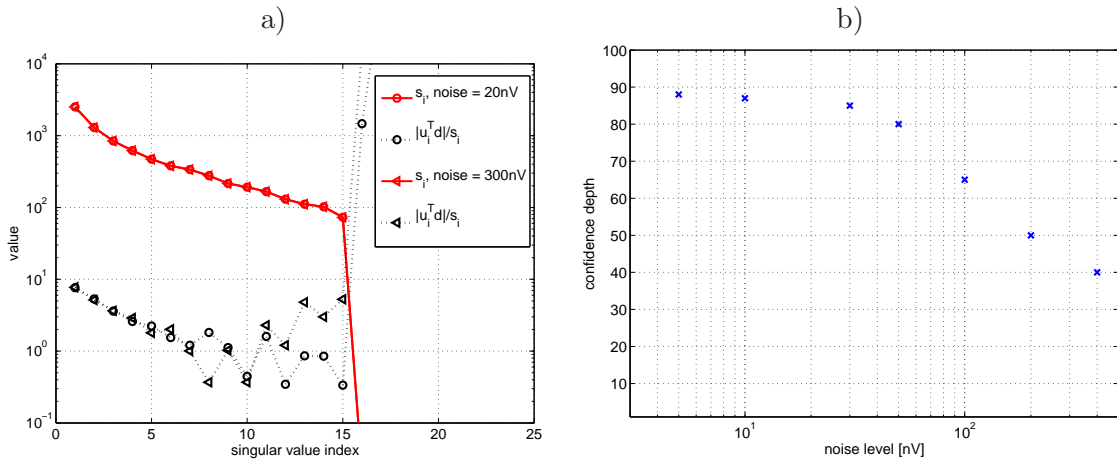


Figure 5.6: Decreasing confidence depth with increasing noise level for  $d = 100$  m loop diameter,  $100 \Omega m$  halfspace resistivity and 18 As max. pulse moment. a) Picard plot, b) confidence depth.

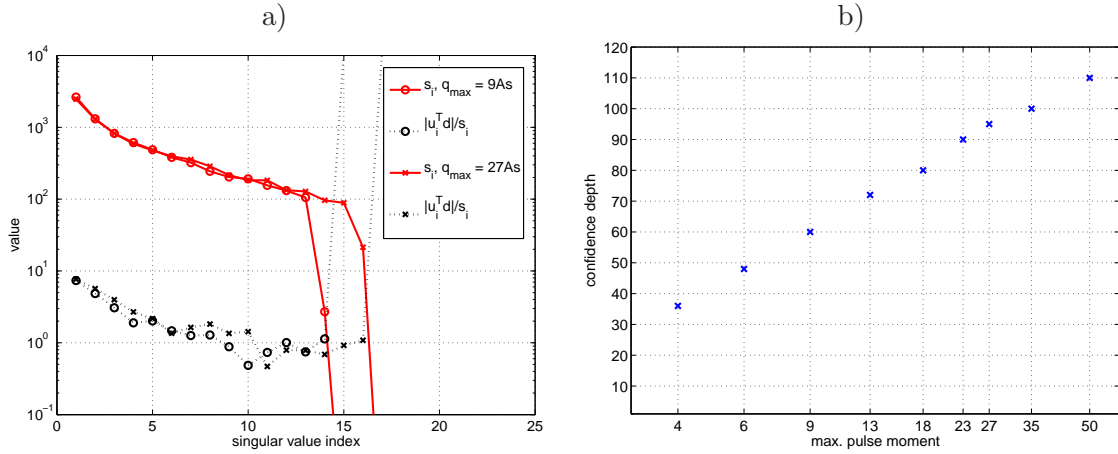


Figure 5.7: Increasing confidence depth with increasing maximum pulse moment for the same configuration as in figure 5.6 at 50 nV noise

moment. Obviously, a linear relationship (at the logarithmic scale of max. pulse moment) exist, i.e., increasing the pulse moment is useful only up to a certain moment related to the loop size and resistivity distribution.

### 5.2.2 Resolution width in dependency on loopsize

Besides the knowledge on dependencies of maximum investigation depth the resolution properties in general and especially the near surface resolution is of interest. One of the basic questions belongs to the relationship of loop diameter and near surface resolution. A simple synthetic model of an aquifer with lower boundary at 2 m as halfspace is useful to illustrate both the use of calculating the resolution width and a proper chosen loop layout. The modelling was carried out taking a  $d = 100$  m,  $d = 30$  m and  $d = 10$  m loop diameter while in order to get a reasonable face the 10 m loop uses 9 turns and equals the face of the 30 m loop. All loops are place on 100  $\Omega\text{m}$  halfspace. The maximum pulse moments where adopted to cover approximately the same depth range using 24 pulse moments in total. The data is contaminated with noise related to the face (based on 20 nV for the 30 m loop). The sounding curve derived by a mono-exponential fit.

The results are shown in figure 5.8. The largest loop provides the best signal to noise ratio that is due to the largest integration volume even in z direction as illustrated by the kernel function. The calculated resolution width at 2 m depth is approximately 7 m, i.e., the sharp boundary of the aquifer is smoothed by averaging over the depth from 0-7 m. The smallest loop of 10 m shows the best resolution of approx. 3 m. The inversion of the 30 m loop data averages the boundary over approx. 4 m. Taking into account that 9 turns of 10 m diameter needs 283 m cable in contrast to 94 m cable used for the 30 m loop, the fields choice is obvious.

### 5.2.3 Field case: Haldensleben

Finally, measurements were carried out at a test site near Haldensleben (previously described in Yaramanci et al. (1999)) to confirm the described analyses, to illustrate its field use and to evaluate the estimated model and field layout.

Remark, that the soundings presented here are measured at a different borehole (B13, see

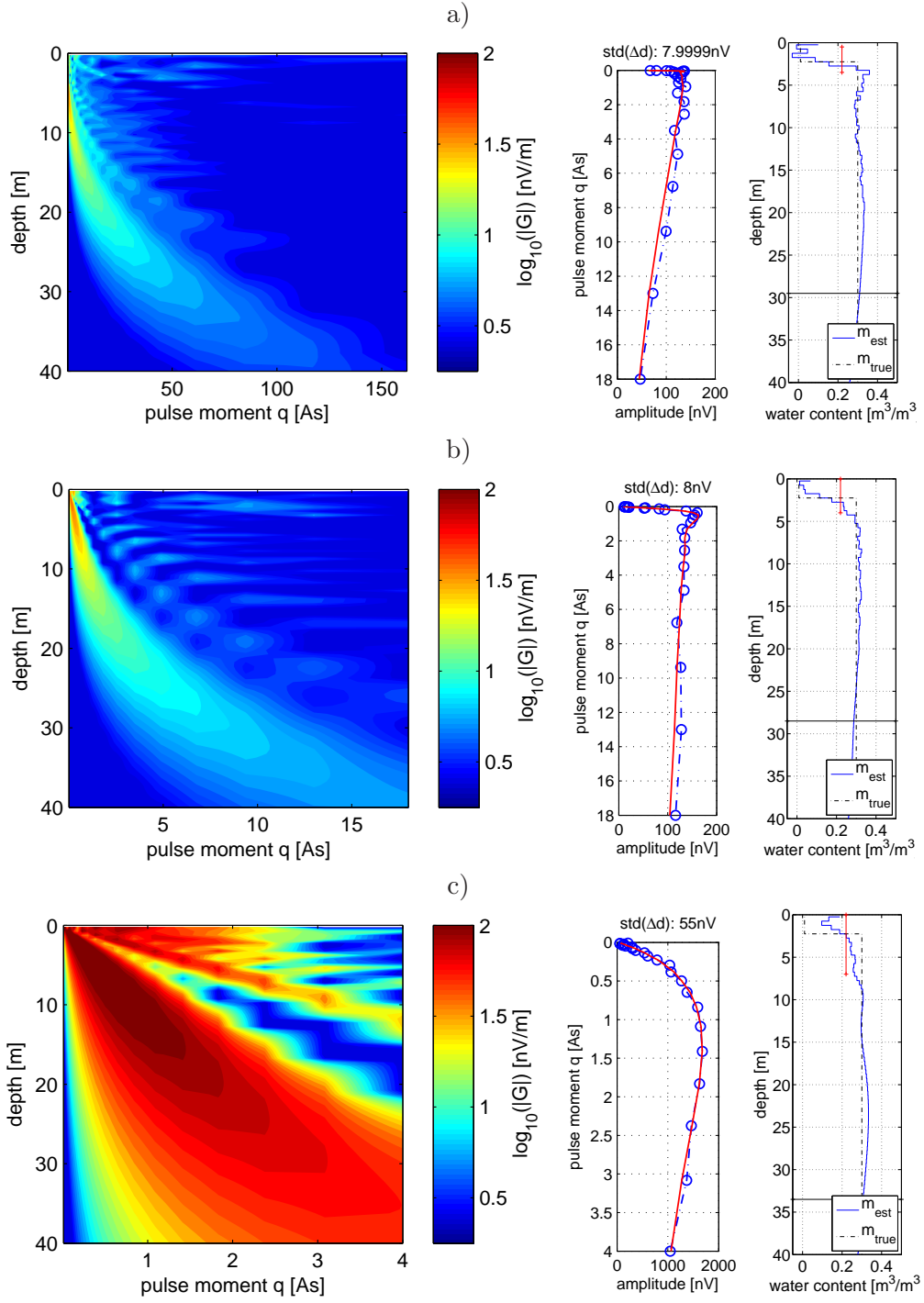


Figure 5.8: Near surface resolution vs. loop size. Left: Amplitudes of the kernel function for a)  $d = 10$  m loop diameter, 9 turns b)  $d = 30$  m, 1 turn and c)  $d = 100$  m, 1 turn. Middle: observed (blue circles) and estimated (red line) amplitude sounding curve, Right: Estimated water content (blue), true model (black dashed), resolution width (red) and confidence depth (black). The noise level is equal according to the loops face, i.e., 20 nV for 10 m and 30 m, 222 nV for 100 m loop.

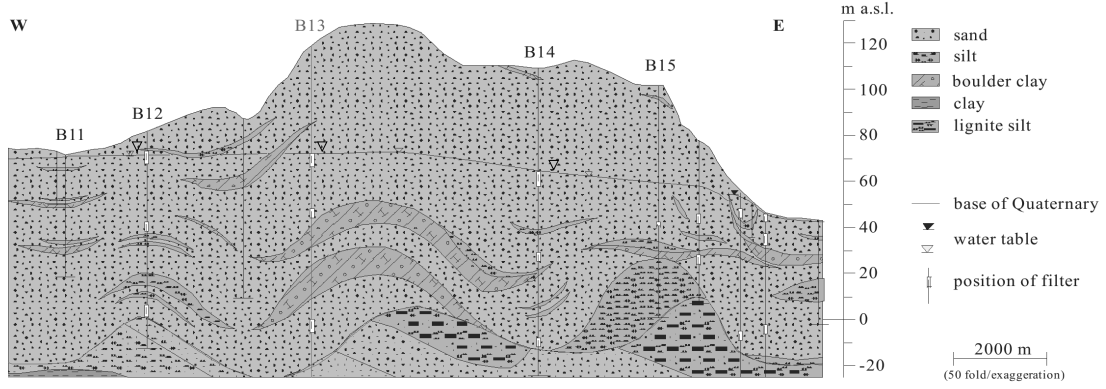


Figure 5.9: Hydrogeological section of the test site near Haldensleben (Germany) by courtesy of German Geological Survey (BGR)

hydrogeological section in figure 5.9). B13 is approximately 30 m elevated and 8 km north of the borehole B8 presented in Yaramanci et al. (1999). A set of borehole measurements (resistivity, gamma-ray) were conducted. At B8, additionally impulse-neutron-gamma measurements were carried out to estimate the subsurface water content distribution. Since the geology is not significantly different, the borehole measurements of B13 and B8 can be compared and define the aquifer top at 48 m depth with a thickness of 30 m. This aquifer is underlain by two deeper aquifers that are separated from the first by marl aquicludes.

As shown in table 5.1 enlarging the loop size increases the penetration depth for a fixed maximum pulse. In contrast, the maximum voltage  $U_{max}$  of the NUMIS device is limited to 4000 V (Iris Instruments (2000)) and hence the maximum pulse moment (calculating the loop impedance  $L$  after Gover (1946))

$$q_{max} = \tau I_{max} = \tau \frac{U_{max}}{\sqrt{R_{\Omega}^2 + \omega^2 L^2}} \quad (5.18)$$

depends on the loop diameter (assuming isolating ground conditions). For example enlarging the loop reduces the maximum pulse moment  $q_{max} = 18$  As for a  $d = 96$  m loop to  $q_{max} = 11$  As for  $d = 144$  m diameter. Since a deep aquifer at 48m is expected two configurations, a  $d = 96$  m and  $d = 144$  m were carried out. The results are shown in figure 5.10. Due to the reduced maximum pulse moment, the larger loop of 144 m diameter shows a slightly lower confidence depth and decreased resolution compared to the smaller loop. We assess the estimated water content with the model derived from borehole measurements. The second and third layer cannot be estimated as expected from the confidence depths. The boundaries of the first layer are smoothed and the larger loop of 144 m diameter shows a higher degree of smoothness. These results are in good agreement with the presented resolution measures. Due to the resolution the boundaries are smoothed and using the large loop the water content is even at its maximum underestimated since the resolution width is larger than the thickness of the aquifer. Taking the higher effort and necessary cable length of building larger loops in the field into account, the use of a pre-analysis becomes obvious. Therefore, selecting the loop size carefully the estimated water content model can be improved and field effort can be reduced.

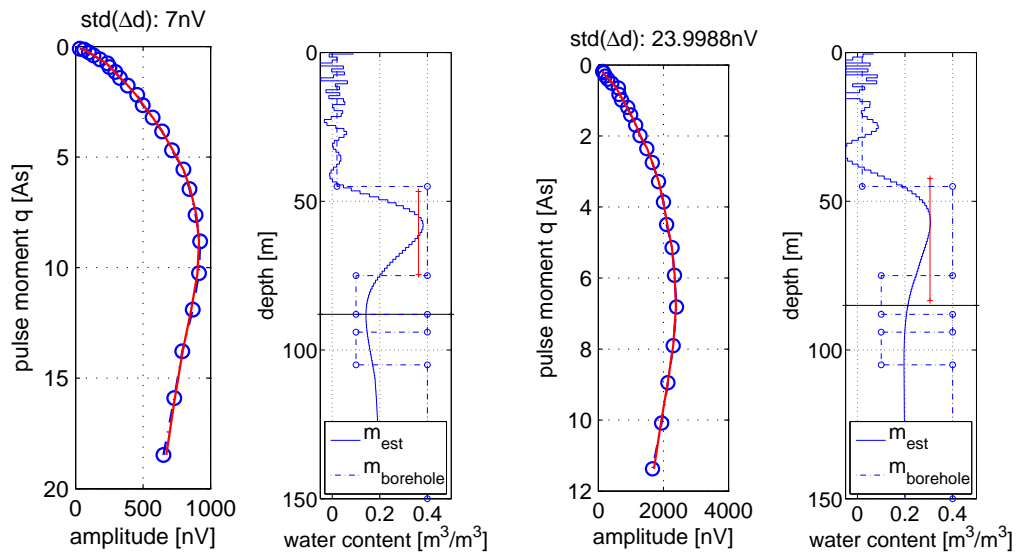


Figure 5.10: Inversion results at the test site Haldensleben of measurements with two different loop sizes. left)  $d = 48$  m loop diameter right)  $d = 72$  m. The dashed line represents a water content model derived from borehole measurements.



### 5.3 Results of the data resolution analysis

Most geophysical measurements provide data that are integral values. The area of integration depends on the methods characteristics, e.g. DC depth sounding, and user defined values like the electrode spacing. The area of integration is changed by changing e.g. the electrode spacing. A set of measurements with different data arising from different integration areas can be called dataset or sounding curve (1D case). Depending on the distribution of electrode spacing the integral values might contain common areas that are nearly equal, i.e., the measurements are fairly equal, or do not share any common values or finally, share only some integration area. Taking into account that a measurement is never exact the first case does not provide a new measurement. The second case provides independent information of another area. But the third case can be used to decrease the integral value to a smaller area and is mostly referred to be a tomography.

Consequently, a dataset that contains measurements that are distributed in a way to provide a maximum of overlapping areas but avoids equal measurements is called optimal and includes a maximum of subsurface information. By a constant number of measurements these datasets are able to image the closest truth to reality compared to other distributions with the same number of measurements.

With regard to surface NMR the choice of pulse moments influences the quality of the estimated model and is to be optimised.

So far, the optimal distribution is calculated by analysing resolution measures derived from the model resolution matrix, i.e., to change a dataset iteratively until consideration concerning the model resolution matrix are met. This task is often referred to as experimental design or optimal survey design and has been recently applied to electrical resistivity tomography (Stummer et al. (2004), Dahlin and Zhou (2004), Wilkinson et al. (2006)) or seismic tomography (Curtis (1999), Curtis et al. (2004)). Legchenko and Shushakov (1998) has proposed an approach for magnetic resonance sounding (MRS) based on the kernel function.

Here, a direct approach is presented to estimate the optimal measurement distribution based on analysing the data resolution matrix. The developed scheme is used to calculate an optimal MRS sounding sequence.

Besides optimal distribution, the number of measurements is an essential parameter for an efficient determination of subsurface properties. The number of measurements may be fixed (Stummer et al. (2004), Wilkinson et al. (2006)) or determined by cost thresholds (Curtis et al. (2004)). In contrast, a measure based on the covariance matrix is presented in this section. This measure is used to evaluate the efficiency of a pulse moment distribution in dependency of the information content versus the number of measurements.

Depending on the noise conditions MRS field surveys may take several hours up to a day for one single sounding (using 16 pulse moments as a standard number of measurements). Obviously, there is an outstanding need for efficiency to avoid redundant measurements.

In dependency of loop size, subsurface resistivity, maximum pulse moment and noise conditions a sequence of optimal distributed measurements is presented and the number of efficient measurements for common used parameter settings is listed.

#### 5.3.1 Calculation of optimal pulse moment distributions

According of equation 5.17  $\mathbf{R}_d$  can be calculated using the unit basis vectors forming the data space and the regularisation by simple matrix multiplication. The singular value decomposition has to be done only once to create the unit basis vectors. While the optimal distribution is



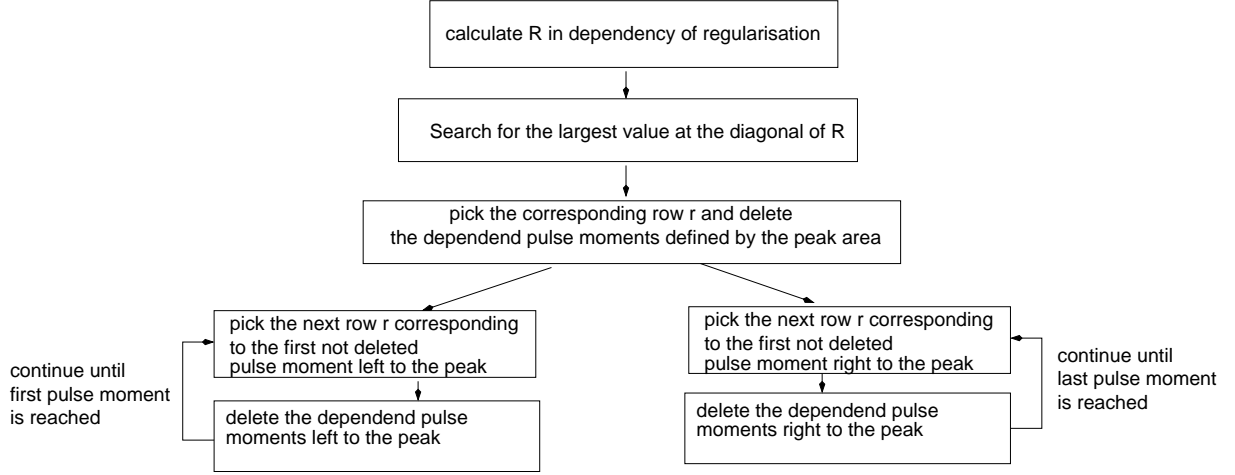


Figure 5.11: Scheme to calculate optimal distributed pulse moments.

defined by the methods physics, the number of measurements depends on the level of data error. First, a scheme to calculate this optimal distribution of pulse moments for predefined number of measurements is provided. Therefore, the truncation approach is used as regularisation. Here the number of used basis vectors exactly defines the number of independent measurements. Figure 5.11 shows the scheme to calculate an optimal distributed set of pulse moments in dependency of the chosen number of measurement realised by a truncation. The scheme is based on deleting dependent measurements by analysing the rows of  $\mathbf{R}_d$ . Since it might not be excluded to have a “most valuable” measurement, the starting point is not the smallest pulse moment but defined by the largest value of  $\mathbf{R}_d$ . Using MRS as an example this “most valuable” measurement within a dataset is obviously neither the first nor the last, but the pulse moment with the highest expectable signal amplitude. Figure 5.12 shows optimal distributed pulse moments for different loop sizes and resistivities. Besides calculating an optimal distribution for any sounding using the appropriate parameters for sensitivity calculation (loop size, resistivity) a cubic function was found to be a usefull fit for a wide range of distributions. The cubic parameters are:

$$q(x) = [(q_{max} - q_{min}) * (0.9 * x^3 - 0.1 * x^2 + 0.2 * x)] + q_{min} \quad (5.19)$$

while  $x$  is a vector  $\in [0, 1]$  with  $n$  equally spaced elements,  $n$  the number of pulse moments and  $q_{min}, q_{max}$  are the minimum and maximum pulse moment, respectively. As long as resistivity can be neglected (that is in dependency on the loop size Müller-Petke et al. (2006) and Braun and Yaramanci (2008)) the optimal distribution of pulse moments does not change significantly and can be approximated by the cubic fit. With increasing resistivity influence the distribution changes but the cubic is a usable approximation for resistivities in the range of geological relevance.

### 5.3.2 Evaluation of optimal pulse moment distributions

In order to evaluate the maximised subsurface information provided by datasets with optimal pulse moment distributions compared to all other, datasets of optimal, logarithmic and linear distributed pulse moments using a 96 m diameter circular loop, 100  $\Omega m$  homogeneous halfspace

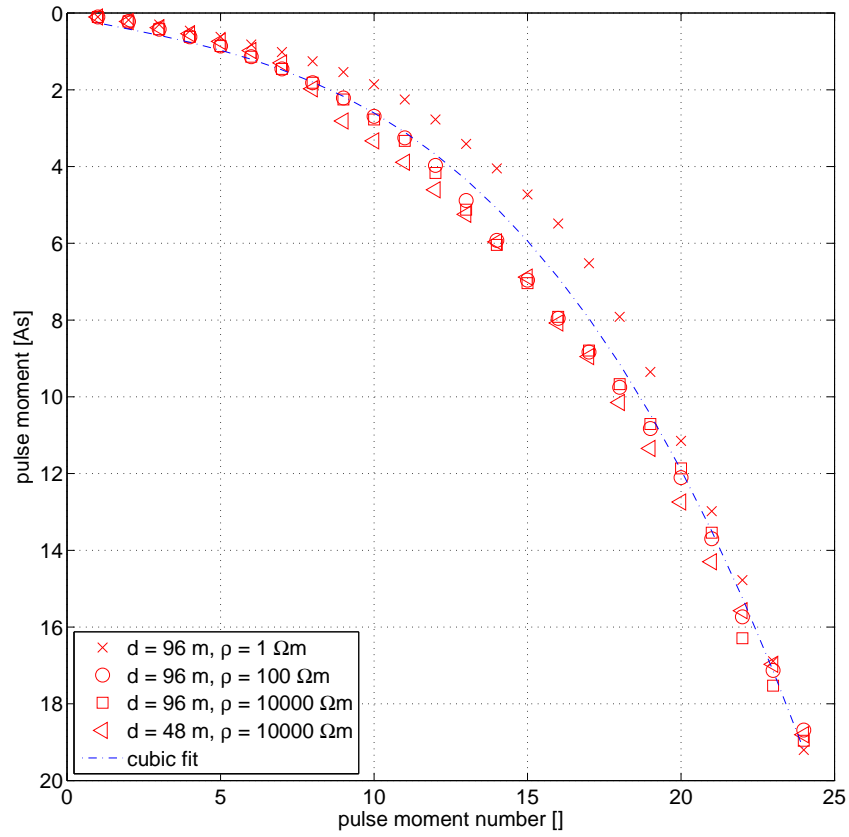


Figure 5.12: Optimal distributions of pulse moments for different loop sizes and resistivity distributions with a fixed total number of 24.

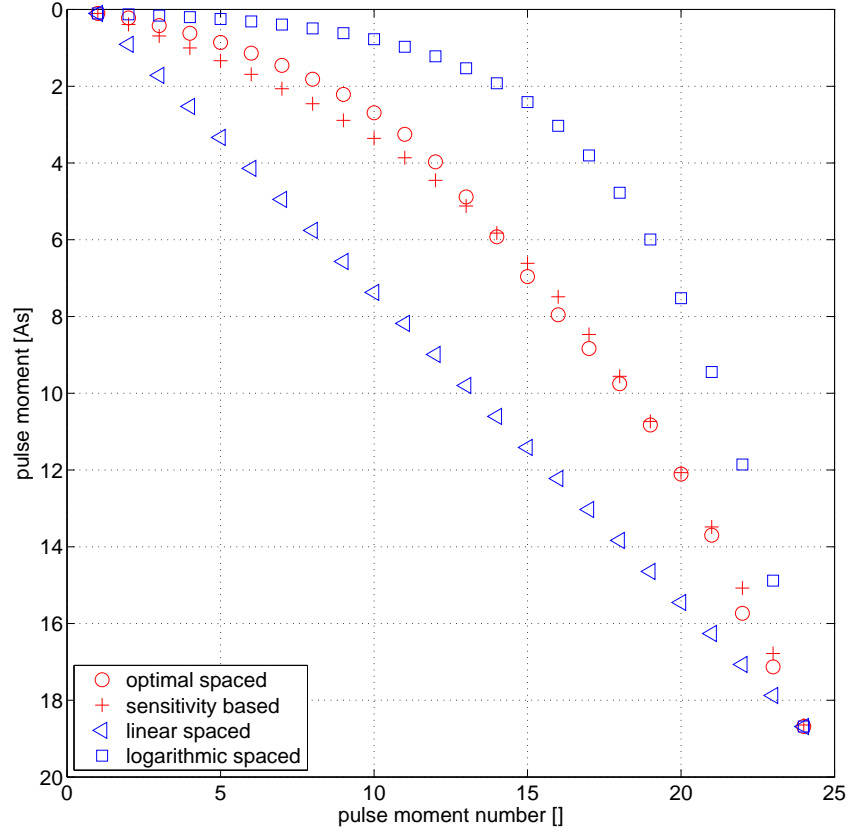


Figure 5.13: Distribution of pulse moments for different schemes (optimal, sensitivity based, linear, logarithmic distribution) with a fixed total number of 24. Loop size 96 m, 100  $\Omega$ m halfspace resistivity

resistivity and 24 pulse moments in the interval of  $[0.01 \ 24]$  As are calculated. The earth magnetic field inclination is  $60^\circ$  at  $|B|$  48000 nT. Figure 5.13 shows these pulse moment distributions including the sensitivity based sequence proposed by Legchenko and Shushakov (1998). This sequence is actually implemented as standard pulse moment distribution of the MRS measurements device Numis by Iris Instruments. It turns out that the sensitivity based is similar to the optimal distributed. A common measure to estimate inversion stability is the condition number

$$c = \frac{s_{min}}{s_{max}}. \quad (5.20)$$

Concerning the 3 different pulse moment distribution (optimal, linear, logarithmic) the condition numbers are:  $c_{optimal} = 56$ ,  $c_{linear} = 77$ ,  $c_{log} = 115$ . The complete singular value distribution for the Jacobian matrix based on the different pulse moment distributions is shown in figure 5.14. Even if the differences are small the Jacobian matrix based on optimal distributed pulse moments is more stable.

As a measure for inversion quality the L2 norm

$$\|\Delta m\| = \|M_{true} - M_{est}\|_2 \quad (5.21)$$

of the deviations from true model  $M_{true}$  to estimated model  $M_{est}$ . Figure 5.15 shows inversion results for the 3 MRS datasets (i.e. sounding curves after mono-exponential fit) based on

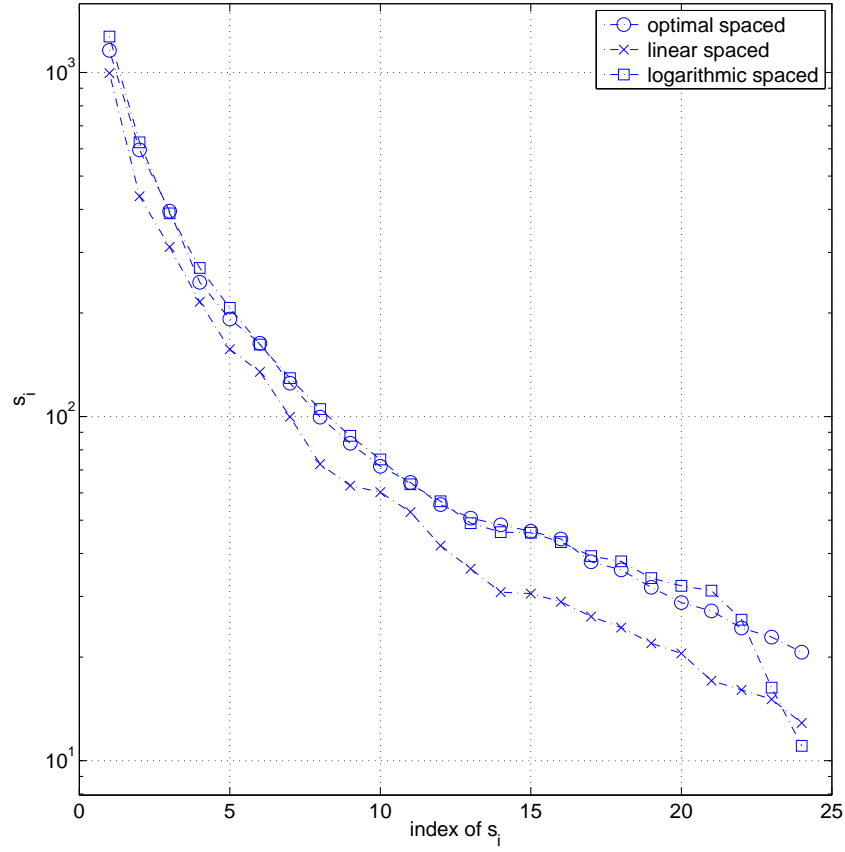


Figure 5.14: Singular value distribution of the optimal, linear and logarithmic pulse moments distribution.

synthetic data contaminated with noise (zero mean, 15 nV standard deviation applied to the sounding curve). In order to get statistical measures all inversions were 10 times repeated with different noise and the norms are calculated from the mean of these 10 independent runs. For both inversion schemes, smooth and block (after Hansen (1996)) the sounding curves based on optimal distributed pulse moments provides the lowest deviation norm. The estimated model provides additional insights into the resolution capabilities of the 3 sounding curves. The linear distributed is able to estimate the deepest water bearing structure best, but shows large variances and bad resolution for the near surface structure. The logarithmic distributed has contrary properties. Both can be explained by the distribution of pulse moments, since low pulse moments correspond to shallow depths and strong pulse moments to large depths. As expected the optimal set combines the resolution properties of both and has the best overall resolution.

### 5.3.3 Efficient number of pulse moments

Besides optimal distribution of pulse moments the number of pulse moments controls field efficiency. In this context, efficiency is the relation of obtained subsurface information versus various time/money dependent parameters, i.e., the number of pulse moments. Figure 5.16 shows the estimated models (with the same parameters as in figure 5.15) for sounding curves with increas-

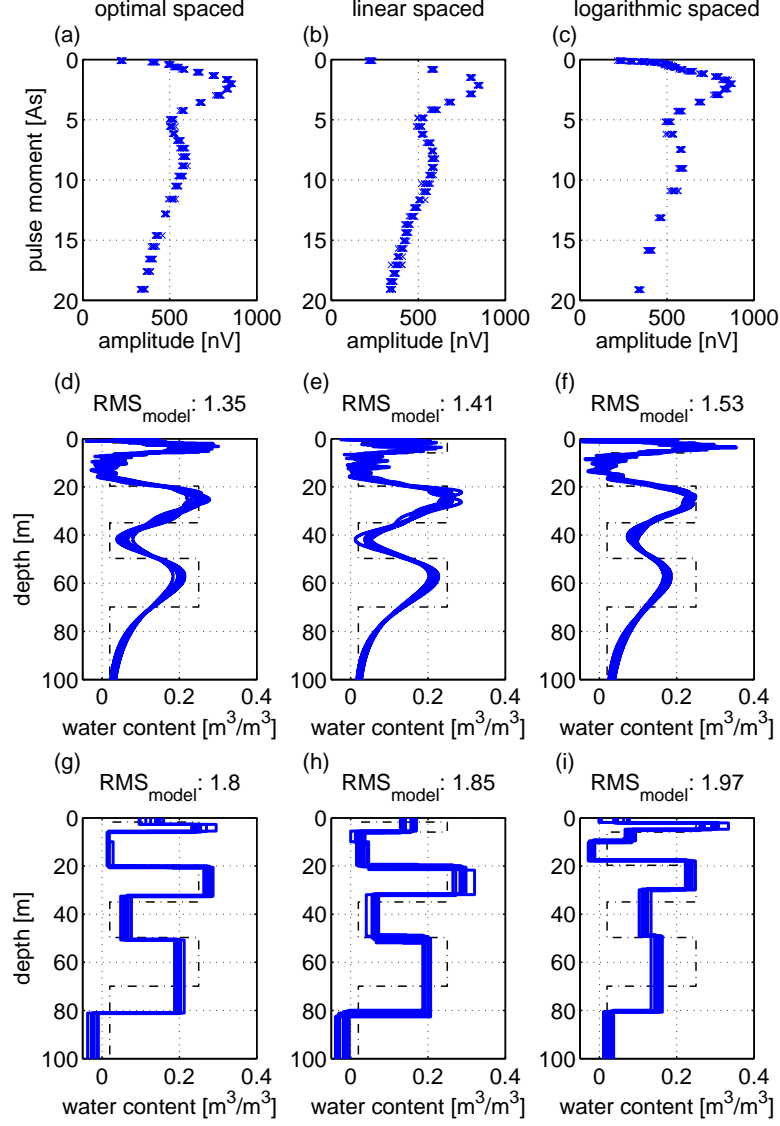


Figure 5.15: Estimated models derived from optimal, linear, logarithmic pulse moment distributions. a) - c) synthetic sounding curves, 10 individual sounding curves for every distribution contaminated with 15 nV Gaussian noise. Forward model based on 100  $\Omega\text{m}$  halfspace resistivity, loop diameter  $d = 96$  m, earth field  $|B| = 48000$  nT,  $60^\circ$  inclination. d) - e) Estimated model derived from smooth inversion. g) - h) Estimated model derived from block inversion. The norm of the model deviation is calculated from the mean of all 10 inversion runs.

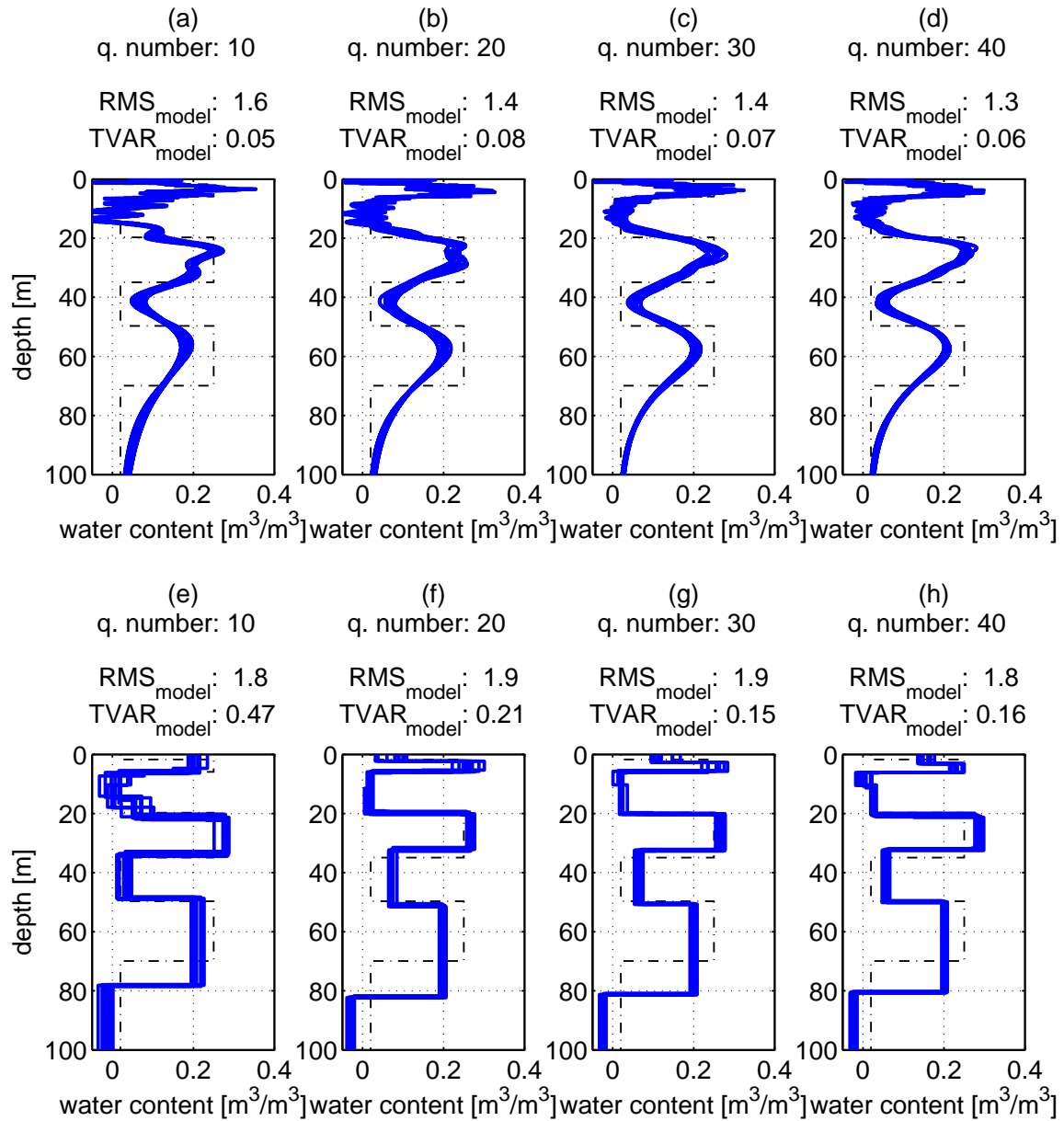


Figure 5.16: Estimated models derived from optimal pulse moment distributions with different total number of data. Forward model settings as in figure 5.15. 10 individual sounding curves for every distribution each contaminated with 15 nV Gaussian noise were inverted using a) - d) smooth and e) - f) block inversion. The model RMS and TVAR are means of the 10 independent inversion runs.

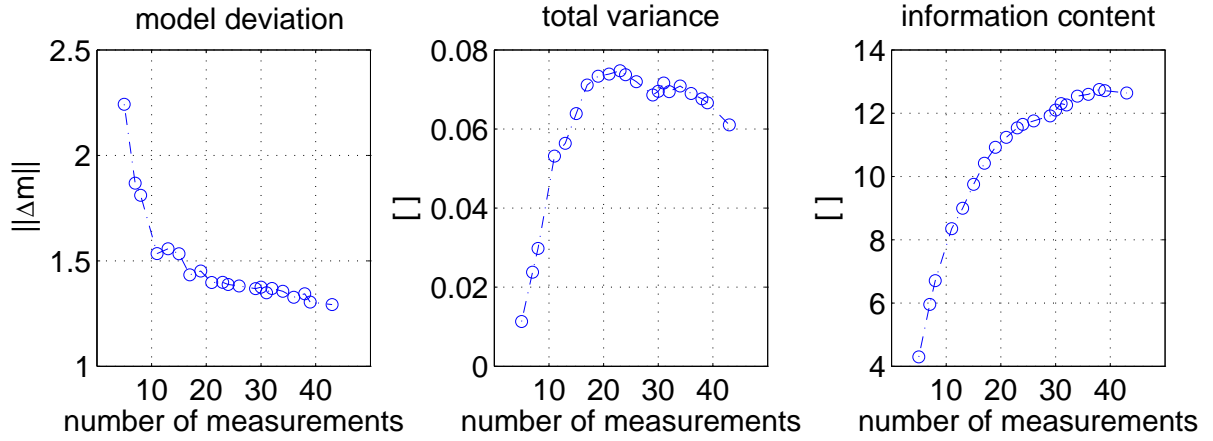


Figure 5.17: Determination of the total number of pulse moments for an efficient number of optimal distributed pulse moments. In extension to figure 5.16 the model RMS, total variance and information content is plotted for varied total number of optimal distributed pulse moments.

ing number of pulse moments (all using the optimal distribution) while figure 5.17 shows only the obtained measures of the model deviation norm (as a measure for inversion quality), the total variance TVAR (as a measure for stability)

$$TVAR = \sum_{i=1}^n var(M_{est}^i) \quad (5.22)$$

(with  $M_{est}^i$  the independent inversion runs and  $n$  the number of model basis layers) and the information content IC (as measure for resolution)

$$IC = \sum_{i=1}^n diag(\mathbf{R}_m) \quad (5.23)$$

with  $\mathbf{R}_m$  the model resolution matrix. As expected with increasing number of pulse moments the model deviation norm is decreasing, i.e., a better result compared to the subsurface truth is obtained. The increasing information content underlines this. The decrease of model deviation is fast for small numbers of pulse moments and slow for large numbers of pulse moments. Obviously, the efficiency of adding new pulse moments to the dataset decreases. One could try to calculate curvatures of the model deviation curve but the total variance is more useful. This measure shows a distinct maximum. This maximum arises due to the relation of increasing information content to reducing model variances.

1. For small number of measurements basically independent measurements are added that do not reduce the model variance but adding new information that causes the total variance to increase.
2. For large number of measurements basically dependent measurements are added that reduce the model variance but not adding new information that reduces the total variance.

number of q	2nV	15nV	45nV
144m10000Ω m	>40	17	12
96m1Ω m	>40	18	12
96m100Ω m	>40	24	15
96m10000Ω m	>40	24	15
48m1Ω m	30	12	7
48m100Ω m	35	14	7
48m10000Ω m	40	15	7

Table 5.2: Total number of pulse moments to get an efficient dataset while the maximum pulse moment is fixed to current equipment limitations.

confident depth [m]/ number of q	$q_{max}$ 10As	20As	50As	100 As
144m10000Ω m	83/17	120/28	180/32	230/36
96m10000Ω m	68/18	95/24	135/28	175/32

Table 5.3: Total number of pulse moments and confident depth versus maximum pulse moment at 15 nV noise.

Therefore, the maximum of the total variance is defined as the total number of pulse moments to get an efficient dataset. Hence, for the given example of a 96 m diameter loop at 100 Ω m halfspace resistivity at 15 nV noise we obtained a dataset of optimal distributed pulse moments with 20 measurements providing the maximum subsurface information in relation to maximum efficiency.

### 5.3.4 Efficiency in dependency on loopsize, noise amd maximum pulse moment

Since dependent pulse moments are related to the level of noise as well as on the Jacobian matrix, i.e., the loop size, resistivity and maximum pulse moment, all of these have to be taken into account. First, table 5.2 lists the total number pulse moments while the maximum pulse moment is restricted to the numis equipment power limitations, i.e., a pulse moment of 20 As for 48 m, 96 m and 11 As for 144 m (Eq. 5.2.3). The number decreases with increasing noise level (that is obvious) and/or increasing conductivity that is due to the decreasing penetrations depth.

In subsection 5.2.3 it was shown that the confidence depth of a 144 m loop is less compared to 96 m loop due to the current limitations. Thus, neglecting the power limitations, the confidence depth and the number of pulse moments for variation of maximum pulse moment was calculated to obtain a need of power for a certain loop size to be used efficiently (Tab. 5.2). Increasing the loop diameter to 144 m becomes efficient if the available pulse moment is up to 20 As. Furthermore, from table 5.3 the relationship of figure 5.7 between confidence depth and maximum pulse moment can be confirmed.



## 5.4 The transformed inverse problem

The MRS forward and inverse problem (Eq. 5.1) is a linear problem. The forward operator maps a model with elements  $m \in \mathbb{R}$  into data element  $d \in \mathbb{C}$ . But, if the problem is ill-posed the inversion might map  $d \in \mathbb{C}$  into  $m \in \mathbb{R}$ . Consequently, handling noise contaminated data the estimated model can easily contain elements  $m \in \mathbb{C}$ . Therefore, the first transformations, already presented in equation 5.2, is to separate real and imaginary part to ensure a real valued model. This separation doubles the amount of equations and leads to improved inversion results in terms of stability and resolution. It is a general property of transformations (Guenther et al. (2008)) that reducing the dimension of data or model space improves the stability and enhances the inversion result.

### 5.4.1 Model space transformations

In respect to the surface NMR method the model space is the subsurface water content domain. Obviously, besides being a real number the water content is a positive value and cannot be larger than 100 % or  $1m^3/m^3$ . Therefore a transformation should be applied that restricts this model space first to positive values and second to an upper boundary. That is, a function has to be found that maps a value  $a \in [-\infty, \infty]$  into  $b \in [0, c]$  with  $c$  the upper boundary (ub). Therefore, the kernel function has to be transformed, i.e., a sensitivity function appropriate to these targets has to be derived. In general the sensitivity is

$$J_{ij} = \frac{\partial D_i}{\partial M_j} = \mathbf{G} \quad (5.24)$$

with  $\mathbf{G}$  the kernel function and for any transformation  $f$

$$J_{ij} = \frac{\partial D_i}{\partial f(M_j)} = \frac{\partial D_i}{\partial M_j} \cdot \frac{\partial f(M_j)}{\partial M_j} = G_{ij} \cdot \frac{\partial f(M_j)}{\partial M_j}. \quad (5.25)$$

To ensure positive values the logarithm  $f(m) = \log(m)$  can be used

$$J_{ij}^{log} = G_{ij} \cdot m_j. \quad (5.26)$$

An upper boundary can be applied using the logarithm, too. Here a shifted and scaled (to ensure values between  $[0, ub]$ ) tangens function (Hertrich et al. (2008)) is applied

$$f(m) = \tan \left( \pi \left[ \frac{m}{ub} - 0.5 \right] \right) \quad (5.27)$$

and the Jacobian reads

$$J_{ij}^{tan} = G_{ij} \cdot \cos \left( \pi \left[ \frac{m_j}{ub} - 0.5 \right] \right)^2 \cdot \frac{ub}{\pi} \quad (5.28)$$

### 5.4.2 Data space transformations

Besides obvious restrictions at the model space, limitation at the data space is less straight forward. The first step is to transform the forward equation into the amplitude domain. Below the derivation of equation 5.5 is given.

According to a real valued model space the forward problem is separated

$$\begin{aligned} \mathbf{d} &= \mathbf{Gm} \\ \mathbf{A} &= \text{real}(\mathbf{G}) \\ \mathbf{B} &= \text{imag}(\mathbf{G}) \\ \text{real}(\mathbf{d}) &= \text{real}(\mathbf{Gm}) \stackrel{m_i \in \mathbb{R}}{=} \mathbf{Am} \\ \text{imag}(\mathbf{d}) &= \text{imag}(\mathbf{Gm}) \stackrel{m_i \in \mathbb{R}}{=} \mathbf{Bm} \end{aligned}$$

and reads using amplitudes

$$|\mathbf{d}| = |\mathbf{Gm}| = \sqrt{(\mathbf{Am})^2 + (\mathbf{Bm})^2}$$

or for a single element

$$|d(1)| = \sqrt{(A(1,1)m(1) + A(1,2)m(2) + \dots + A(1,j)m(j))^2 + \dots + (B(1,1)m(1) + B(1,2)m(2) + \dots + B(1,j)m(j))^2}$$

The Jacobian  $J(1,1)$  for this single data element  $|d(1)|$  in respect to the model  $m(1)$

$$\begin{aligned} J(1,1) &= \frac{\partial |d(1)|}{\partial m(1)} \\ &= \frac{[A(1,1)m(1) + \dots + A(1,j)m(j)]A(1,1)}{|d(1)|} \\ &+ \frac{[B(1,1)m(1) + \dots + B(1,j)m(j)]B(1,1)}{|d(1)|} \end{aligned}$$

or any elements

$$\begin{aligned} J(i,j) &= \frac{|d(i)|}{m(j)} \\ &= \frac{[A(i,1)m(1) + \dots + A(i,j)m(j)]A(i,j)}{|d(i)|} \\ &+ \frac{[B(i,1)m(1) + \dots + B(i,j)m(j)]B(i,j)}{|d(i)|}. \end{aligned}$$

Finally, the Amplitude Jacobian reads

$$J^A(i,j) = \frac{\text{real}(d(i))A(i,j) + \text{imag}(d(i))B(i,j)}{|d(i)|}. \quad (5.29)$$

A common approach in geophysical inversion theory is to transform the data into the same domain as the model. That is, in DC-Electric measurements are transformed from the voltages into pseudo resistivities. Then these pseudo values are used for inversion. This ensures equal scales

on both sides of the equations and is important if transformation (e.g. logarithm for resistivities) shall be applied. Consequently, the extrapolated initial voltages can be transformed into pseudo water content. According to DC-Electrics this is the voltage measured for a homogeneous half space at a certain water content.

In order to apply a transformation that ensures positive data, amplitudes are used to calculate the pseudo water content. Therefore, the sounding curve  $\mathbf{d}^k$  for a homogeneous half space for full saturation (100 %) is calculated

$$\mathbf{d}^k = \sum_j J_{ij}^A \quad (5.30)$$

and used for both side multiplication. For a single pseudo water content (pswc) data element  $d^{pswc}$

$$d^{pswc}(i) = d(i)/d^k(i) \quad (5.31)$$

and for the pswc Jacobian matrix  $J^{pswc}$

$$J^{pswc}(i, j) = J^A(i, j)/d^k(i). \quad (5.32)$$

Now, using the pswc the data space can be restricted with upper and lower boundaries, e.g. using logarithm or tanges transformation. Consequently, model and data space can be limited to reasonable values. In general a both side transformation reads (Guenther (2004))

$$J_{ij} = \frac{\partial f(D_i)}{\partial f(M_j)} = \frac{\partial D_i}{\partial M_j} \cdot \frac{\partial f(d_i)}{\partial d_i} / \frac{\partial f(M_j)}{\partial M_j} \quad (5.33)$$

The Jacobian matrix using pswc and logarithm transformation at both sides then reads

$$J_{ij}^{log,log} = G_{ij} \cdot \frac{m_j}{d_i}. \quad (5.34)$$

and using the tanges

$$J_{ij}^{tan,tan} = G_{ij} \cdot \frac{\cos\left(\pi \left[\frac{m_j}{ub} - 0.5\right]\right)^2}{\cos\left(\pi \left[\frac{d_i}{ub} - 0.5\right]\right)^2}. \quad (5.35)$$

Unfortunately, all transformations turn the linear inverse problems transforms into a non linear, i.e., a Jacobian matrix that is model dependent. The degree of non-linearity is different, as shown in section 5.1.1. The amplitude Jacobian is only slightly non-linear while the tangens transformation shows large the model dependencies (Fig. 5.18). The amplitude Jacobian and the Jacobian using a tanges transformation on both model and data space for a 2 aquifer situation are shown. Clearly using the tanges transformation the Jacobian is focused on the areas with suitable water content. This is due to the multiplication of the original kernel function with the water content model and the data. Both data and water content become smaller for decreasing amount of water. Therefore, introducing the logarithm and tanges transformation the Jacobian (or sensitivity) is “automatically“ focused to the regions of interest that should finally improve the resolution capabilities.

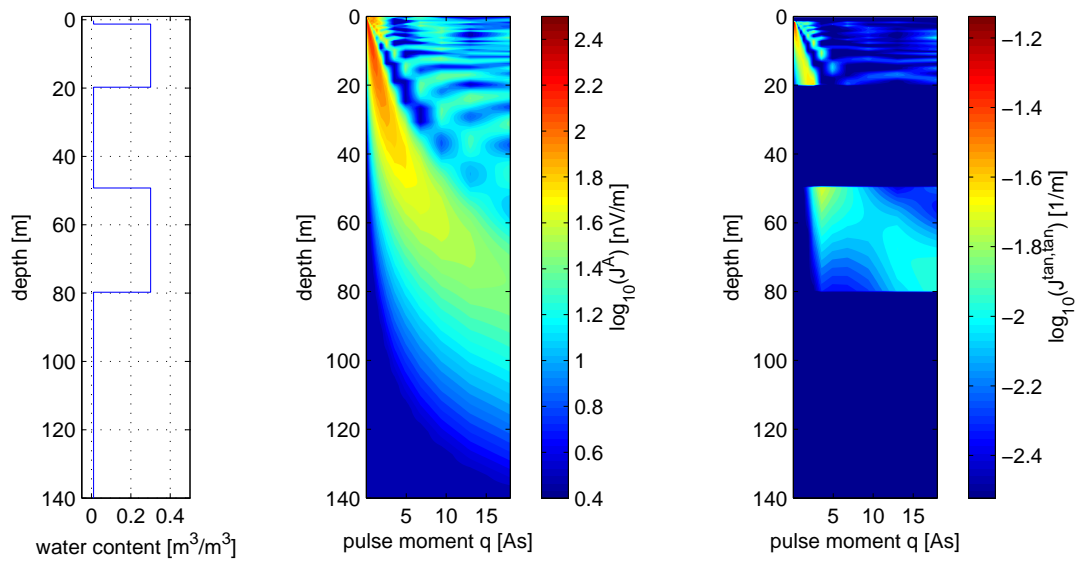


Figure 5.18: Jacobian matrix for a non homogeneous subsurface water content distribution (left). Middle: Amplitude Jacobian  $J^A$ . Right: Jacobian matrix for tangens transformation on both model and data space.

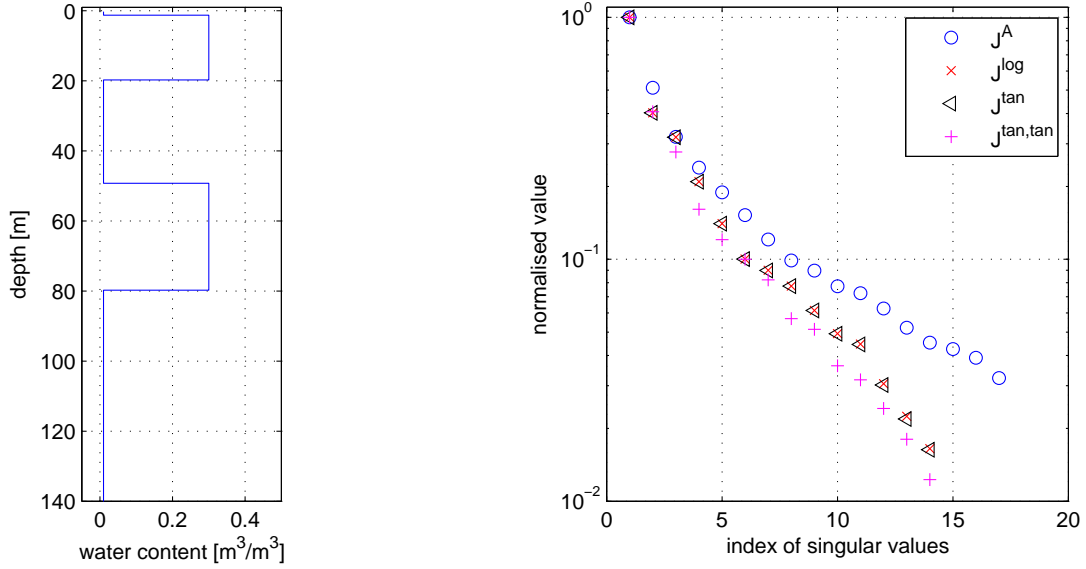


Figure 5.19: Singular value distribution for different transformation with a non-homogeneous water content model.

### 5.4.3 Evaluating the use of transformations

Besides analysing the Jacobian matrix in order to compare and evaluate the properties of the transformed inverse problem next the singular value distribution is compared in figure 5.19 for the same water content distribution as in figure 5.18. Apparently, the singular value distribution with transformations performs worse than without, i.e., decreases faster. Taking into account that the columns of the Jacobian matrix are close to zero at depth with low water content the distribution of singular value is not surprisingly. In general, one should be aware of comparing singular value distributions based on different discretisation in model or data space. Either a higher data or model space sampling would improve the singular value distribution, i.e., increasing the number of none zero value or cause a less fast decrease. In fact, the Jacobians are equally sampled but the transformation maps some columns to zero. Therefore, the same effect as no sampling or no information occurs. Consequently, the distribution of singular values for the transformed Jacobians is only apparently worse. But however cannot be evaluated as better.

However, the distribution of the both side transformation in model and data space shows the fastest decrease. Therefore, the singular value distribution only for the amplitude Jacobian and the transformation into pseudo water content data space is compared for a homogeneous halfspace in figure 5.20. Again, the distribution using the pseudo water content decreases faster than for the amplitudes and might be evaluated as worse. But since the weight on the lines of the Jacobian matrices has been changed by the transformation from volt to pseudo water content the Picard plot is more useful. The Picard plot provides a criterion up to which index of singular values a truncated svd inversion is stable. According to the svd solution the more singular values can be used the better the estimated solution. The Picard criterion now states that singular value can be used for globally decreasing  $|u_i^T d|/s_i$ . Concerning figure 5.20 the index for  $J^A$  is about 10 and for the  $J^{pswc}$  approximately equal or slightly larger. Consequently, the transformation into pswc does not worse the inverse problem but allows the application of

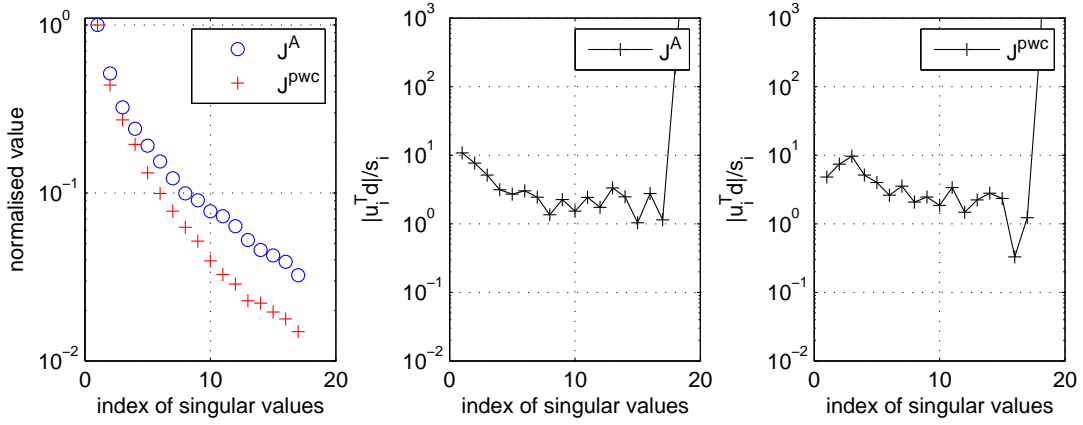


Figure 5.20: Comparison of amplitude Jacobian and transformation into the pseudo water content data space for homogeneous halfspace using the singular value distribution (left) and the Picard plots for the amplitudes (middle) and pseudo water content (right).

a equal transformation also at the data space.

Finally, estimated solutions based on the same data are compared in figure 5.21. The signals were generated at the base of nmr signals and mono-exponential fitted to create the initial amplitudes. Then the same initial values are used to test 4 inversion schemes

1. Amplitude inversion (standard application)
2. Logarithmic transformed model space
3. Tangens transformed model space with  $0.4 [m^3/m^3]$  upper boundary
4. Tangens transformed model and data space with  $0.4 [m^3/m^3]$  upper boundary.

This is repeated 20 times in order calculate the mean of the model deviation (estimated model - true model) using the  $L_2$  norm. The standard deviation of the data fit was set to 30 [nV].

As expected the model and data space tangens transformed inverse problem provides the best solution. The deviation to the true model decreases with increasing constraints. The logarithm ensures a positive water content and improves the model uncertainty compared to the amplitude inversion that shows negative water content for large depth and at depths about 30 m. But due to the missing upper boundary and the focused Jacobian the estimated solution often overestimates the water content while the thickness of the layer is underestimated. This effect can be reduced by introducing an upper boundary using the tangens transformations. Finally, due to constraints also on the data space the model variability for larger depth decreases by the both side transformation and the resolution increases. Since all inversions show the same data fit (the data error was estimated from the exponential fit) the tangens transformation should be preferred.

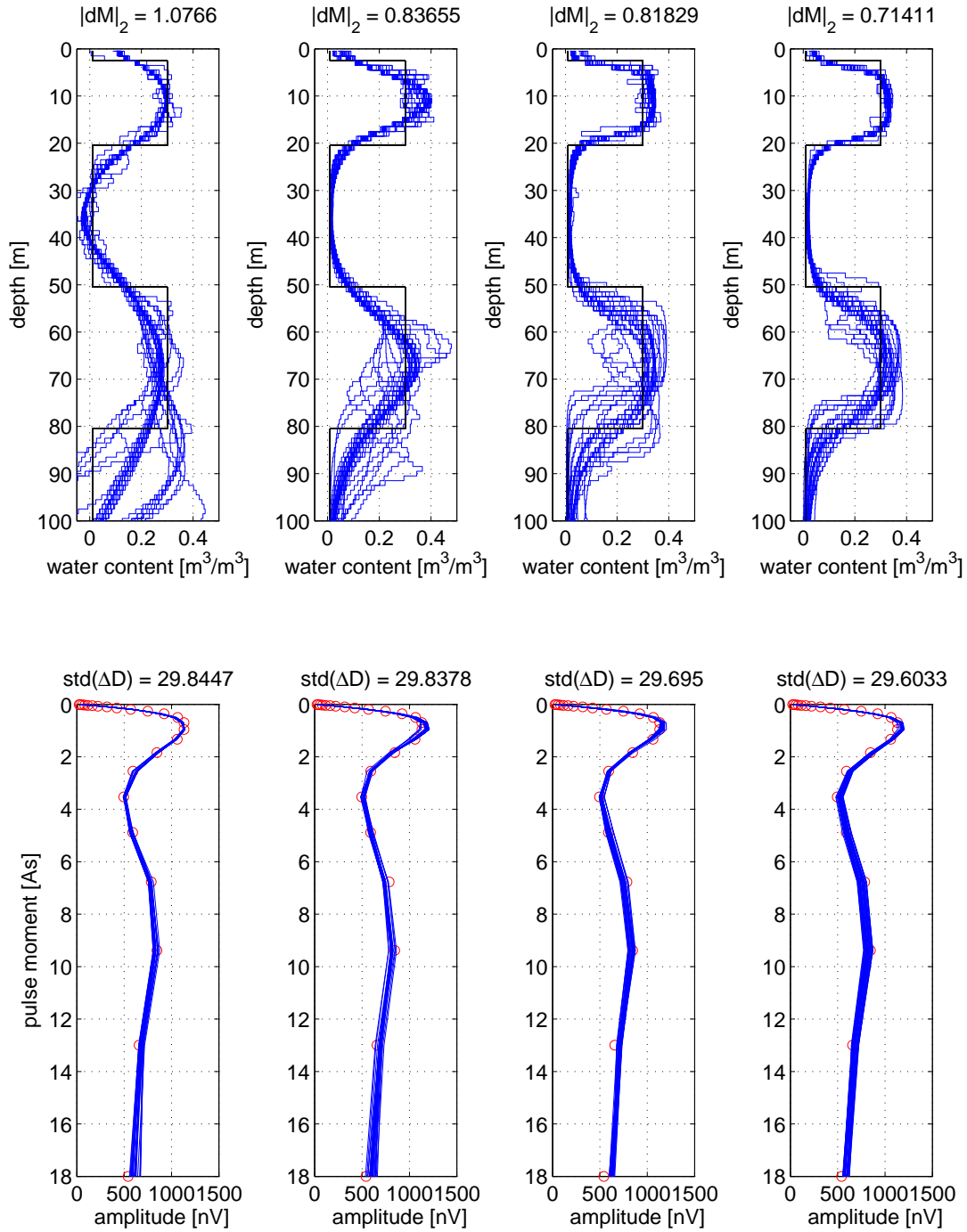


Figure 5.21: Comparison of estimated solutions using (from left to right) amplitude, logarithmic transformed model space, tangens transformed model space and tangens transformed model and data space. Bottom: All 20 independent contaminated sounding curves (red circles) and the forward responses (blue line). Top: All 20 inversion results (blue line) and synthetic model (black line). The model deviation is the  $L_2$  norm of the deviation of the true model to the mean solution of all 20 runs.

## 5.5 Outlook on 2D Resolution

An important step during the development of a geophysical technique is to overcome the restrictions for both modelling and inversion on a lateral layered earth, i.e., 1D condition. This opens a new field of applications but also includes new field layout to improve the lateral resolution. This section shortly summarises the development and improvement taking the step from 1D to 2D and presents a first analysis of the newly introduced measurement layout concerning resolution properties and layout strategies.

**From 1D to 2D** The first misfit estimations using a 2D water content distribution (i.e. a 2D forward operator) and comparing to 1D inversion results were presented by [Eikam \(2000\)](#) and [Warsa et al. \(2002\)](#). The name Magnetic Resonance Tomography (MRT) for 2D and 3D applications of the surface NMR technique in combination with first 2D inversion results was introduced by [Hertrich et al. \(2005\)](#) and in more detail in [Hertrich et al. \(2007\)](#).

Beginning with the standard coincident configuration an expected 2D section can be measured by several soundings at different positions along a profile as shown in figure 5.22. The resulting sounding curve might be inverted like 1D depth sounding and plotted. The distance between these single soundings (Fig. 5.22 one loop diameter) might be adopted depending on the structure to be expected.

Typically these 1D inversion results are displayed together using a contour plot as shown in figure 5.23a.

Since the basic surface NMR equation (Eq. 2.11) already holds for 3 spatial dimensions a 2D inversion is straight forward. In contrast to 1D inversion the kernel function is not pre-integrated over  $x$  and  $y$  but only over one lateral dimension depending on the profile orientation. Remark, the kernel function is not symmetric due to the earth field inclination, i.e., the profile direction is of importance in order to integrate over the perpendicular direction.

Hence, using a 2D inversion code that handles 2D water content distribution the estimated model can be significantly improved as shown in figure 5.23b. The inversion was carried out using an SVD based solver as for the 1D inversion while the data is noise free.

Obviously, the quality of the estimated 2D water content distribution using a 1D scheme depends on the lateral change of the structure to be investigated as for any other geophysical

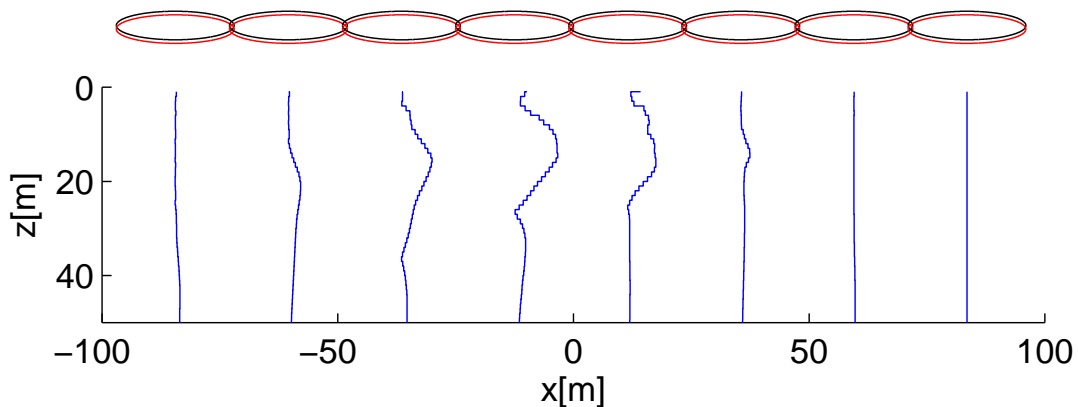


Figure 5.22: Scheme of a 2D survey using a coincident loop layout (transmitter (red) and receiver (black) coincide) and 1D water content inversion (blue line).



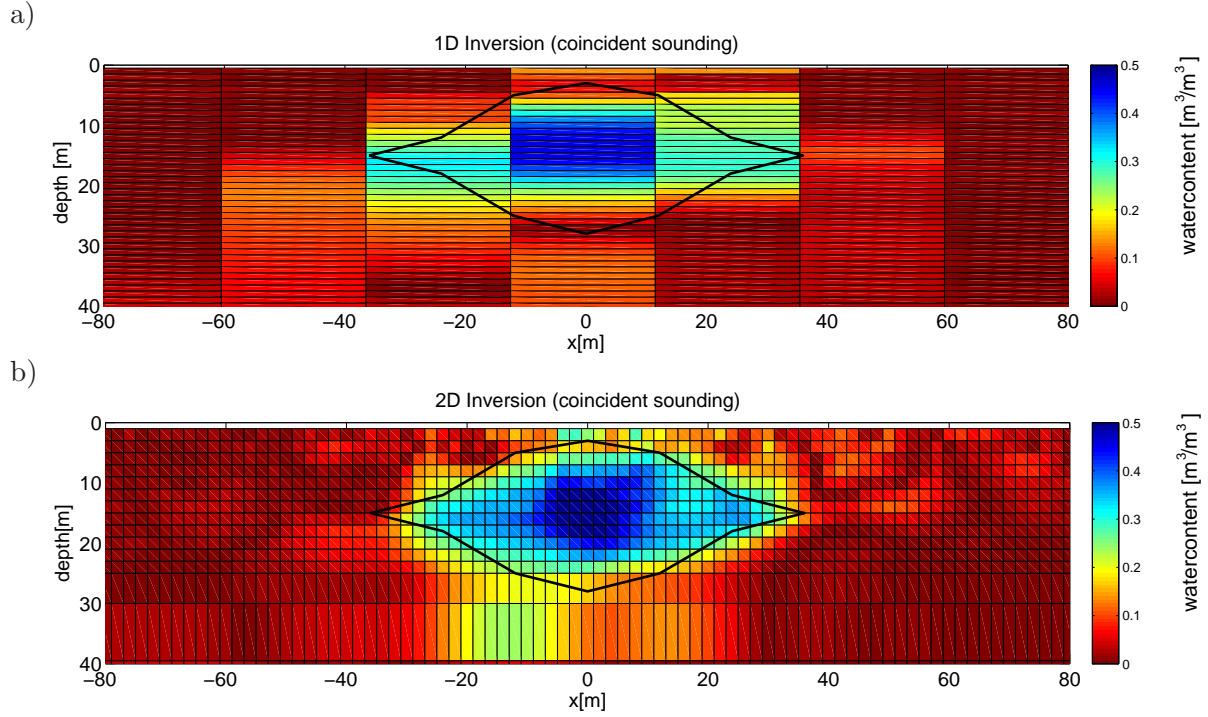


Figure 5.23: Comparison of 1D inversion shown as a contour of single inversion results (a) and true 2D inversion using the same noise free data. The true subsurface model is marked by the black line and represents a water lens at 30 % water content with a background water content of 0 %. The modelling parameter are: 48 m loop diameter,  $|B| = 48000$  nT earth magnetic field strength at  $60^\circ$  inclination.

method. The larger the lateral homogeneity of the structure the better becomes the estimation with reality. Some rule of thumb in order to apply 1D inversion of even 2D subsurface will be presented later. It depends on the loop size and cannot be chosen freely since also the maximum depth depends on the loop size.

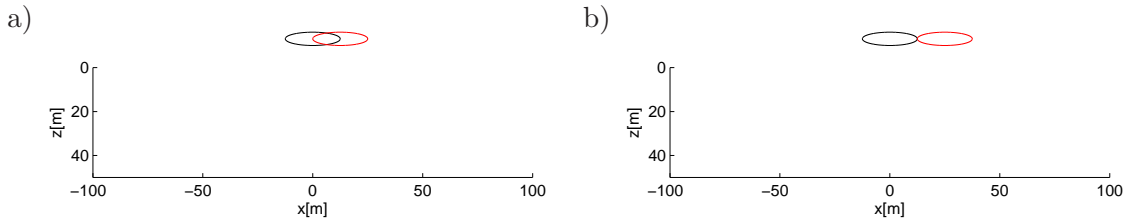


Figure 5.24: Separated loop sounding. Transmitter and receiver do not coincide but can be separated by a certain distance, e.g. half overlapping (a) or edge to edge (b).

**Separated loop measurements** Introduced by [Hertrich et al. \(2005\)](#) and triggered by the extended surface NMR forward formulation after [Weichman et al. \(2000\)](#) additional loop configurations besides the coincident layout using separated transmitter and receiver loops are of interest for 2D investigations. Figure 5.24 show schematically a separation of half the loop diameter (so called half overlapping) and one loop diameter (called edge2edge). It turned out that increasing the separation the geometrical relation of the receiver to the transmitter decreases the signal strength but apparently focuses the sensitivity in lateral direction as well as to smaller depth. Therefore, separated loop sounding promise increases resolution for 2D investigation.

As an outlook on the resolution properties of 2D investigation and especially on separated loop measurements a synthetic example using only the real part of the kernel function is calculated to provide a first insight on the resolution properties.

Figure 5.25 shows again standard 1D kernelfunctions for coincident, half overlapping and edge2edge measurements as well as the resolution matrix calculated using a truncated svd approach and cutting after the degree of freedom (for this problem) according to the distribution of singular values. The model and data space discretisation is equal for all examples. The kernels were calculated for insulation conditions.

Clearly, the vertical resolution power decreases for increased separations. The sensitivity focuses on near surface areas with increasing separation and the absolute sensitivity in nanoVolt per meter decreases as well. Consequently, separated loop sounding are not to be preferred for 1D vertical investigations.

Besides pre-integration over  $x$  and  $y$  to get a 1D kernel function for vertical inversion (and vertical resolution analysis), i.e., assuming lateral layered earth next the integration is over  $y$  and  $z$ . This results in a 1D kernel function as well but for horizontal inversion (and lateral resolution analysis), i.e., assuming a dike like vertical layered earth. This model does not have to much practical relevance but allows investigating lateral resolution very nicely. Figure 5.26 shows again the kernel function and the resolution matrices for the different layouts.

First, the kernel function for the coincident case is symmetric around the loop center. In order to interpret the resolution matrices, remark that the resolution matrix is  $x$  vs.  $x$  direction so the white loop does not represent true surface position in  $x$  and  $y$  but helps for orientation. According to the kernel function the resolution for coincident case is ambiguous. Using just a single sounding the lateral origin of the signal is not defined. Consequently, applications for 2D structures have to use many coincident soundings with a small increment in lateral position. Thus, the signal originates from a laterally limited area. That is, for a 50 m diameter loop approximately 100m around its midpoint. Consequently, as long as an expected structure is laterally homogeneous within this area 1D conditions are met.

If the transmitter and receiver are separated this lateral ambiguity is broken. The sensitivity

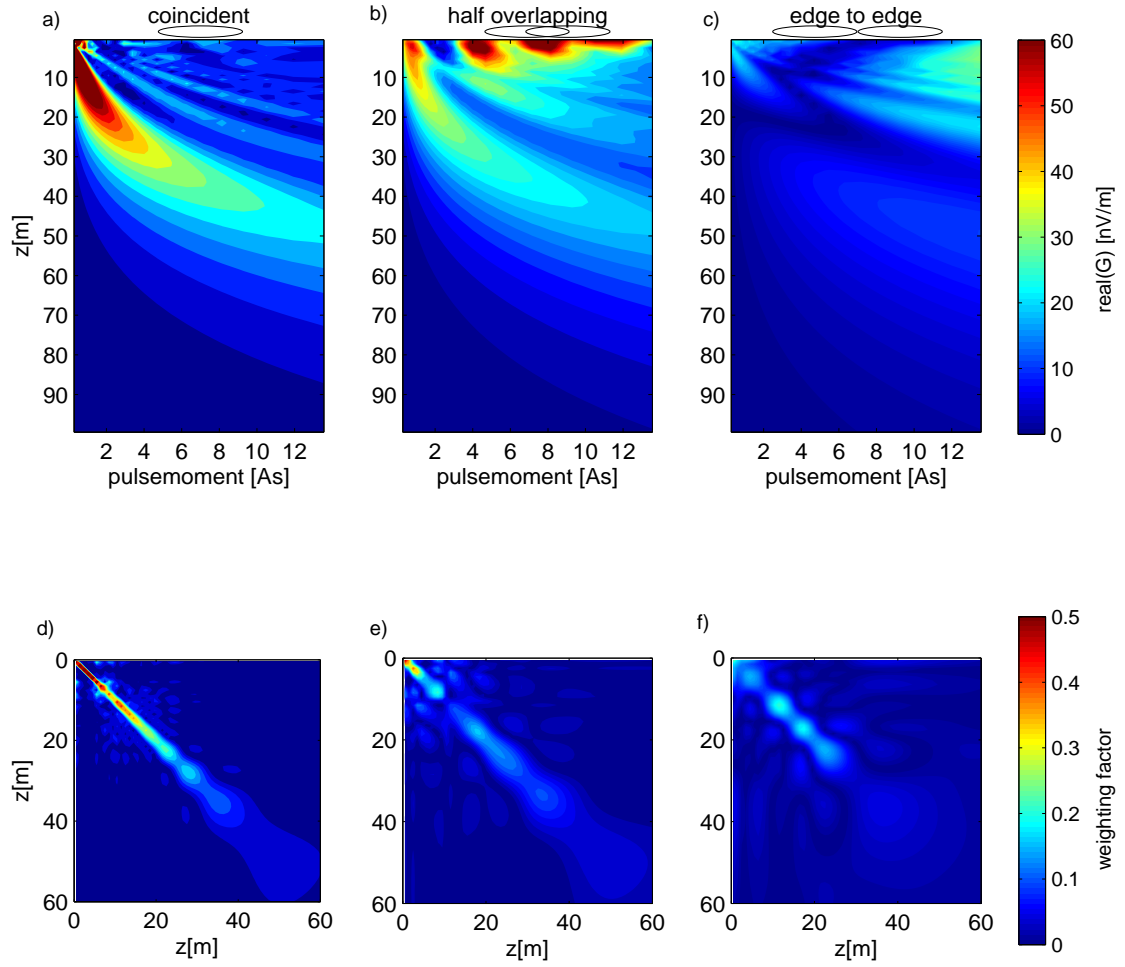


Figure 5.25: 1D kernel function and resolution matrices for lateral layered earth condition (standard 1D assumption). a) coincident, b) half overlapping and c) edge2edge

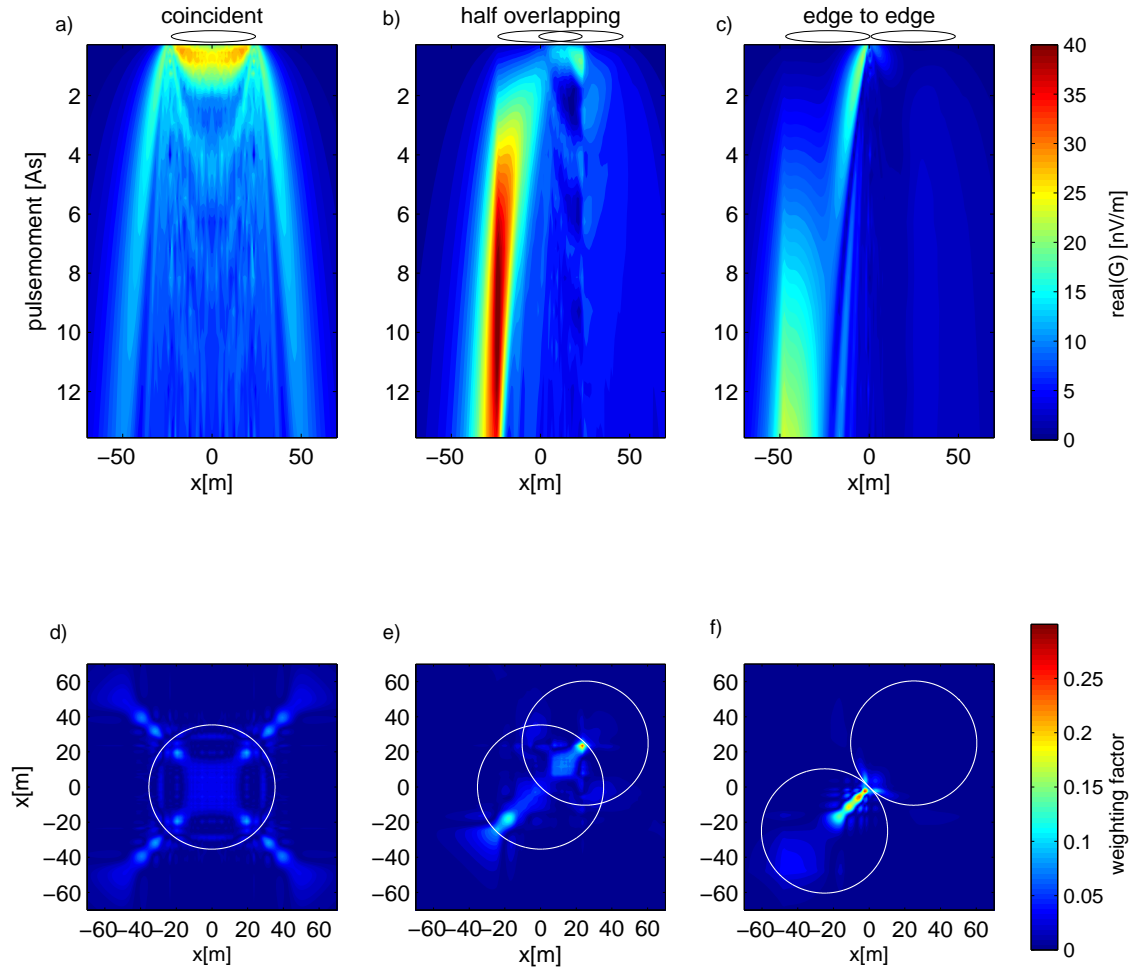


Figure 5.26: 1D kernel function and resolution matrices for vertical layered earth condition (dike like structure). a) coincident, b) half overlapping and c) edge2edge. d), e) and f) show the resolution matrices. The white circles present the size of the loop and measurement configuration just for orientation. Remark, the resolution matrix is  $x$  vs.  $x$  direction so the white loop does not represent true surface position in  $x$  and  $y$ .

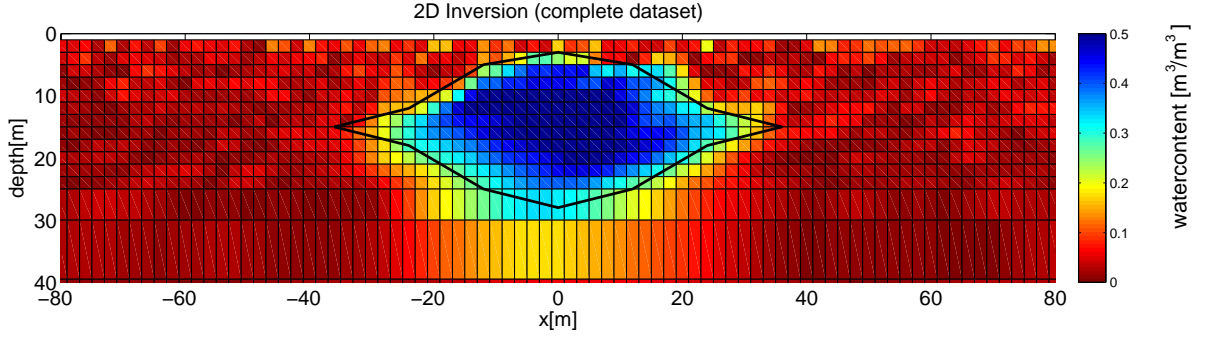


Figure 5.27: 2D inversion using the complete synthetic noise free dataset of coincident, half overlapping and edge2edge measurements. The loop diameter is 48 m, lateral increment of loop position is 24 m, i.e., half overlapping. This corresponds to 9 coincident, 16 half overlapping and 14 edge2edge soundings.  $|B| = 48000$  nT,  $60^\circ$  inclination and insulation conductivity condition.

focuses beneath the receiver loop and with increasing separation the lateral resolution improves. On the other hand, with increasing separation the total sensitivity in nanoVolt per meter decreases as well as the area of integration. That is, the detectable signal becomes smaller with increasing separation. As a consequence, separations larger than one loop diameter are not useful. In conclusion, separated loop measurements are important to improve lateral resolution without increasing the increment of lateral positions.

Next, a true 2D inversion using synthetic coincident, half overlapping and edge2edge measurements is carried out. The lateral increment for midpoint positions is half the loop diameter of 48m. The lateral extension of the area is from -96 m to +96 m. This corresponds to 9 loop positions and therefore 9 coincident, 16 half overlapping and 14 edge2edge soundings. Figure 5.27 shows the inversion result for noise free data. Compared to figure 5.23b based on only the coincident soundings the estimated model is clearly improved but it should be stated that the amount of data used for this inversion is fairly much larger.

Therefore, a direct view on the resolution is useful. Figure 5.28 shows exemplarily which cells of the 2D section influences a single cell. These weights are the main diagonal elements of the resolution matrix. It shows that for the coincident layout the vertical resolution is good, i.e., the area of influence is small. Laterally the area is large causing bad lateral resolution. The edge2edge layout shows inverse resolution properties, i.e., good lateral resolution and bad vertical as expected from the 1D analysis. Consequently, the combination of both improves the overall resolution very nicely.

**Conclusion** These first results show the general properties of 2D resolution in dependency on the layout. It is restricted to the real part of the kernel function as well as on noise free data and simple inversion schemes, i.e., truncated svd. For further investigations the amplitude signal should be taken into account as well as noise dependent analysis as shown for the 1D inversion.

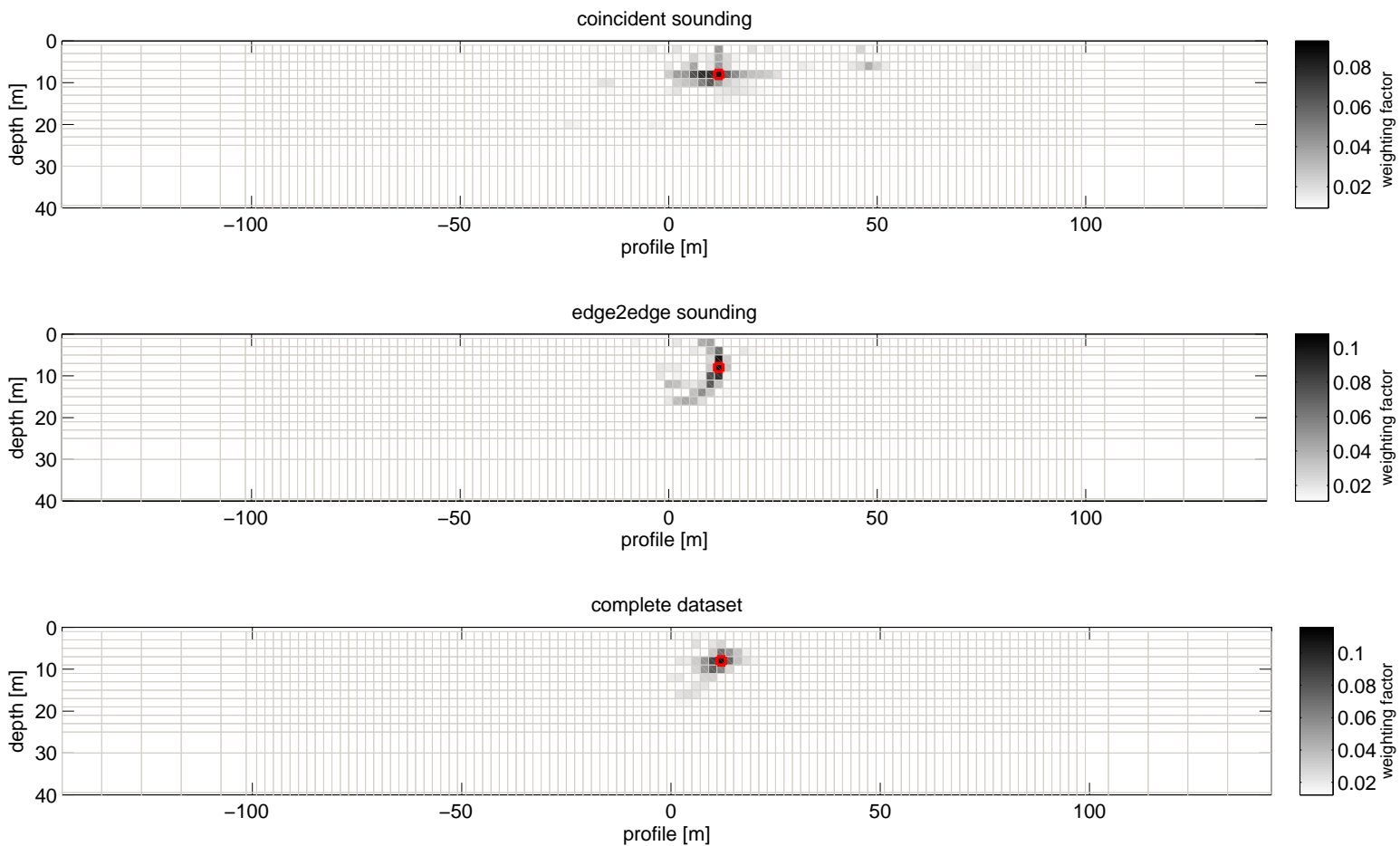


Figure 5.28: Cell resolution for the different layouts. The white to black colormap marks the influence weights for every cell to the original cell (red).

## 6 QT Inversion

According to chapter 3 and in order to motivate a new inversion scheme, the drawbacks of the currently used schemes are concluded first and schematically summarized in figure 6.1 and figure 6.2.

The initial value inversion uses a mono-exponential fit to derive the initial value. Hence, the final model of this approach only provides the subsurface water content. The decay times can be represented versus the pulse moment but cannot be inverted for depth. Furthermore, each of the mono-fits is independent of all other. Due to the integrating character of the kernel function signals of different pulse moments share depth ranges. Thus, neighbouring pulses are not independent. Consequently, this scheme has two major drawbacks:

1. Due to the dependency of different pulse moments but independent fitting information gets lost.
2. Taking different relaxation regimes, i.e., decay times into account a signal can be multi-exponential even if the single subsurface layers are of mono-exponential behaviour.

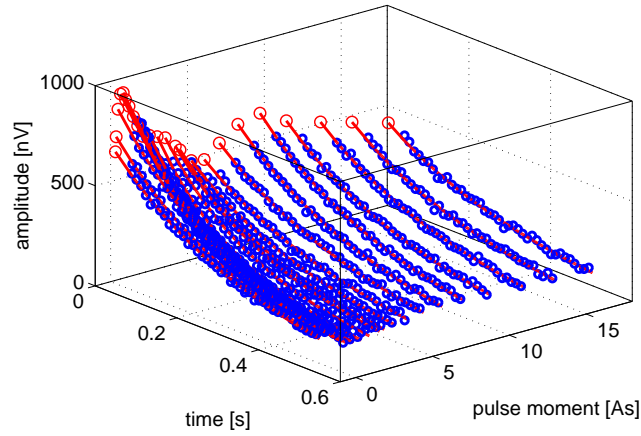
According to the inability of estimating the decay time as a function of depth [Legchenko and Valla \(2002\)](#) presented a new inversion scheme that has been extended by [Mohnke and Yaramanci \(2005\)](#). Here, the dataset is not extrapolated to the initial values but sub-datasets are extracted. These sub-datasets are measured values at a fixed time versus the pulse moment, i.e., a sounding curve at some other time than  $t = 0$ . The approach uses the amplitudes of the measured signal for the same reasons as discussed for the initial value inversion. In contrast to the initial value inversion not the amplitudes of the initial value is calculated but the amplitude of the relaxation signal. Thus, an overestimation according to figure 4.12 in subsection 4.3 can occur.

These amplitude subsets are inverted for water content in the same manner as for the initial value inversion. Consequently, one gets a subsurface water content vs. depth and record time. Since this water content dataset has already solved the integral character of the kernel function (i.e., the signal are separated to its original depths) mono-exponential properties of the subsurface are not mixed up to multi-exponential signals and one drawback of the initial value inversion is solved. Next, this water content data can be fitted by mono ([Legchenko and Valla \(2002\)](#)) or multi-exponential ([Mohnke and Yaramanci \(2005\)](#)) approach and the estimated model of this inversion scheme consists of both: the water content and decay time as a function of depth.

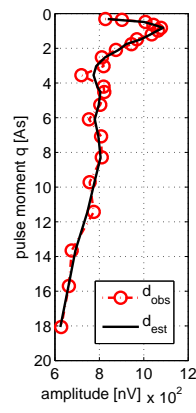
Although one drawback of mixed relaxation signals is solved, further drawbacks are:

1. The independent processing of dependent data still exist, since any inversion at every time step is not independent of the former or next one. Therefore, also using the time step inversion scheme information gets lost that might improve the estimated model.
2. A upper boundary for the water content inversion cannot be fixed due to the decay of the water content that has to be fitted during the second step.
3. Using the amplitude of the signal the decay times are overestimated.

a)



b)



c)

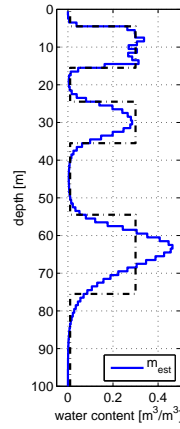


Figure 6.1: Scheme of initial value inversion. From the complete dataset (a) the initial values (only amplitudes shown here) (b) are derived by mono-exponential fitting and inverted to subsurface water content using the kernel function (c).



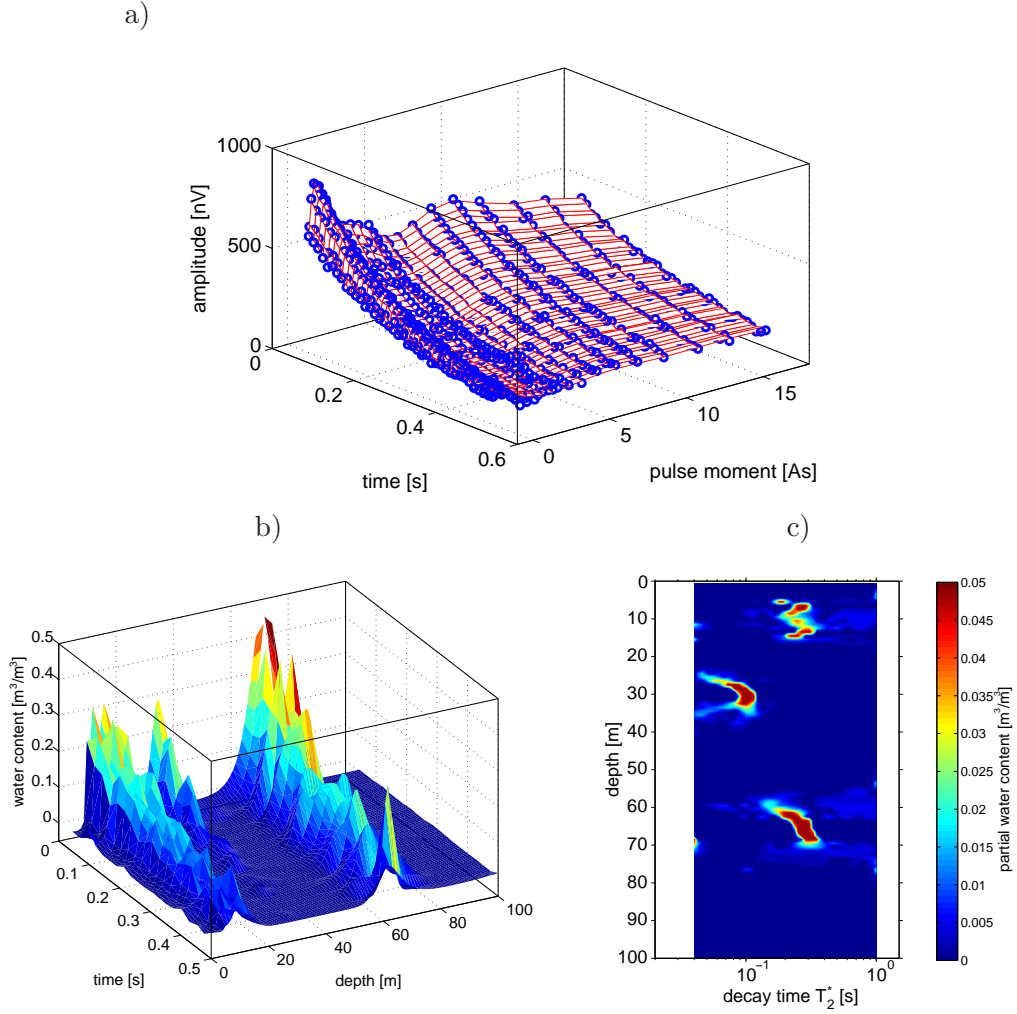


Figure 6.2: Scheme of time step inversion after [Mohnke and Yaramanci \(2005\)](#). From the complete dataset (a) subsets (i.e., sounding curves) at selected (or all) time steps are inverted for water content (red lines in a) represent the estimated data at this time step) corresponding to this time step, i.e., the data space of measured voltages is transformed into the water content space (b) via inversion. Next, at any depth these water content decay curves are fitted by multi-exponentials and the coefficients presented as partial water content (PWC) distribution in c).

In order to avoid overestimated decay times, the time step inversion is used different. Equal to the dataset processing for the QT inversion the corrected amplitudes (subsection 4.3) can be used for the time step inversion to ensure non biased decay time estimation. On the other hand, data space transformations cannot be applied as for the initial value inversion. The pseudo water content might be calculated but obviously negative data is expected, if the record length is larger than the decay time, i.e., no lower boundary can be fixed in the data space. Finally, figure 6.2 shows exemplarily a time step inversion using the corrected amplitudes and the logarithmic transformation at the model space. The water content vs. decay time is calculated using a multi-exponential fit to the water content dataset. In order to get a total (or due to the dead time extractable) water content, all coefficients at the different decay times might be summed up for total extractable water content. Summarising all the above it appears to be useful to solve the inverse problem in just a single step as it is presented in the following.

### 6.1 Forward operator

According to equation 2.11 the forward problem can be rewritten to

$$d(q, t) = \int G(\mathbf{r}, T_2^*, q, t) m(\mathbf{r}, T_2^*) dT_2^* d\mathbf{r} \quad (6.1)$$

using a general forward operator  $G(\mathbf{r}, T_2^*, q, t)$  that includes the relaxation process. If assuming 1D lateral homogeneous condition a pre-integration over  $x$  and  $y$  can be applied

$$d(q, t) = \int G(z, T_2^*, q, t) m(z, T_2^*) dT_2^* dz \quad (6.2)$$

and the inverse problem is of two dimensions, the depth  $z$  and the decay time  $T_2^*$ . In order to solve this numerically both dimension can be discretised and written in matrix notation (Eq. 6.3). Equation 6.3 shows that the original 1D kernel function  $G(z, q)$  remains and is multiplied by a relaxation term  $e^{-t/T_2^*}$ . Obviously, the model space is necessarily multi-exponential since the decay time is discretised and therefore smooth. On the other hand equation 6.2 can be used to derive a Jacobian matrix for a 2D block inversion to ensure mono-exponential layer properties. Here equation 6.3 is solved as an 2D smooth problem.

### 6.2 Inverse problem

There are some basic differences on solving equation 6.3 compared to the initial value inversion. In addition to a depth discretisation, the decay time is discretised in an appropriate range. That is, according to the detectable decay times. The dataset is about 24 pulse moments with time records sampled at 500 Hz. In total, this results in a forward operator that easily fills the size of 40000x6000. The dataset might be reduced in future but basically the problem is too large for an SVD based solver as used for initial value inversion. Therefore, in the following the conjugate gradient solver as presented in Guenther et al. (2006) is used.

Due to the two-dimensional model space an upper boundary for the total (extractable) water content cannot be applied directly since the model space is a PWC distribution. Thus, the total water content is the sum of all water parts and is not constraint in a first step. Therefore, only a lower boundary, i.e., the logarithm transformation is applied, yet.

To avoid a biased solution for the decay times the corrected amplitudes (subsection 4.3) are

$$\begin{bmatrix} d_1^1 \\ d_2^1 \\ \vdots \\ d_l^1 \\ d_1^2 \\ \vdots \\ d_l^m \end{bmatrix} = \begin{bmatrix} G(z_1, q_1)e^{-t(1)/T(1)_2^*} & \dots & G(z_k, q_1)e^{-t(1)/T(1)_2^*} & G(z_1, q_1)e^{-t(1)/T(2)_2^*} & \dots & G(z_k, q_1)e^{-t(1)/T(n)_2^*} \\ G(z_1, q_2)e^{-t(1)/T(1)_2^*} & \dots & G(z_k, q_2)e^{-t(1)/T(1)_2^*} & G(z_1, q_2)e^{-t(1)/T(2)_2^*} & \dots & G(z_k, q_2)e^{-t(1)/T(n)_2^*} \\ \vdots & \dots & \vdots & \vdots & \dots & \vdots \\ G(z_1, q_l)e^{-t(1)/T(1)_2^*} & \dots & G(z_k, q_l)e^{-t(1)/T(1)_2^*} & G(z_1, q_l)e^{-t(1)/T(2)_2^*} & \dots & G(z_k, q_l)e^{-t(1)/T(n)_2^*} \\ G(z_1, q_1)e^{-t(2)/T(1)_2^*} & \dots & G(z_k, q_1)e^{-t(2)/T(1)_2^*} & G(z_1, q_1)e^{-t(2)/T(2)_2^*} & \dots & G(z_k, q_1)e^{-t(2)/T(n)_2^*} \\ \vdots & \dots & \vdots & \vdots & \dots & \vdots \\ G(z_1, q_l)e^{-t(m)/T(1)_2^*} & \dots & G(z_k, q_l)e^{-t(m)/T(1)_2^*} & G(z_1, q_l)e^{-t(m)/T(2)_2^*} & \dots & G(z_k, q_l)e^{-t(m)/T(n)_2^*} \end{bmatrix} \begin{bmatrix} m_1^1 \\ m_2^1 \\ \vdots \\ m_k^1 \\ m_1^2 \\ \vdots \\ m_k^n \end{bmatrix} \quad (6.3)$$

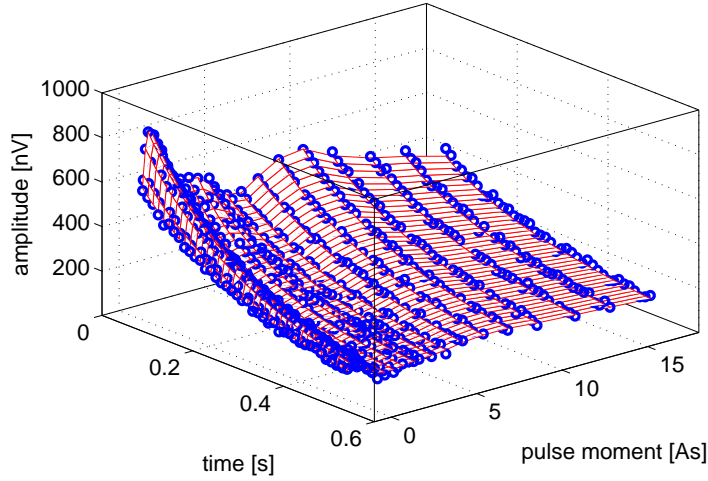


Figure 6.3: Schematically visualisation of a data fit presented by the QT inversion. This scheme takes the complete dataset build by the pulse moments  $q$  and the record time  $t$  into account and tries to find a solution that satisfies all data equally.

used. Here the phase and freq. offset is deleted from the complex signal. Thus, the real part can be used as amplitudes.

Finally, in addition and equal to the time step inversion no transformation on the data space is used since negative data is expected if the signal record time is long compared to the decay time.

Additionally, the new inversion scheme takes the complete dataset build by the pulse moment  $q$  and the record time  $t$  into account and tries to satisfy all data at once.

### 6.3 Synthetic comparison

In the following synthetic examples are used to compare all three inversion strategies. The synthetic model (Fig. 6.4) consists of 3 aquifers of different thickness and relaxation properties. The general modelling properties are:

- Circular loop of 96 m diameter, 1 turn
- Earth magnetic field at  $|B| = 48000$  nT and  $60^\circ$  inclination
- Subsurface resistivity according to the aquifer and aquiclude situation, i.e.,  $1000 \Omega m$  down to 5 m: representing the unsaturated dry zone;  $200 \Omega m$  down to 15m: the first medium sand aquifer;  $90 \Omega m$  down to 25 m: the first aquiclude;  $110 \Omega m$  down to 150 m: a mixed zone of aquifer and aquiclude of different coarse material and mineralisation; from 150 m on  $3 \Omega m$  halfspace
- 24 pulse moments in the range from 0.01 As up to 18 As maximum pulse moment.

The datasets have been contaminated using Gaussian noise at 5 nV standard deviation representing very favourable condition and 200 nV standard deviation for unfavourable conditions.

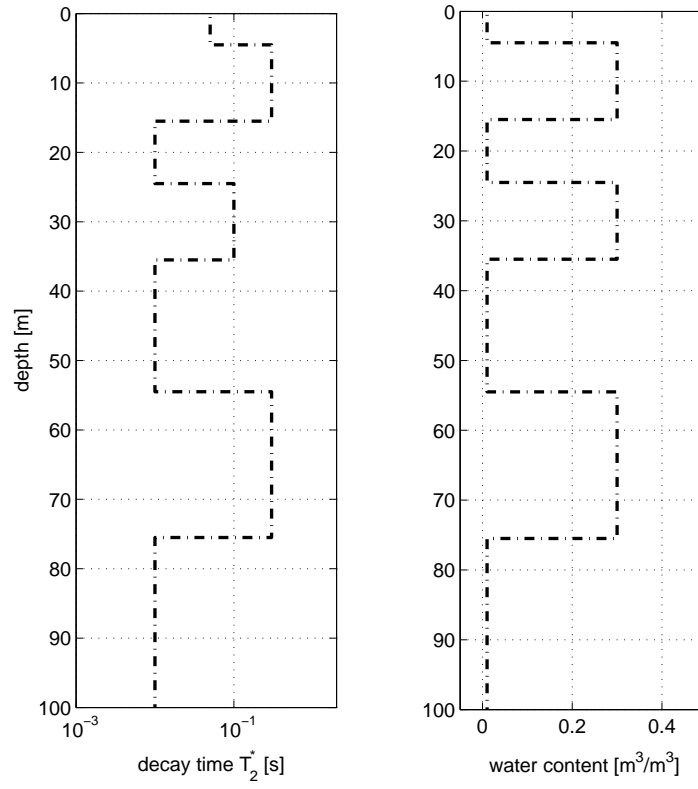


Figure 6.4: Synthetic model for tests and comparison of the different schemes.

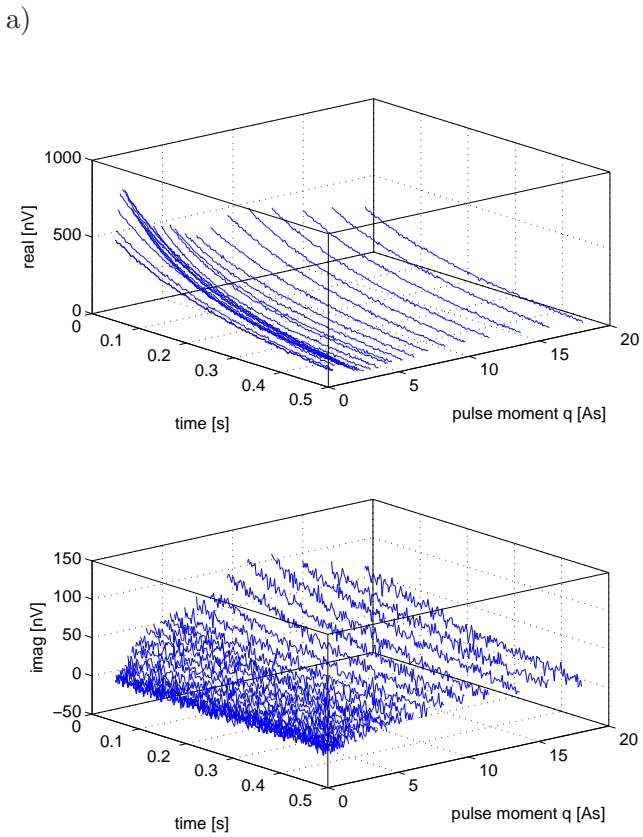
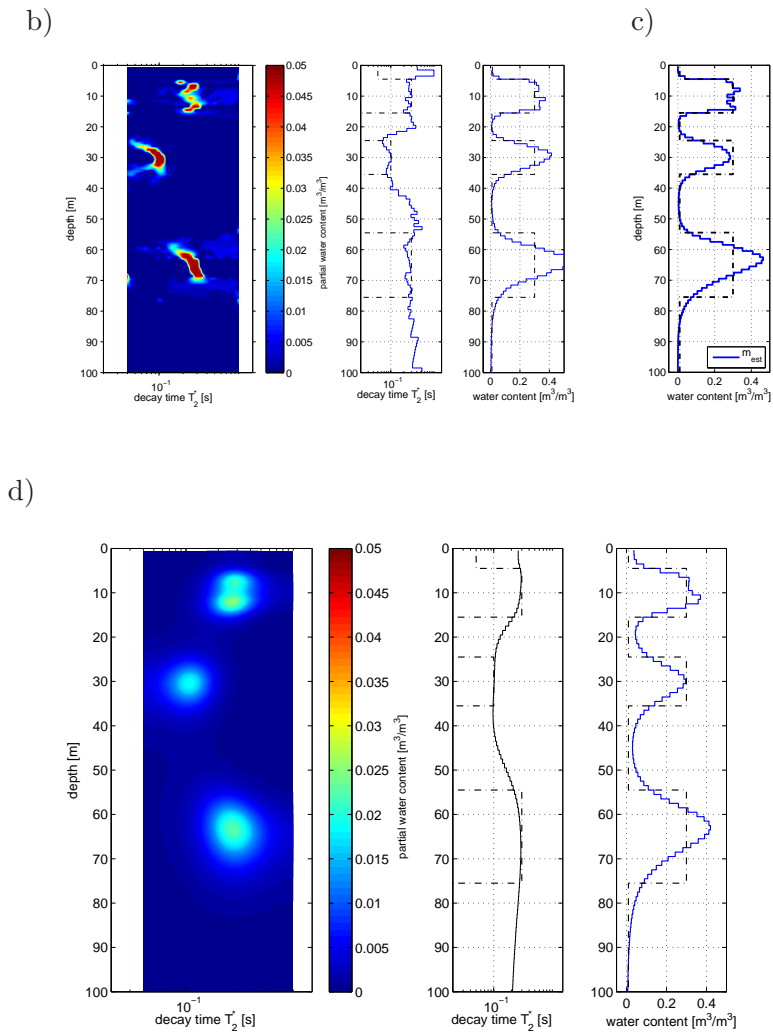


Figure 6.5: Inversion scheme comparison according to the synthetic model in figure 6.4 and the general setting as described in the text. a) real and imaginary data; b) time step inversion: PWC distribution, mean decay time depth distribution and total water content using corrected amplitudes dataset (left to right); c) initial value inversion; d) QT inversion: PWC distribution, mean decay time depth distribution and total water content using corrected amplitudes dataset (left to right). Gaussian noise with 5 nV standard deviation.

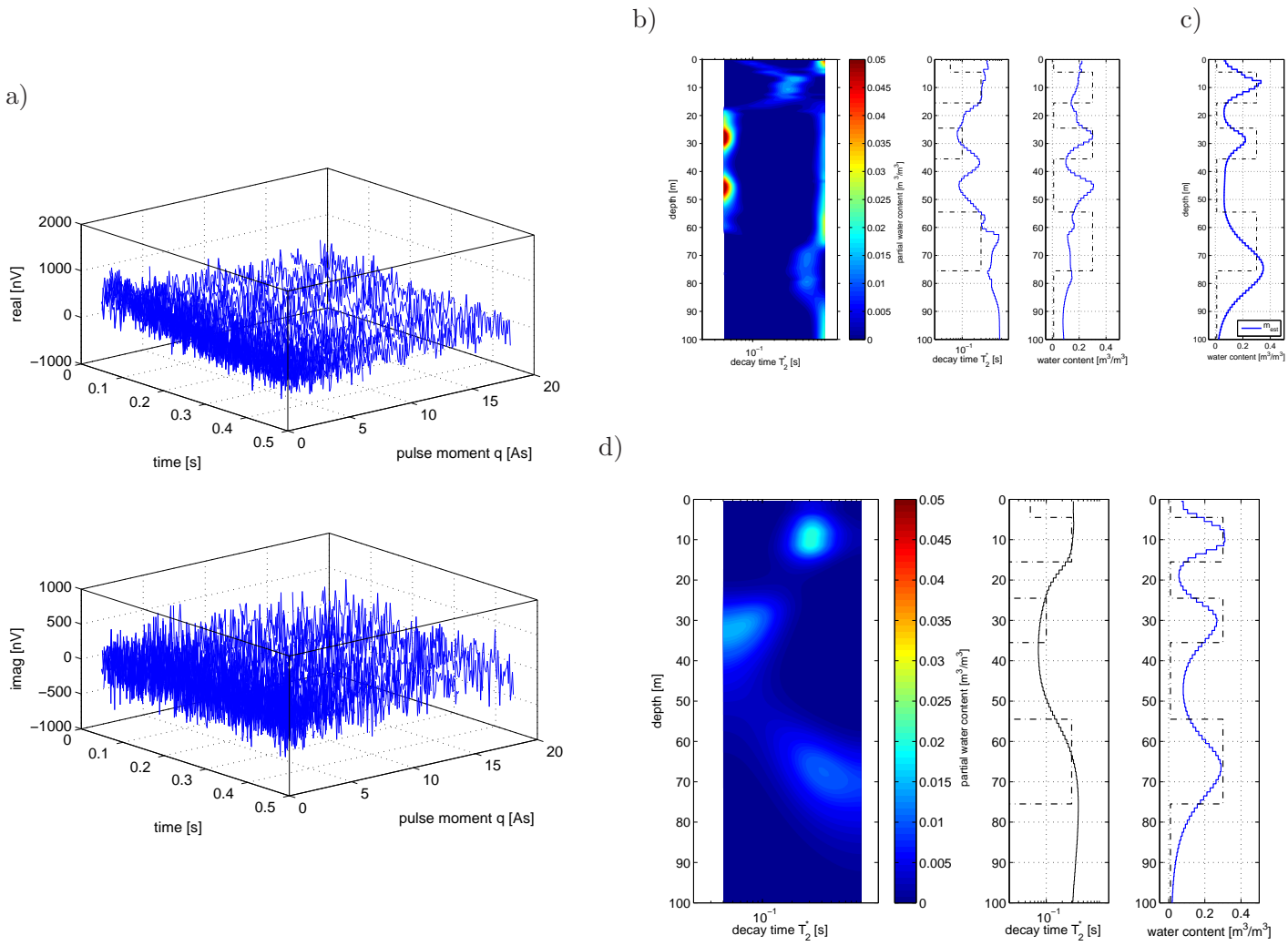


Figure 6.6: Inversion scheme comparison as described in figure 6.5 Gaussian noise with 200nV standard deviation.

Figures 6.5/6.6 show the synthetic dataset in real and imaginary part as used for mono-exponential fitting. Time step and QT inversion uses the corrected amplitudes as described in subsection 4.3. All schemes use only the logarithmic transformation on the model space in order to avoid different properties and ensure comparability.

As expected for the low noise condition case all results of the total water content depth distribution are fairly equal. Due to the scheme no decay time is presented for the initial value inversion. The synthetic model is estimated nicely for both parameters but shows some overestimation of the water content for larger depths as discussed for the initial value inversion with logarithmic transformation.

At the high noise case the QT inversion can estimate the synthetic model reliable while the standard initial value inversion shows partly underestimated water content and the third aquifer is located at too large depth. More serious, the time step inversion is not able to estimate a useful model. In general, this example shows two effects.

First, with increasing noise condition the stabilising effect of the 2D inversion improves the inversion result, since dependent data is handled together and not separately. Thus, cross information can be used.

Second, comparing the time step inversion with the initial value inversion the different order of the two steps becomes important. On the one hand, the mono-exponential fit is very stable, i.e., the data quality is improved before inverting for water content. On the other hand, the time step inversion first estimates the water content that is (compared to the mono-exponential fitting) a rather unstable process, i.e., the data quality is not improved and due to the difficult regularisation process mostly worse. Consequently, for bad data quality the standard inversion should be preferred compared to the time step scheme.



## 7 Field cases

Finally, two field datasets, one measured at a well known test site (for comparison see [Yaramanci et al. \(2002\)](#)) Nauen/Germany (in courtesy of M. Hertrich and M. Braun) and another measured at the Shwaib/Emirate of Abu Dhabi test site (in courtesy of T. Hiller and Schlumberger Water Services) will be discussed in detail.

### 7.1 Nauen

#### 7.1.1 Test site geology - laboratory measurements

The Nauen test site is mainly characterised by glacial sediments as typical for wide parts of northern Germany. In order to determine the specific and local properties of the test site a research well had been drilled in 2001. A wide set of geophysical methods were carried out and presented in [Yaramanci et al. \(2002\)](#). This study characterises the site as partly 2D while the research well is located at 1D condition. Figure 7.1 shows some of the laboratory measurements using core samples provided during the drilling. The laboratory measurements provide the mean grainsize by sieving, total porosity by weighting and laboratory NMR  $T_2$  decay time distributions (in courtesy of S. Costabel). Using these results the 1D part of the test site is characterised below:

1. A primary unconfined aquifer from about 2 meter (in dependency on the seasonal change) down to about 22 m and build by medium sand (0-7 m, 35 % porosity), fine sand (7-12 m, 37 % porosity) interrupted by glacial till (8-9 m, 40 % porosity), gravel (12-14 m, 30 % porosity) and again fine sand (14-22 m).
2. A aquiclude consisting of marl down to 30 m with porosities of about 45 %.
3. A highly structured confined second aquifer partly with thicker layers of fine sand or till material that might be separated into 2 aquifers. The second ranges from 30 down to 40 m depth and the third from 45 m on.

The laboratory NMR measured log mean NMR  $T_2$  decay time (Fig. 7.1) do not generally correspond to the lithology and especially the dimension of the measured  $T_2$  relaxation times are too small corresponding to an expected permeability. Even though, this petrophysical observation is part of further research a first approach of interpretation is according to [Keating and Knight \(2007\)](#) and bases on the presence of iron oxides. The authors concluded that the presence of iron oxides significantly decreases the  $T_2$  relaxation rates in dependency on concentration and its mineralogical form by increased surface relaxation rates. The laboratory measurements at the samples of the Nauen core were carried out in 2008, i.e., at dry samples that had to be re-saturated. This is exactly the sample preparation process used in [Keating and Knight \(2007\)](#). Due to the geology it can be expected that iron either as Fe(II) or Fe(III) depending on the redox condition exist. Thus, after re-saturation of dry samples the iron is oxidised and decreased relaxation rates occur. Especially the small layer of gravel at about 12 m depth is known to

carry large amounts of iron. Therefore, this layer is represented by too small relaxation rates compared to the surrounding medium sand.

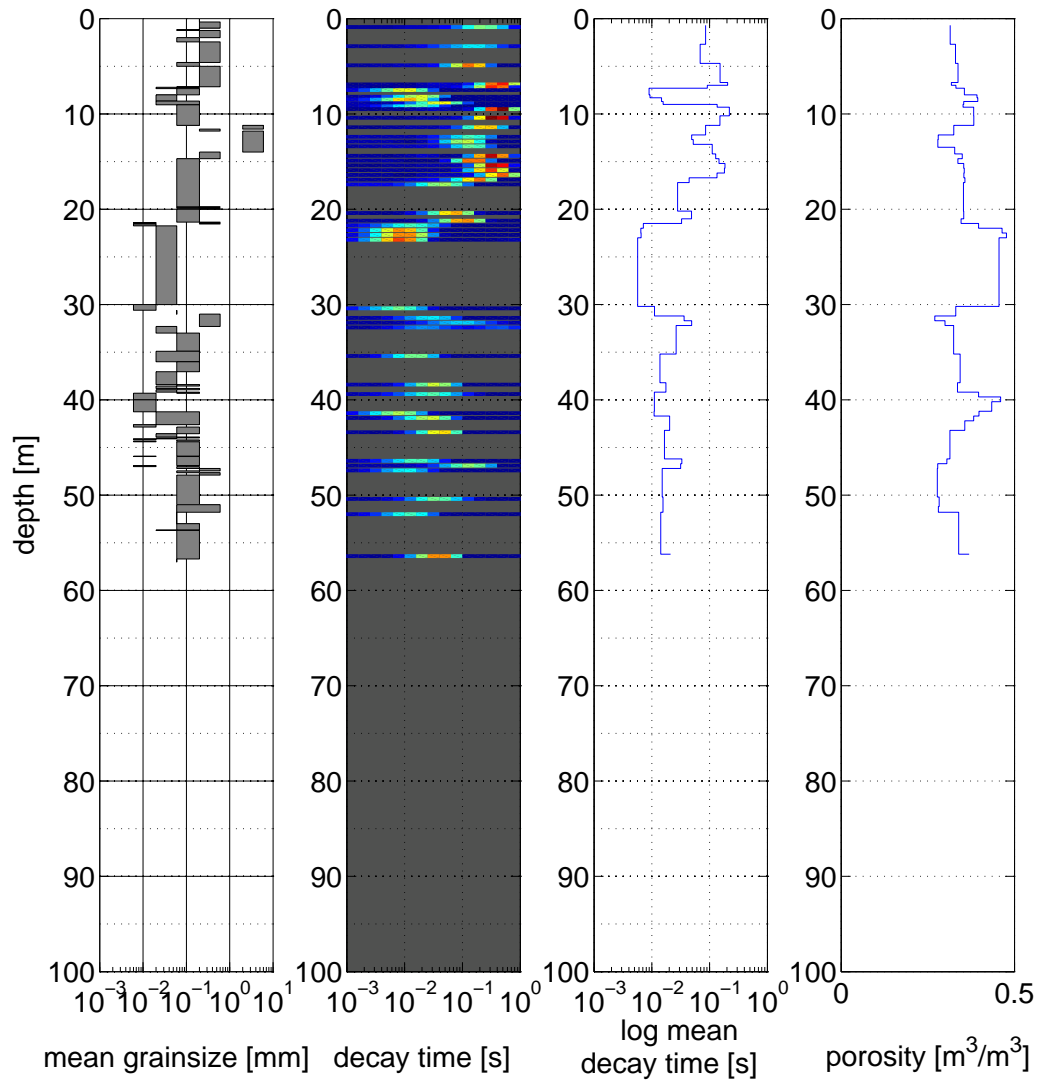
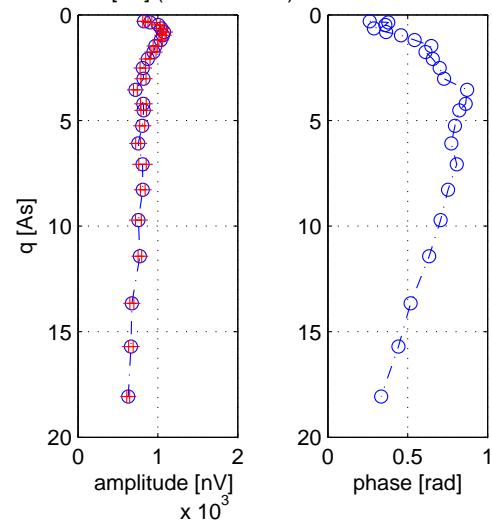


Figure 7.1: Laboratory measurements at core samples from the research well. The mean grain-size is derived by sieving, total porosity by weighting and decay time after multi-exponential fitting of  $T_2$  measurements.

mean std: 28.29 [nV] (gaussian)  
 mean std: 16.8 [nV] (@ dead time)



mean std: 0.0070498 [s]

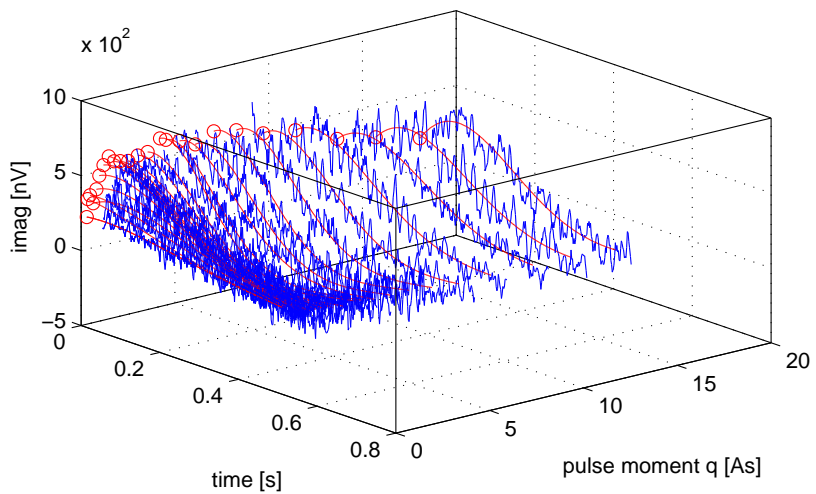
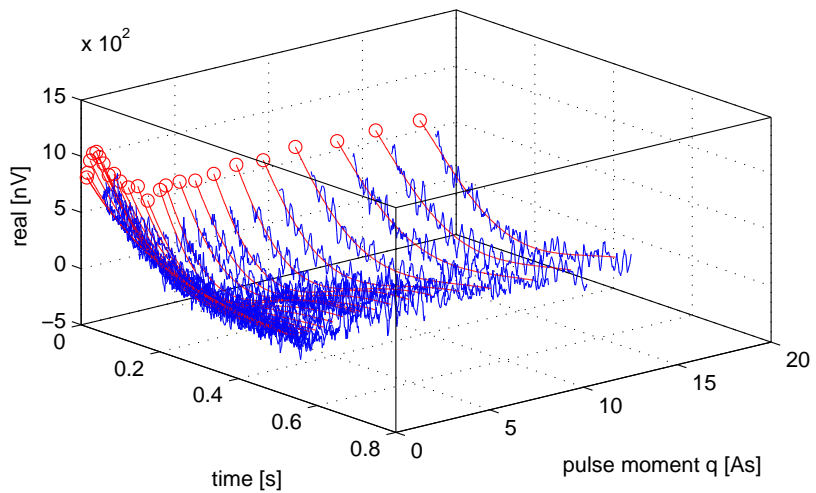
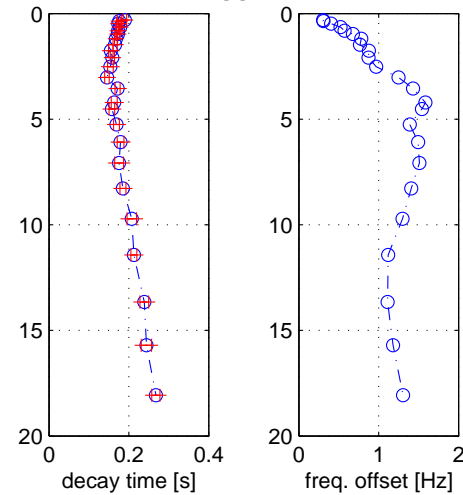


Figure 7.2: Field measurements at Naumen test site using a 96 m diameter circular loop.

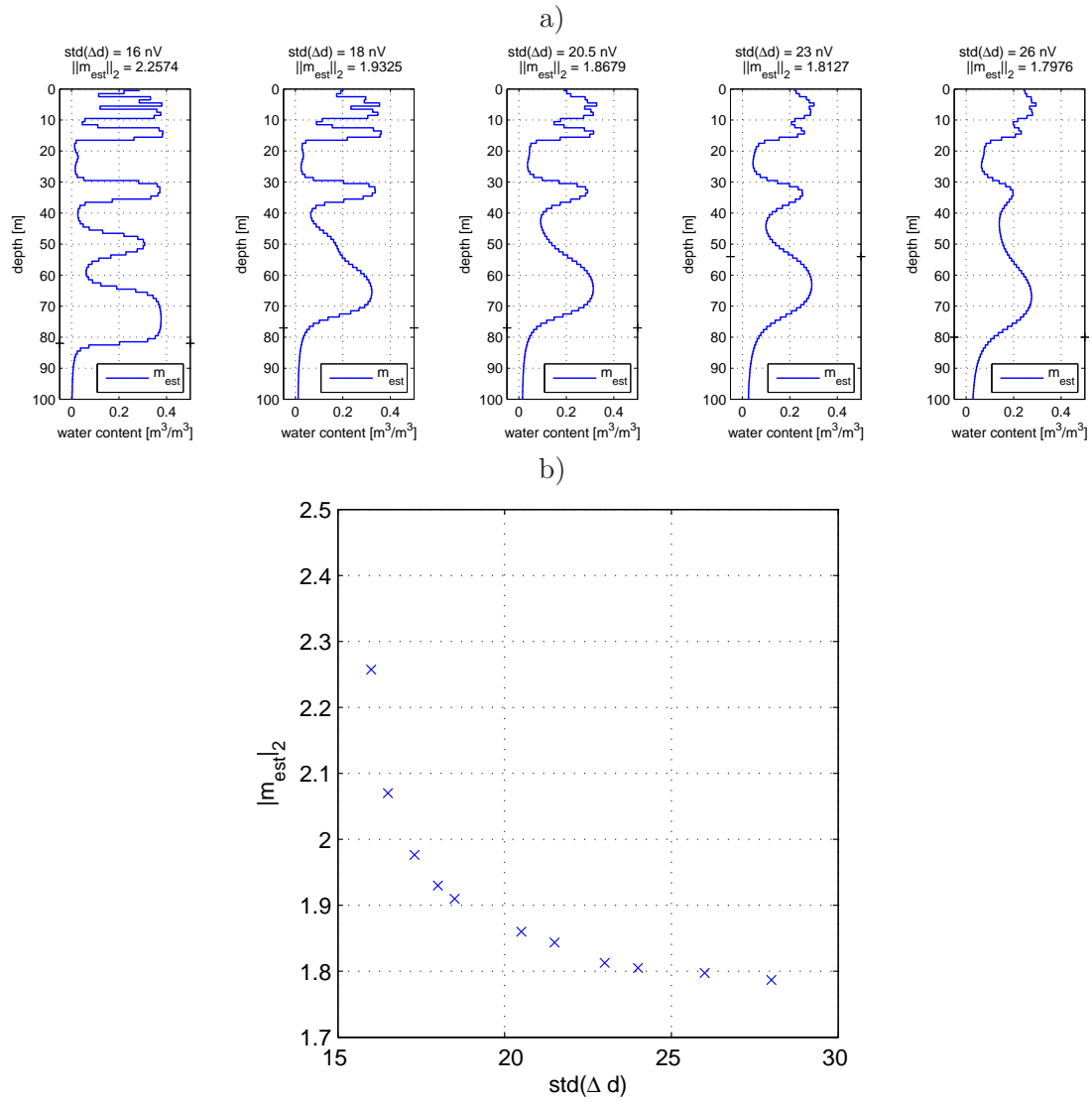


Figure 7.3: Set of initial value inversion (using the tangens transformation for both model and data space with an upper boundary of  $0.4 \text{ m}^3/\text{m}^3$  water content) to cover the range of data error from 16 nV up to 26 nV. b) L-curve for the calculated models in a).

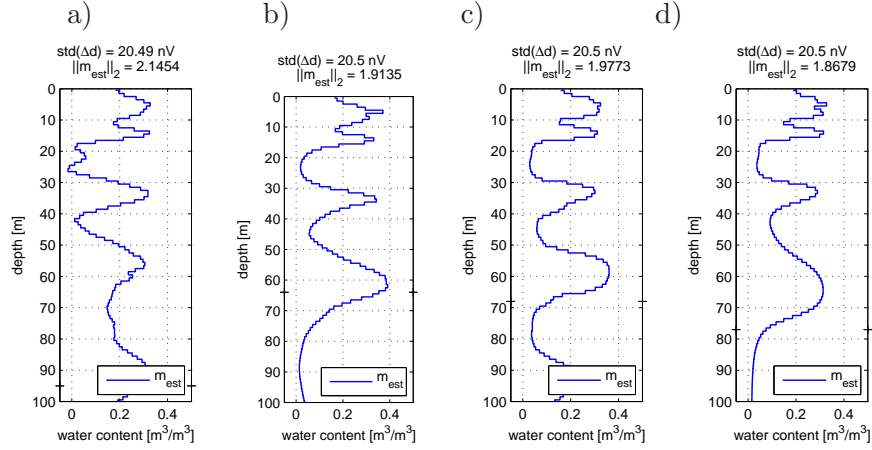


Figure 7.4: Set of initial value inversion using a) untransformed amplitudes, b) logarithmic model space, c) tangens transformed model space with  $0.4 \text{ m}^3/\text{m}^3$  water content as upper boundary and d) both data and model tangens transformation all fitting the data with the same data misfit.

### 7.1.2 Results of the different inversion schemes

**MRS dataset** Next, a field measurement was carried out close to the research well using a 96 m diameter circular loop of one turn. The dataset is presented in figure 7.2 including the mono-exponential fit.

The overall data quality is very good for field measurements, i.e., the average noise is about 60 nV while the maximum amplitude is about 1000 nV. In detail, the dataset shows a large frequency variation up to 1.5 Hz that obviously influences the signal phases. According to subsection 4.2.2 the calculated initial values show standard deviations of 28 nV as upper limit (Gaussian error propagation) and 17 nV as lower limit (at dead time). This error estimation can be used to determine the regularisation for the initial value inversion. As expected from the laboratory the surface NMR decay times as a function of the pulse moment derived from the mono-exponential fit show variations.

**Initial value inversion** First, the standard initial value inversion without decay time interpretation will be discussed.

According to the interval of expected data errors (16 nV up to 26 nV) a set of inversions was calculated (with tangens transformation for both the model and data space with an upper boundary of  $0.4 \text{ m}^3/\text{m}^3$  water content) fitting the data within that range (Fig. 7.3). In order to calculate the well known L-curve as a common approach to decide for an optimal regularisation, the  $L_2$  norm of the model is calculated and plotted against the data misfit. The model showing the largest curvature within the L-curve is selected. Corresponding to the presented L-curve this is the model of 18 nV data misfit. In a subjective manner this model appears to be quite rough. As a smoother representation the model of 20.5 nV is taken as subsurface water content distribution. Next, the different transformations as described in subsection 5.4 are presented in figure 7.4. Obviously, the subjective model quality increases the more additional information via transformations can be introduced. The differences between model space tangens transformed and both side tangens transformed model cannot be evaluated since borehole data is available only down to 60m depth. According to the results of subsection 5.4 mostly the accuracy at

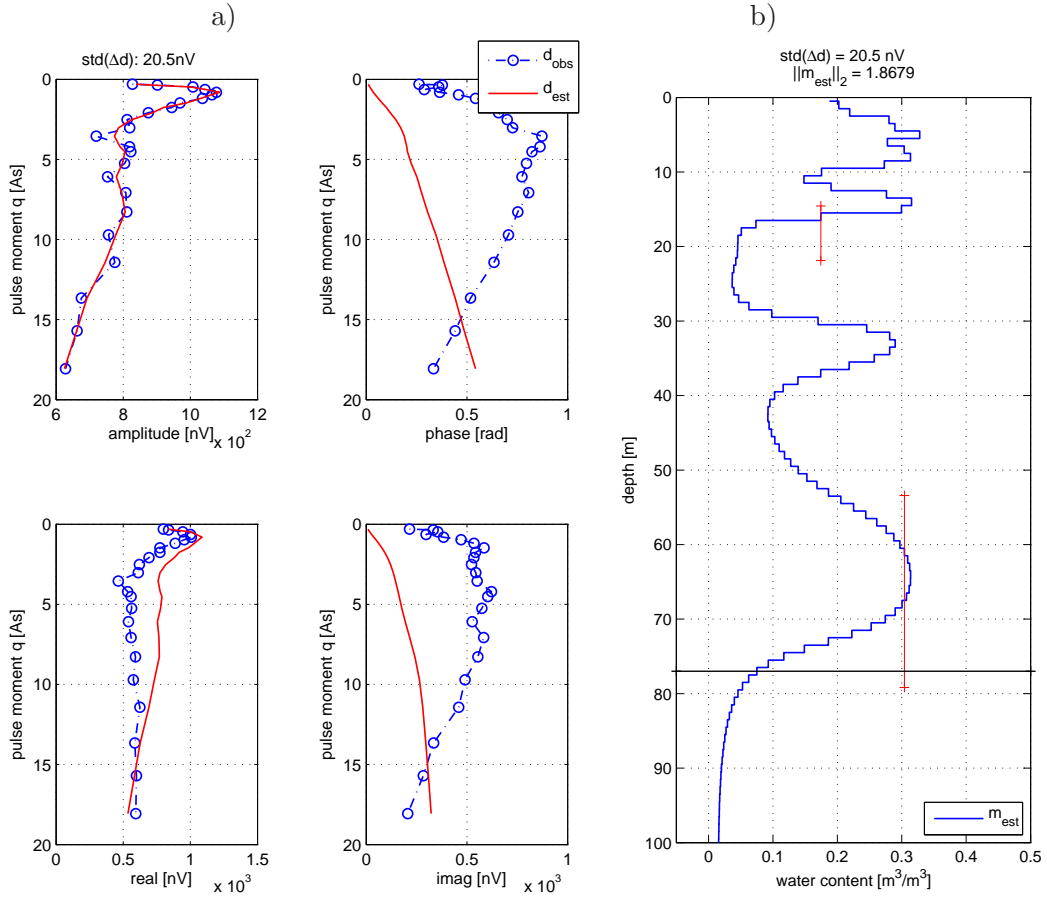


Figure 7.5: Final inversion result using initial value inversion. a) complex data (blue circles) as amplitude, phase, real and imaginary part as well as the corresponding estimated data (red line). b) Estimated model (blue line), resolution (red) and confidence depth (black).

larger depth benefits from the data space transformation and should be trusted.

Finally, figure 7.5 shows the result including resolution properties and confidence depth as well as the data fit in detail for the complex signal. The estimated model represents the main water content structure in Nauen. Remark, water content corresponding to small decay times (approx.  $T_2 < 0.04$  s, e.g. clay) cannot be measurement and appears as dry zones. A detailed comparison of the field measurements to the laboratory results will follow after presenting all inversion schemes.

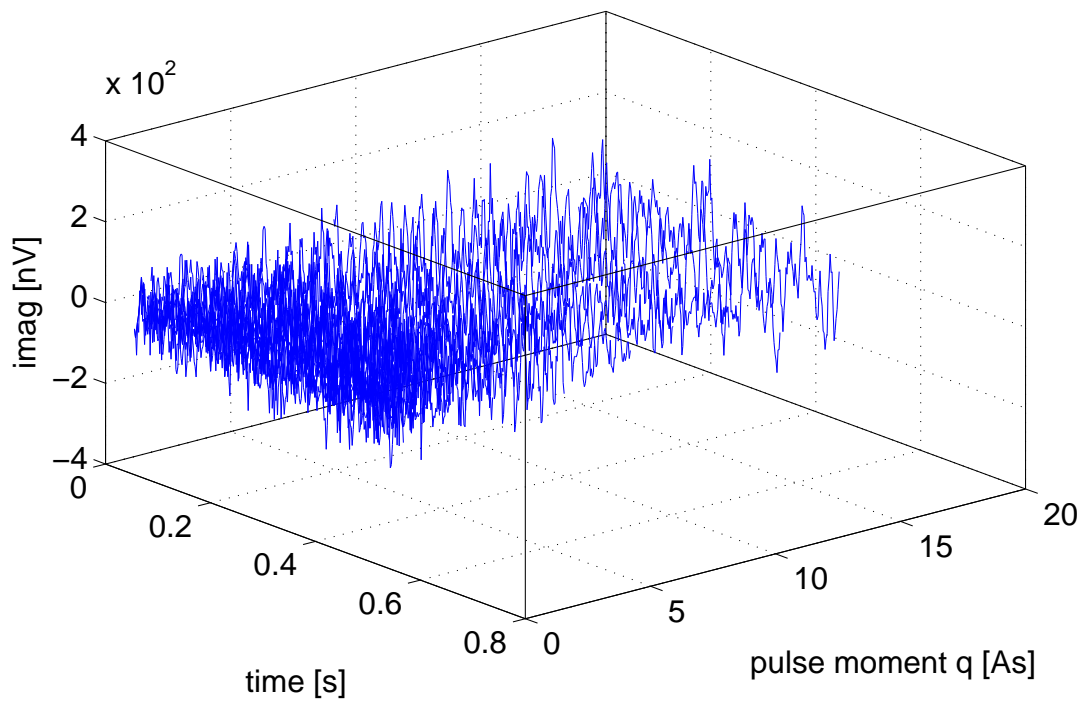
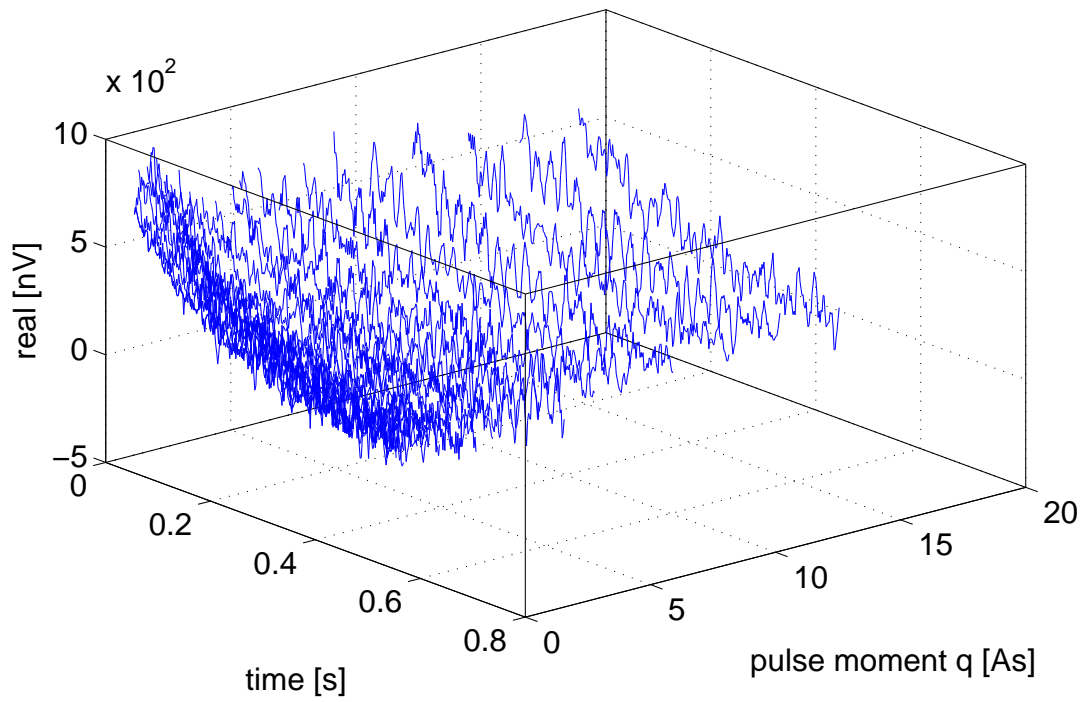


Figure 7.6: Dataset after subtracting the signal phase and frequency offset in order to use the real part of the signal as amplitudes, i.e., to ensure unbiased decay times.

**Time step inversion** First, the dataset is processed to calculate the corrected amplitude signals. As necessary, the imaginary part of the signal is reduced to a random distribution only consisting of the noise and the real part carries the complete information (Fig. 7.6). Hence, the real part can be used to fit with the synthetic signal amplitudes and ensures unbiased decay times in contrast to directly using the amplitude signal.

The final inversion result using the time step inversion is presented in figure 7.7. Clearly, the independent use of any sounding curve as single inversion are visible (Fig. 7.7a). The results is a fairly unconstrained global datafit while every single data fit is according to a data average noise of 62  $nV$  (the same as for the final results of the QT inversion). The direct results of these single inversion is the water content decay signal (Fig. 7.7b). These results of the first step are now used for multi-exponential fitting. Even without fitting the larger decay time of first aquifer compared to the smaller decay time of the second one is visible (Fig. 7.7b). As expected (reminding the resolution properties in general and especially the comparison of the transformation schemes in section 5.4) for larger depth the inversion results become more unstable. Here one of the drawbacks using the model space logarithmic transformation without upper boundaries is obvious compared to the initial value inversion. Finally, after fitting the PWC distribution, the total water content (the sum over the PWC distribution) and the log mean decay time (the logarithmic mean of the PWC distribution) are presented in figure 7.7c.

**QT inversion** Last but not least the results of the QT inversion using the same corrected amplitudes as for the time step inversion and also only using model space logarithmic transformation is shown in figure 7.8. A proper model is chosen by calculating the L-curve (Fig. 7.8a) and selecting the largest curvature. In contrast to all other schemes the observed data is fitted in one single step taking all data into account. Thus, the estimated data is a smooth surface explaining the observed data as presented in figure 7.8b. The corresponding model to this datafit is shown in figure 7.8c again as PWC distribution (as the original output of the inversion scheme), total water content and log. mean decay time.

### 7.1.3 Discussion and comparison to the laboratory data

All three inversion schemes show globally a three aquifer case. But in detail the results are different among each other and different from the laboratory.

The lower boundary of the first aquifer is estimated at approx. 15 m from the field measurements while the laboratory indicates 22 m. This can be caused by two effects. On the one hand, taking into account that the first aquiclude (the marl) is rising and crops out in a distance of some 100 m and even though the field measurements are close to the borehole this different estimation can be geological truth. On the other hand, the decay time of the lower part of the aquifer is small (about 0.05 s) and might be undetectable by field measurements.

Besides this lower boundary the detailed internal structure of this first aquifer is estimated different by the field measurements. Referring to the laboratory this aquifer is separated by a small till layer at about 8-9 m depth. Due to the decay time the water content is not visible for MRS and, consequently, appears as a zone of less water. This layer is only very slightly visible by the time step inversion and slightly too deep by the initial value inversion. The QT inversion estimates the position very nicely compared to the laboratory. Of course the resolution radius is too large to estimate the water content precisely, i.e., an average according to the resolution properties is estimated. The small gravel layer at 12 m depth cannot be separated from the surrounding sand since the decay time differences are too small to be resolved by field data quality. Finally, the upper boundary, i.e., the water table at about 2 m, is estimated well with



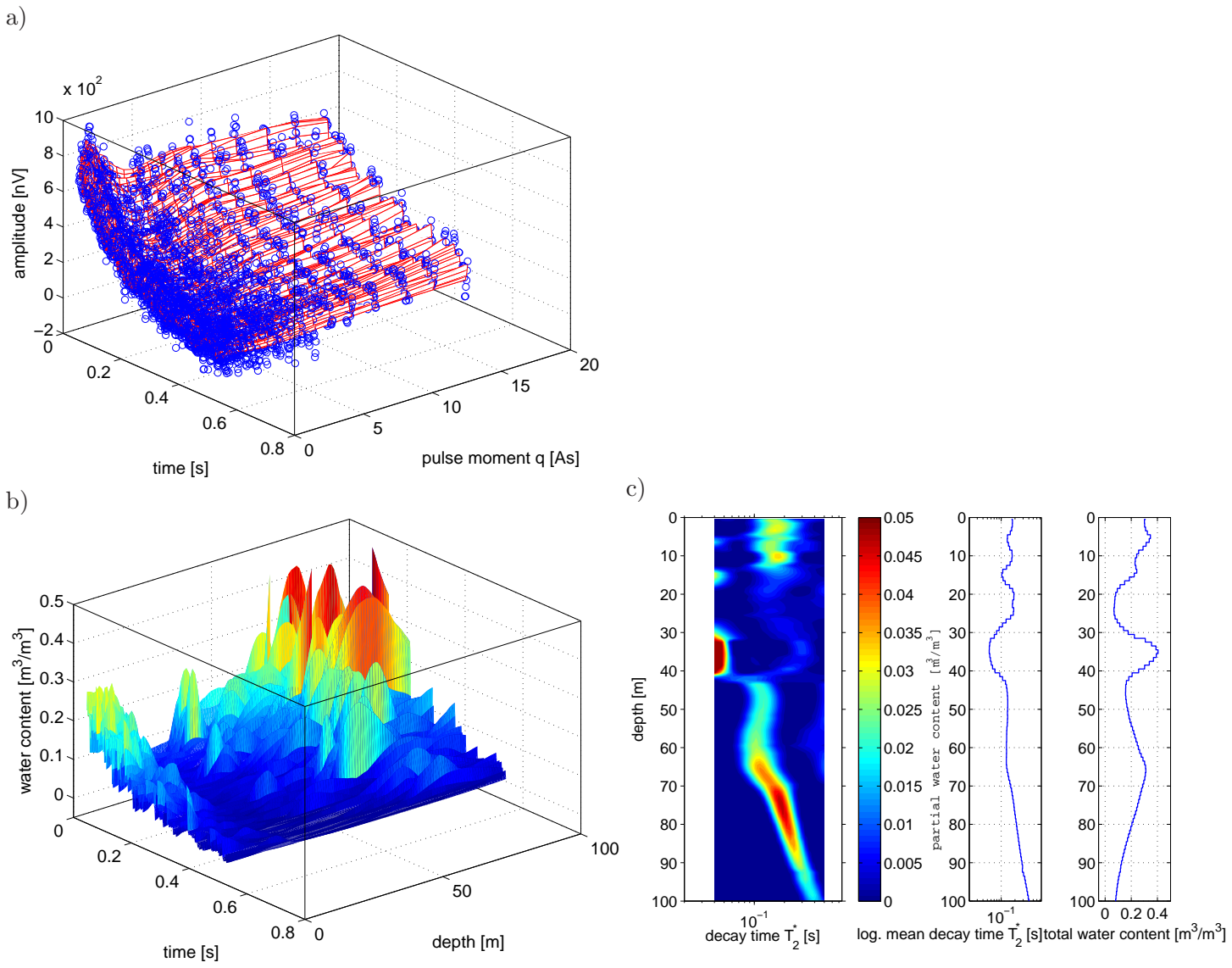


Figure 7.7: Time step inversion. a) Dataset of corrected amplitudes (blue circles) and estimated sounding curves (red lines), b) Water content domain after the first inversion step, i.e., single results at every time step, c) PWC distribution, total water content (sum of the PWC distribution and log. mean of the distribution) after multi-exponential fitting of b).

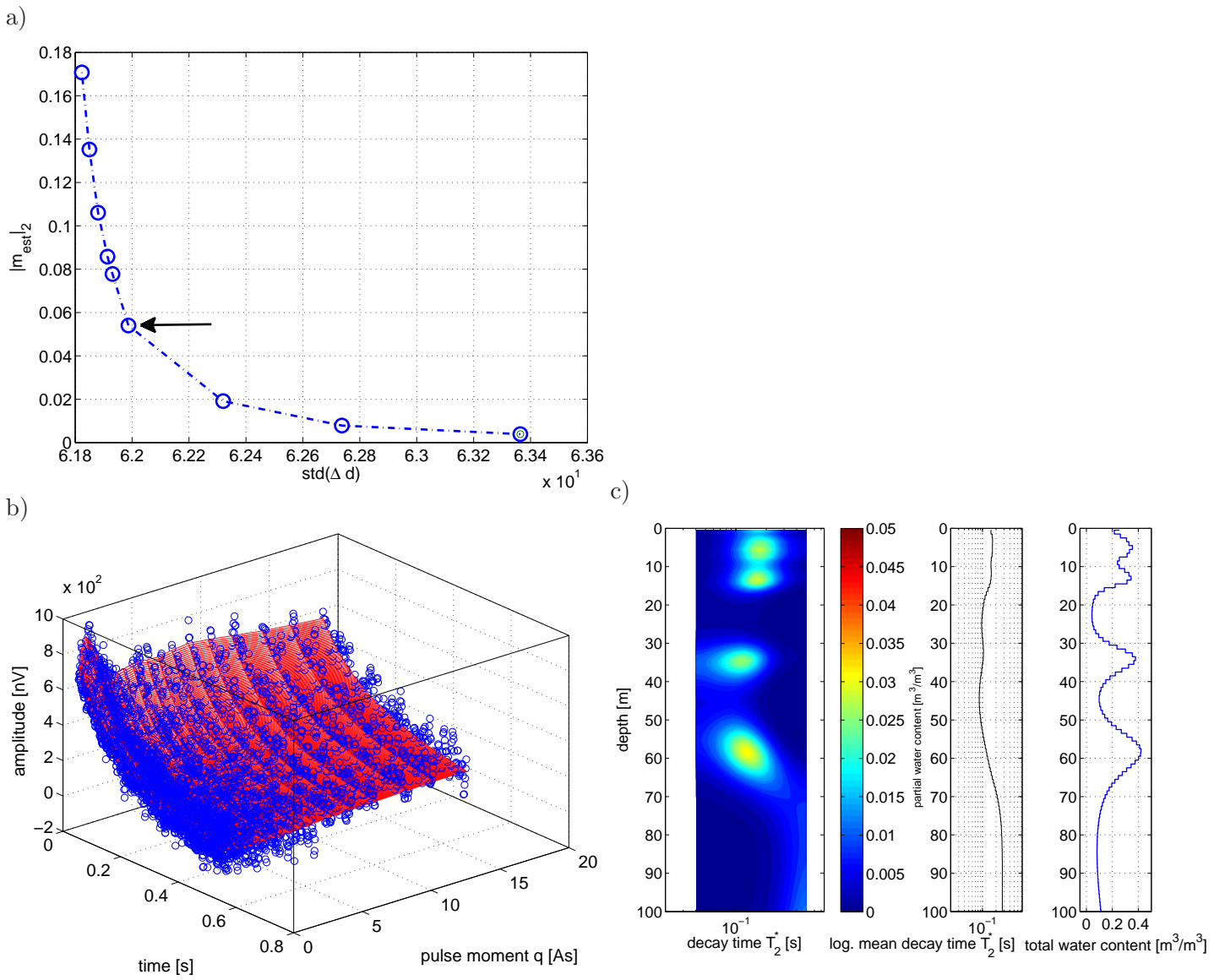


Figure 7.8:  $QT$  inversion. a) L-curve for different regularisation parameter setting (the final setting is indicated by an arrow), b) Dataset of corrected amplitudes (blue circles) and estimated data (red), c) PWC distribution, total water content (sum of the PWC distribution and log. mean of the distribution) as direct result of the inversion).

both the initial value inversion and QT inversion.

The estimated decay times for the first aquifer are equal to the laboratory. Be aware, even the laboratory measurements show too small decay time due to possible iron oxides. Consequently, we can expect to have an oxidation regime as well for the field measurements. This interpretation appears to be valid for the upper 10 m - 20 m. At larger depth an inconsistency appears. If the lower part after 15 m depth of the first aquifer is not visible due to small decay times a second and third aquifer should not be detectable too, according to the laboratory decay times since these decay times are even smaller.

One interpretation approach leads back to the influence of iron oxides. After [Bryar and Knight \(2002\)](#) and in contrast to the effects of  $FE(III)$ ,  $FE(II)$  does not influence the NMR decay time. The laboratory samples all include the influence of  $FE(III)$  due to the re-saturation. At field conditions the oxidation environment turns into reducing environment at some depth. That is,  $FE(II)$  instead of  $FE(III)$  is present. Thus, field measurements are not affected by decreased decay times for large depth and the second and third aquifer is detectable.

The quality of estimation for the water content is comparable between all schemes but the decay time estimation of the time step inversion shows an effect discussed in subsection [4.2.1](#). For bad data the total water content might be estimated well but the distribution prefers very small or large times.

The third aquifer using the time step inversion is a rather very smooth estimation while initial value inversion and QT inversion show a clear separation.

In conclusion, the QT inversion shows the aquifer structure in most detail and contains (from the point of inversion) reliable decay time information.

## 7.2 Shwaib

The data shown next results from a joint research project by the Technical University of Berlin and Schlumberger Water Services as presented in [Hiller \(2008\)](#). Amongst others, this project allowed to compare high resolution borehole NMR data with surface NMR data.

### 7.2.1 Test site geology - borehole NMR

The geology at the Shwaib site is mainly dominated by a tightly folded and thrust-faulted regime striking NNE-SSW originating in the Late Eocene-Miocene collision of the northeastward moving Arabian Plate and the Eurasian Plate. Stratigraphically the near surface sediments can be divided into four parts from top to bottom:

- Unsaturated Aquifer, unconsolidated quartz-rich sand dunes ( $\sim 30\text{m}$  high)
- Saturated Aquifer, Quaternary unconsolidated Aeolian sands and silt clays
- Upper Fars unit, claystone with interbedded dolomitic marls, limestone and siltstones
- Lower Fars unit, mudstone and evaporites

Schlumberger Water Services has accomplished an Aquifer Storage and Recovery Project including the drilling and logging of more than 20 wells spread over the whole test site. Figure 7.9 shows the results of NMR borehole measurements as provides by Schlumberger Combinable Magnetic Resonance (CMR) tool for the well SWS16 that is close to the MRS measurements shown later. Here, no focus is drawn on borehole interpretation but the CMR porosities and the decay time spectra are used. The CMR porosities indicate the saturated aquifer at approximately 40m down to 70m below surface. The decay time distribution and its separation into several decay time classes (left column) show very small decay times. Even for the water saturated aquifer most of the extractable water corresponds to decay times of less than 0.15 s. Neglecting capillary bounded water of decay times less than 0.03 s (as a usual cutoff for bounded water) an extractable water content of about 20 % can be expected.

### 7.2.2 Results

The measurement as presented next was located approx. 70 m west of SWS16 using a 100 m square loop. The local Larmor frequency was 1850 Hz, earth field inclination was  $35^\circ$  and the maximum pulse moment for 0.04 s pulse duration was 12.5 As. The resistivity distribution was derived from borehole and transient electromagnetic (TEM) measurements (not shown here). The noise condition were acceptable but according to the expected very small decay times the signal to noise ratio is quite unfavourable even after 256 stacks as shown in figure 7.10. Most of the recorded NMR signals had vanished into the noise level after 0.05 s.

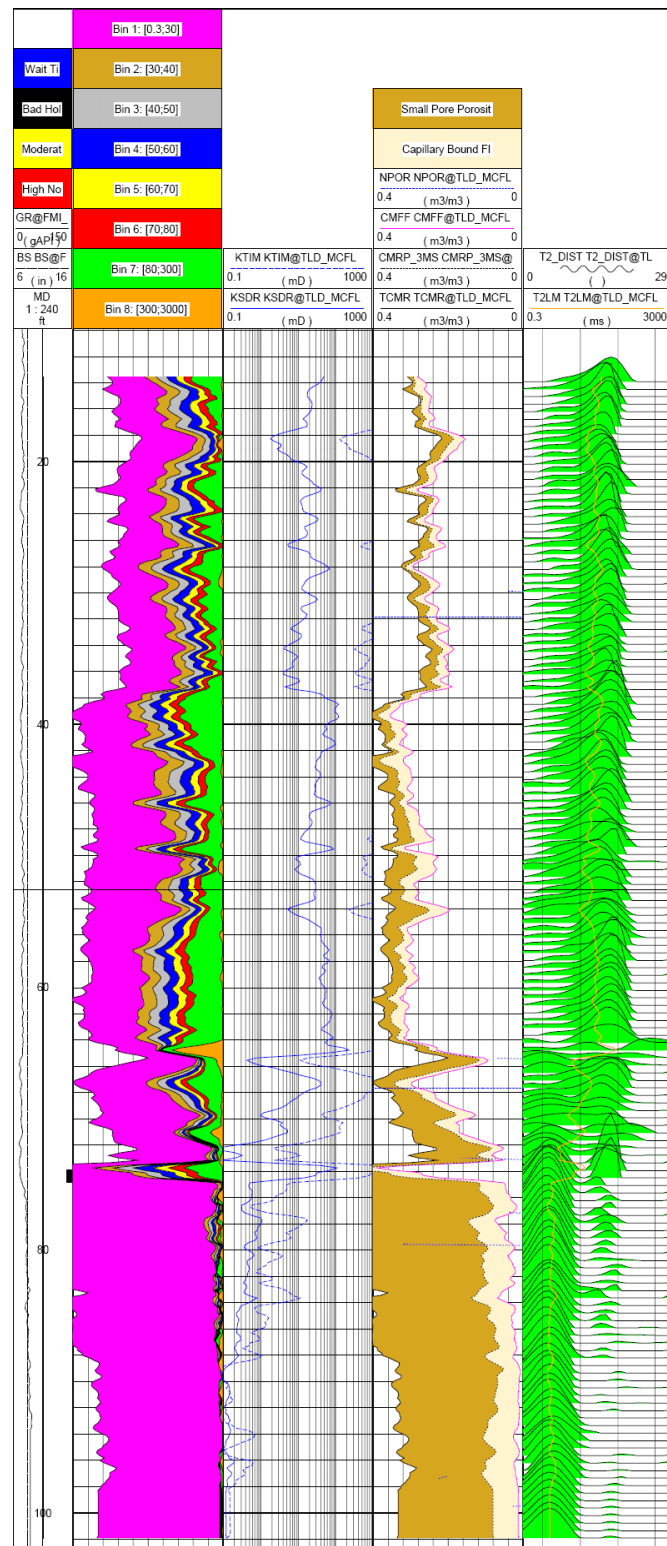


Figure 7.9: Combinable Magnetic Resonance (CMR) log at the well SWS16.

## 7 Field cases

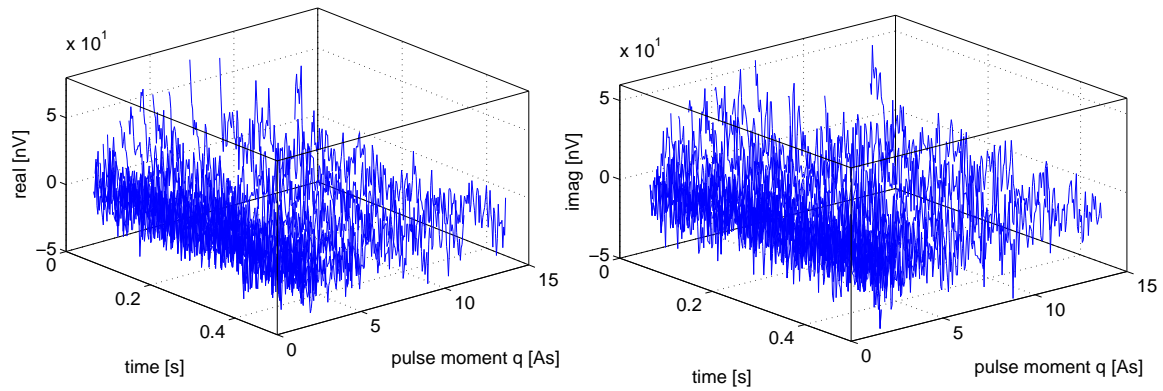


Figure 7.10: Rawdata after 256 stacks and despiking at Shwaib test site. Measurement parameter are: 100 m square loop, 1850 Hz Larmor frequency and earth field inclination of  $35^\circ$ .

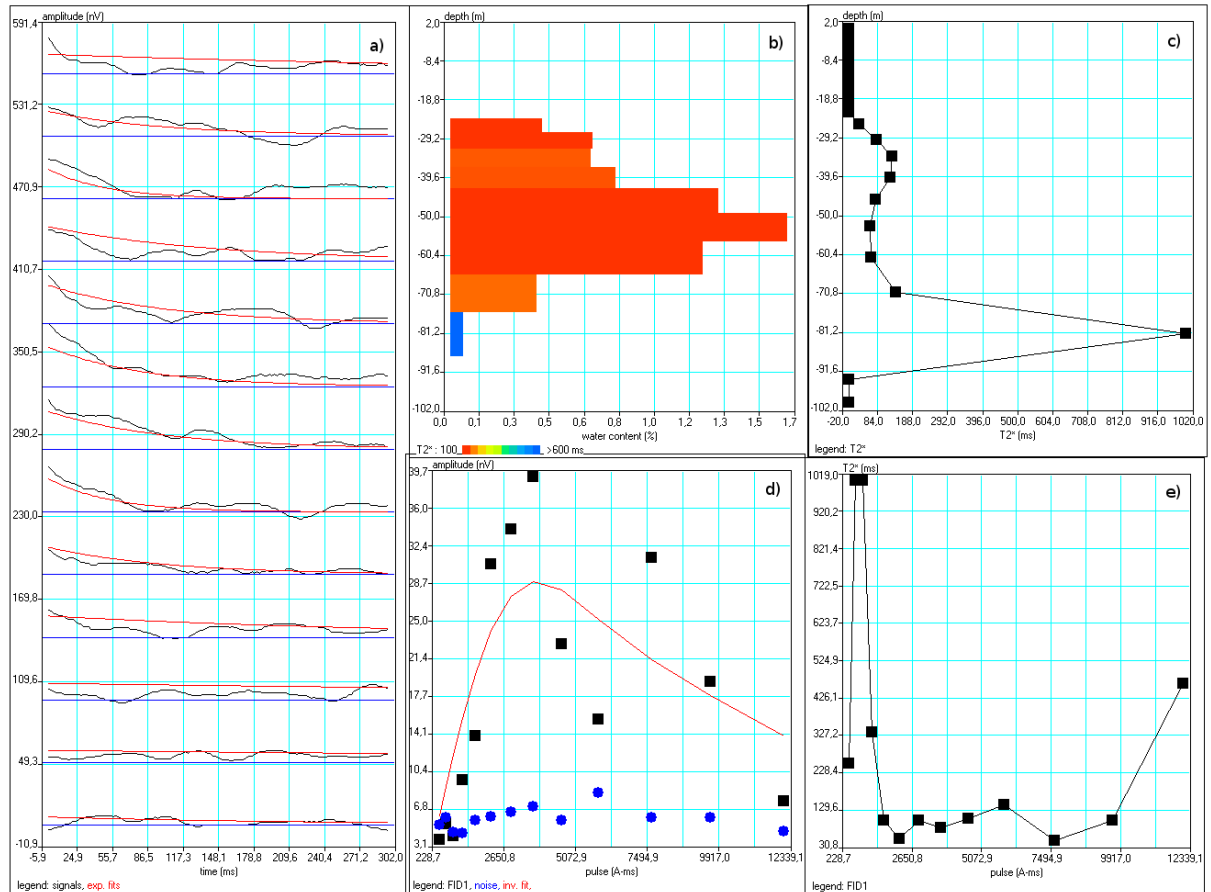


Figure 7.11: SAMOVAR (Iris Instruments) Processing and Inversion result. a) fitted signals, b) water content model, c) decay time model, d) sounding curve (black squares), noise (blue dots), inverted sounding curve (red line), e) decay time per pulse moment

**Samovar - Inversion result** First, the MRS standard processing result as presented in [Hiller \(2008\)](#) using the inversion software Samovar as provided by Iris Instruments (Fig. 7.11) is discussed. The software processes and inverts the data according to [Legchenko and Valla \(2002\)](#), i.e., water content inversion using the initial values and the decay time inversion using a time step inversion approach with mono-exponential fit. The fitted single signals are shown in figure 7.11a while initial amplitude and  $T_2^*$  decay time in dependency of the pulse moment is shown in figure 7.11d/e, respectively. The total water content is approximated with maximum 2 % at 55 m depth (Fig. 7.11b) with an upper aquifer boundary at approx. 30 m. Compared to the borehole NMR the total water content is underestimated and also the upper boundary is wrong. These bad results can be interpreted as follows: The signal fit estimates too long decay times, resulting in too small initial amplitudes. This is due to the very short NMR signals and the unfavourable noise condition. Therefore, also the sounding shows bad quality, resulting in a very smooth water content estimation and inexact boundary estimation. Furthermore, after [Walbrecker et al. \(2009\)](#) the 0.04 s excitation pulse hardly affects water content estimation for NMR signals with very small decay times. The authors recommend to extrapolate the measured signals not to the end of the excitation pulse but in the middle of the pulse duration  $\tau$ . This reduces wrong water content estimation. Using Samovar this cannot be taken into account.

**Initial value inversion** Second, the signals were processed according to subsection 4.2.1. This does not essentially differ from the Samovar exponential fitting routine but provides additional processing and control like

- Despiking to enhance signal quality
- Every signal can be processed individually to adjust start parameter for the exponential fit
- According to [Walbrecker et al. \(2009\)](#), the exponential fit can be extrapolated to the middle of the pulse  $\frac{\tau}{2}$ , i.e., 0.06 s (0.04 s pulse, 0.04 s dead time) to calculate the initial values and thus the sounding curve.

Figure 7.12 shows the fitting results according to this processing. Compared to Samovar processing smaller decay times and higher initial amplitude were calculated. The sounding curve appears to be slightly smoother due to additional processing. Nevertheless the signal to noise ratio (largest amplitude of 600 nV/ averaged standard deviation of 100 nV) is only 6.

Finally, the processed dataset is inverted using the initial value inversion (Fig. 7.13a) and using the QT inversion (Fig. 7.13b/c).

On the one hand, the initial value inversion using the both side logarithm transformation shows a significantly improved result that fits the expectation of 20 % water content but estimates the upper aquifer boundary at about 45 m depth slightly to deep. At depth larger than 50 m the water content estimation becomes wrong, showing an decrease of water content until 65 m depth. The large increase of water content for depths larger than 70 m should not be interpreted since not covered by methods sensitivity.

On the other hand, the QT inversion reconstructs the subsurface compared to the NMR logging very well. Due to the joint use of all data in a single inversion step, resulting in a smooth datafit (Fig. 7.13c) the maximum information content of the dataset can be extracted. The upper boundary of the aquifer is close to the logging tool determined boundary and also the water content, related to the decay times is nicely estimated. Furthermore, even at larger depth



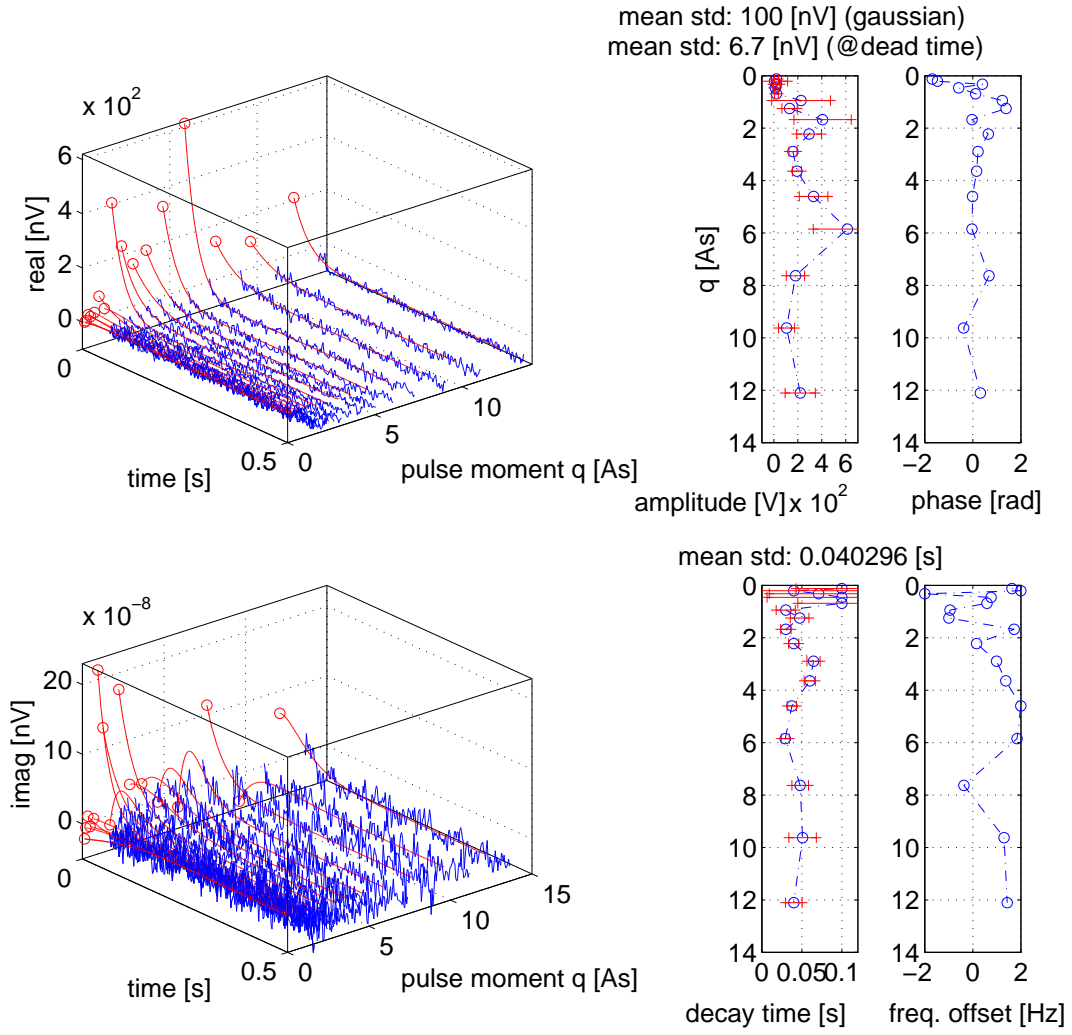


Figure 7.12: Individually processed dataset of the Shwaib measurements including despiking, individual fitting and extrapolation to  $\frac{\pi}{2}$

the total water content is correctly estimated.

Consequently, even at low signals and short decay times and therefore unfavourable data quality, MRS using the QT inversion is able to reliably detect the subsurface water content distribution comparable to NMR logging tools.



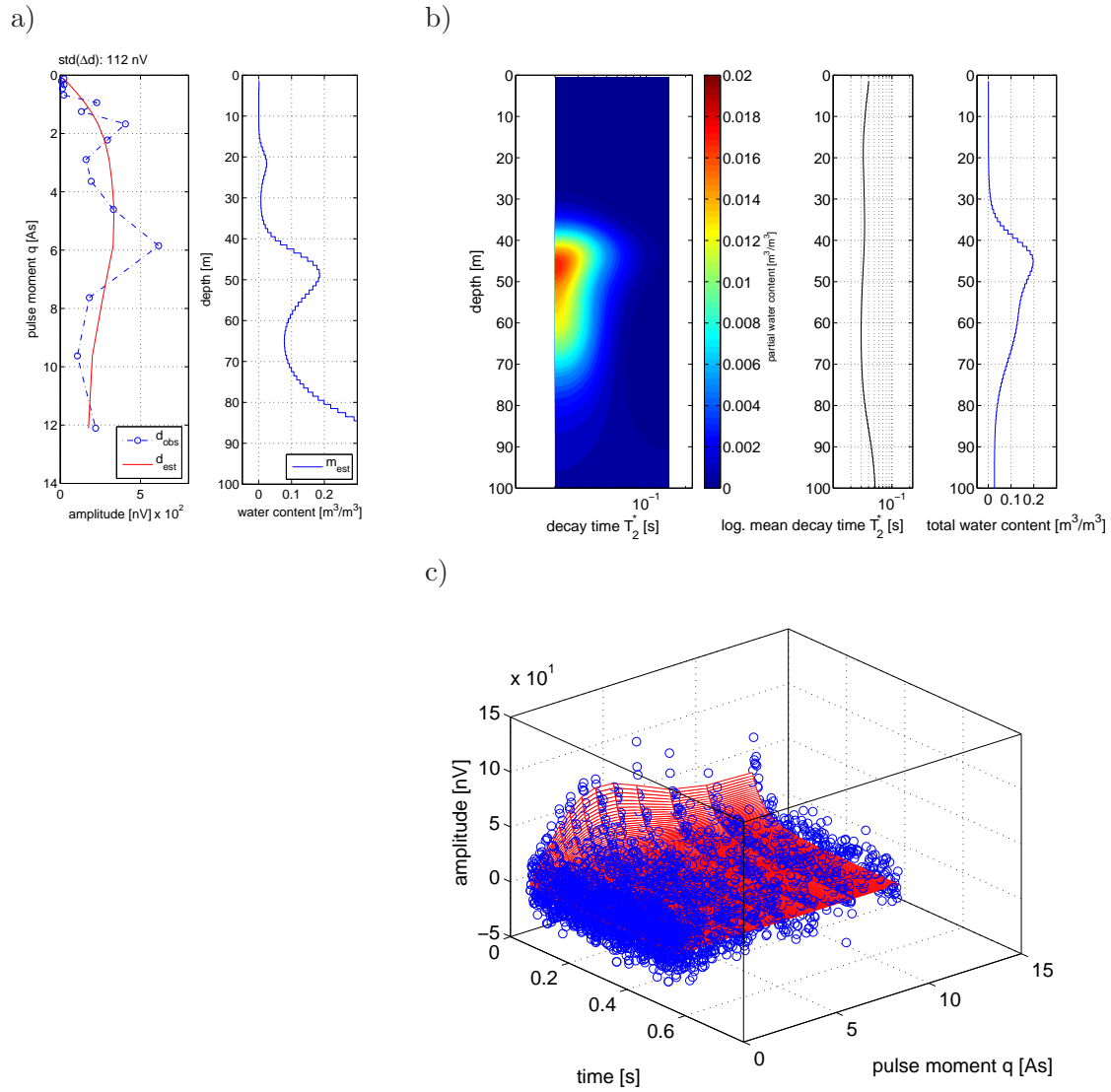


Figure 7.13: Inversion results using a) initial value inversion (both side log. transformation) and b) QT inversion. c) shows the datafit of the QT inversion result.



## 8 Conclusion and Outlook

The development of the Surface Nuclear Magnetic Resonance method has been very rapidly with respect to the last decade. The theoretical framework for the surface NMR forward problem had been extended to all physical parameters and spatial dimension. Thus, inversion schemes had been developed to fundamentally take advantage of these extensions both for spatial dimensions, i.e., 2D water content inversion and physical parameters, i.e., resistivity inversion. Therefore, in the course of this work detailed investigations towards the basics of the inverse problem have been done, including the development of a new solutions scheme, assessing data uncertainty and resolution of the estimated model.

The initial value inversion approach to the inverse problem had been focused first. Along with the data processing it had been shown that taking a usual signal to noise level into account a convenient separation into NMR decay time distribution as known from laboratory applications is not possible and mono-exponential fitting should be preferred. The target values extracted by this processing step are, according to the set of physical parameter and the governing equations, the complex initial values and the decay time of the detected signal both as a function of the pulse moment.

Next, a scheme was presented that estimates the uncertainty of these values based on noise records, covariance analysis and Gaussian error propagation. The scheme was evaluated with synthetic and field data. Concerning field data it showed that, using a dataset with repeated measurements but in agreement with other field data, the amplitude and decay time are repeatable parameter and the uncertainty can be predicted very nicely by the scheme. Thus, in the sense of signal processing the amplitude and decay time are reliable parameters. Remark, repeatability in this context includes an unchanged loop position. There are datasets measured at locations with comparable hydrological parameters but showing different (repeatable) decay times. Therefore, petro-physical research showing sources of influence on the decay time (e.g. [Keating and Knight \(2007\)](#), [Bryar and Knight \(2002\)](#)) is needed and research on hidden influences like frequency variation (in time and space) causing significantly decreased decay times is of interest. In the course of this work some effects that might influence the signal in a systematic fashion and consequently undetectable from the point of signal processing, like frequency variations were evaluated and discussed.

On the other hand, the signal phase is even concerning repeatability often rather erratic. Consequently, amplitudes are preferred as default dataset for estimations of the subsurface water content and assessing surface NMR resolution properties.

In respect to recently presented new measurement devices that provide full time series at higher sampling and new designed digital record technology as well as noise reducing systems and multi channel possibilities, the signal processing part will become of increasing interest for further research.

Next, the initial value inversion scheme estimates the subsurface water content based on mono-exponential data fitting and extrapolation to calculate initial values. An error estima-

tion as presented in the signal processing chapter is used for reliable water content estimation including error estimation for the water content. At this, a confidence interval as an estimator down to which depth the inversion is reliable and a resolution measure was introduced. Moreover, the dependencies of the method concerning loop size, maximum pulse moment and resistivity are shown. This analysis allows determining layout parameter, such as loop size, beforehand. The importance of this pre-survey analysis is underlined by a dataset measured in Haldensleben/Germany. It shows that increasing the loop size does not necessarily increase the depth down to which the inversion result can be trusted and, in addition, the resolution decreases as it was calculated beforehand. Therefore, this section lists several dependencies of the confidence depth to common field layouts and noise levels. Remarkably, investigations down to depth larger than 100 m are not possible.

Since a MRS measurement can take up to several hours depending on the noise conditions and number of pulse moments there is a need for optimisation and efficiency. Analysing the data resolution matrix an optimal distribution of pulse moments had been presented as well as a rule of thumb to estimate an efficient number of pulse moment in the field. Even though, the presented sequence is very similar to the currently used and the impact of this section is more theoretically, the presented approach holds for 2D investigations, i.e., separated loop sounding and promises great influence on resolution and efficiency. In general, the extension of the resolution analysis for both the data and model space is straight forward. First results for 2D resolution were shown and the use of separated loop sounding for lateral resolution is clearly emphasised.

Transformations were assessed in order to improve the initial value inversion scheme. Here, the already developed tangens transformation that introduces a lower and upper boundary for the estimated water content is combined with a newly introduces pseudo water content. This conjunction enables the use of the tangens transformation also for the data space and clearly improves the final estimated model. It should be recommended to use this both side transformation as standard application in future.

Finally, a new inversion scheme was developed to avoid the inability of the initial value inversion to invert for spatial decay time depth distribution and the drawbacks of stability concerning the time step inversion. The new inversion scheme called QT inversion, due to the data space parameter pulse moment  $q$  and time  $t$ . QT inversion takes for the first time advantage of the native two parameter data structure of even one dimensional sounding and satisfies all data jointly. The improved stability and resolution properties are shown by synthetic and field examples. Foremost the field example of Shwaib clearly shows that using the QT inversion reliable inversion results can be derived even from measurements at an unfavourable signal-to-noise ratio.

According to the advantage of using transformations that improve the inversion results with restrictions on the model and data space the QT inversion should be extended to a layered or block inversion since the actual scheme estimates a smooth parameter distribution. Furthermore, an extension to 2D should be envisaged and coordinated with further evaluation of physical influences on the decay time as well as joint inversion schemes.

## 9 Acknowledgements

Many people took part during many years of research for this thesis. Some of which provided the working background that's necessary and some the social and of much importance some did both. I am glad to have met them and looking forward to keep the contact. Anyhow some are of special importance.

Prof. U. Yaramanci for giving me the opportunity to work with a new and dynamical growing geophysical method. He was always open minded for discussions and provided the freedom to develop and follow my own ideas.

Prof. A. Kemna who agreed to be the second referee.

Dr. M. Hertrich for invaluable introductions, explanations and motivation, even beyond the topic of SNMR. Without him it would have taken me much more time to step in. He attended and motivated my work throughout the years in Berlin and later from Zürich. Finally his fair and constructive criticism improved this work substantially.

Gerhard Lange and M. Hertrich both showed me what SNMR field work means, how nice data and places can look at times I will never forget.

I would like to thank Dr. Martina Braun, Jochen Kamm and Stephan Costabel for fruitful discussions and a pleasant team play during all the years at the Department of Applied Geophysics at the Berlin University of Technology, especially Stephan for keeping me up to date and activating my interests for petrophysics.

I am grateful to my parents who never stop believing in me.

Finally, I am deeply grateful to my wife and daughter. Christiane, you turn my point of view whenever I got on the wrong track. Thank you Gesine, for sometimes claiming your Dad by 100%. Thank you both for your love.

## 9 Acknowledgements

# Bibliography

- Aster, R., B. Borchers, and C. Thurber, 2005, Parameter estimation and inverse problems: Elsevier Academic Press.
- Braun, M., 2002, Untersuchungen komplexwertiger Oberflächen-NMR Signale im leitfähigen Untergrund: Master's thesis, Technische Universität Berlin.
- , 2007, Influence of the resistivity on magnetic resonance sounding: 1d inversion and 2d modelling: PhD thesis, Technical University of Berlin.
- Braun, M., M. Hertrich, and U. Yaramanci, 2003, SNMR investigations with variable parameters and loop geometries - A comprehensive study: Proceedings of the 2nd International workshop on MRS, Orleans, France, 137–140.
- Braun, M. and U. Yaramanci, 2008, Inversion of resistivity in magnetic resonance sounding: Journal of Applied Geophysics.
- Bryar, T. and R. Knight, 2002, Sensitivity of nuclear magnetic resonance relaxation measurements to changing soil redox conditions: Geophysical Research Letters, **29**.
- Buttkus, B., 2000, Spectral analysis and filter theory in applied geophysics: Springer-Verlag Berlin.
- Curtis, A., 1999, Optimal design of focused experiments and surveys: Geophysical Journal International.
- Curtis, A. et al., 2004, A deterministic algorithm for experimental design applied to tomographic and microseismic monitoring surveys: Geophysical Journal International.
- Dahlin, T. and B. Zhou, 2004, A numerical comparison of 2d resistivity imaging with 10 electrodes: Geophysical Prospecting.
- Eikam, A., 2000, Modellierung der Amplituden von Oberflächen-NMR-messungen an 2D- und 3D-strukturen.: Diplomarbeit, Technische Universität Berlin, Fachgebiet Angewandte Geophysik.
- Fedi, M., P. Hansen, and V. Paoletti, 2005, Analysis of depth resolution in potential-field inversion: Geophysics.
- Friedel, S., 2003, Resolution, stability and efficiency of resistivity tomography estimated from a generalized inverse approach: Geophysical Journal International, **153**, 305–316.
- Gover, F., 1946, Inductance calculations, working formulas and table: Dover Publication, New York.
- Guenther, T., 2004, Inversion methods and resolution analysis for the 2d/3d reconstruction of resistivity structures from dc measurements: PhD thesis, Technischen Universitaet Bergakademie Freiberg.
- Guenther, T., M. Müller-Petke, M. Hertrich, and C. Rücker, 2008, The role of transform functions in geophysical inversion: Presented at the Proceedings of EAGE Near Surface 2008 Meeting, Krakau/Poland.
- Guenther, T., C. Rücker, and K. Spitzer, 2006, Three-dimensional modelling and inversion of dc resistivity data incorporating topography – ii. inversion: Geophysical Journal International.
- Hansen, P., 1994, Regularisation tools: A matlab package for analysis and solutions of discrete ill-posed problems: Numerical Algorithms, **6**.

- , 1996, Piecewise polynomial solutions without a priori break points: Numerical Linear Algebra with Applications.
- Hertrich, M., M. Braun, and U. Yaramanci, 2005, Magnetic resonance soundings with separated transmitter and receiver loops: Near Surface Geophysics, **3**, 131–144.
- Hertrich, M. et al., 2007, Surface nuclear magnetic resonance tomography: IEEE TRANSACTIONS ON GEOSCIENCE AND REMOTE SENSING.
- Hertrich, M., M. Müller-Petke, and T. Günther, 2008, Optimized inversion of surface nmr data: Presented at the Proceedings of the DGG Annual Meeting 2008, Freiberg/Germany.
- Hiller, T., 2008, Joint interpretation of magnetic resonance sounding and nmr - logging: Master's thesis, Berlin, University of Technology.
- Iris Instruments, 2000, Numisplus - surface proton magnetic resonance system for water prospecting: Reference Manual.
- Keating, K. and R. Knight, 2007, A laboratory study to determine the effect of iron oxides on proton nmr measurements: Geophysics, **72**.
- Legchenko, A., 2004, Magnetic Resonance Sounding: Enhanced Modeling of a Phase Shift: Applied Magnetic Resonance, **25**, 621–636.
- Legchenko, A. and O. A. Shushakov, 1998, Inversion of surface NMR data: Geophysics, **63**, 75–84.
- Legchenko, A. and P. Valla, 1998, Processing of surface proton magnetic resonance signals using non-linear fitting: Journal of Applied Geophysics, **39**, 77–83.
- , 2002, A review of the basic principles for proton magnetic resonance sounding measurements: Journal of Applied Geophysics, **50**, 3–19. Special Issue.
- Levitt, M. H., 2002, Spin Dynamics - Basics of Nuclear Magnetic Resonance: John Wiley & Sons, LTD.
- Mansfield, P., A. Maudsley, P. Morris, and I. Pykett, 1979, Selective Pulses in NMR Imaging: A reply to Criticism: Journal of Magnetic Resonance, **33**, 261–274.
- Menke, W., 1984, Geophysical data analysis: Discrete inverse theory: Academic Press Inc.
- Militzer, H. and F. Weber, eds., 1985, Band 1: Gravimetrie und magnetik. Angewandte Geophysik: Akademie-Verlag.
- Miller, C. R. and P. S. Routh, 2007, Resolution analysis of geophysical images: Comparison between point spread function and region of data influence measures: Geophysical Prospecting.
- Mohnke, O. and U. Yaramanci, 2002, Smooth and block inversion of surface NMR amplitudes and decay times using simulated annealing: Journal of Applied Geophysics, **50**, 163–177.
- , 2005, Forward modeling and inversion of MRS relaxation signals using multi-exponential decomposition: Near Surface Geophysics, **3**, 165–185.
- , 2008, Pore size distributions and hydraulic conductivities of rocks derived from magnetic resonance sounding relaxation data using multi-exponential decay time inversion: Journal of Applied Geophysics.
- Müller-Petke, M., M. Hertrich, and U. Yaramanci, 2006, Analysis of magnetic resonance sounding kernels concerning large scale applications using svd: Presented at the Proceedings of the 19th EEGS conference 2006, Seattle/USA.
- Müller-Petke, M. and U. Yaramanci, 2008, Resolution studies for magnetic resonance sounding (mrs) using the singular value decomposition: Journal of Applied Geophysics.
- Semenov, A., A. Burshtein, A. Pusep, and M. D. Schirov, 1988, A device for measurements of underground mineral parameters: USSR Patent 1079063. in Russian.
- Strehl, S., 2006, Development of strategies for improved filtering and fitting of snmr signals: Master's thesis, Berlin University of Technology.



- Strehl, S. and U. Yaramanci, 2008, Resolution limits of nmr-based estimation of pore size distributions: Presented at the Proceedings of EAGE Near Surface 2008 Meeting, Krakau/Poland.
- Stummer, P., H. Maurer, and A. Green, 2004, Experimental design: Electrical resistivity data sets that provide optimum subsurface information: *Geophysics*.
- Taylor, J. R., 1982, *An introduction to error analysis*: University Science Books.
- Vouillamoz, J. et al., 2008, Contribution of magnetic resonance sounding to aquifer characterization and recharge estimate in semiarid niger: *Journal of Applied Geophysics*.
- Walbrecker, J., M. Hertrich, and A. Green, accepted - 2009, Accounting for relaxation processes during the pulse (rdp) in surface-nmr data: *Geophysics*.
- Warsa, W., O. Mohnke, and U. Yaramanci, 2002, 3-D modelling of Surface NMR amplitudes and decay times: *Water Resources and Environment Research ICWRER 2002*, 209–212.
- Weichman, P. B., E. M. Lively, and M. H. Ritzwoller, 1999, Surface nuclear magnetic resonance imaging of large systems: *Physical Review Letters*, **82**, 4102–4105.
- , 2000, Theory of surface nuclear magnetic resonance with applications to geophysical imaging problems: *Physical Review E*, **62**, 1290–1312.
- Wilkinson, P. et al., 2006, Improved strategies for the automatic selection of optimized sets of electrical resistivity tomography measurement configurations: *Geophysical Journal International*.
- Yaramanci, U., 2000, Surface Nuclear Magnetic Resonance (SNMR) - A new method for exploration of groundwater and aquifer properties: *Annali di Geofisica*, **43**, 1159–1175.
- Yaramanci, U., G. Lange, and M. Hertrich, 2002, Aquifer characterisation using surface NMR jointly with other geophysical techniques at the Nauen/Berlin test site: *Journal of Applied Geophysics*, **50**, 47–65.
- Yaramanci, U., G. Lange, and K. Knödel, 1999, Surface nmr within a geophysical study of an aquifer at haldensleben (germany): *Geophysical Prospecting*, **47**, 923–943.